

ALMA MATER STUDIORUM · UNIVERSITÀ DI BOLOGNA

SCUOLA DI SCIENZE
Corso di Laurea Magistrale in Fisica del Sistema Terra

**IMPACT OF CONVECTIVE MOTIONS
ON POLLUTANT DISPERSION
IN URBAN CANYONS: AN ANALYSIS
THROUGH RANS SIMULATIONS**

Relatore:

Dr. Carlo Cintolesi

Correlatrice:

Prof.ssa Silvana di Sabatino

Presentata da:

Simona Rinaldi

Anno accademico 2021/2022

Contents

1	Introduction	1
1.1	Objectives	1
1.2	Planetary Boundary Layer and Urban Canyons	2
1.2.1	Planetary Boundary Layer	2
1.2.2	Urban Boundary Layer and Urban Canyons	5
1.2.3	Urban Heat Island and Heat Waves	7
1.3	State of the Art	9
1.4	Structure of the thesis	10
2	Simulation methodology	12
2.1	Governing equations	12
2.2	Numerical approach and modelling	13
2.2.1	RANS	14
2.2.2	The $k - \varepsilon$ model	18
2.2.3	OpenFOAM	18
3	Problem description and Validation	22
3.1	Numerical Setup and Physical Parameters	22
3.1.1	Geometry and computational domain	22
3.1.2	Algorithm and numerical schemes	23
3.1.3	Initial and boundary conditions	25
3.1.4	Non-Dimensional Parameters	25
3.2	Convergence assessment	27
3.3	Validation	31
3.3.1	Neutral case	31
3.3.2	Heated case	36
3.3.3	Comparison between the neutral and heated cases	41
3.4	Final remarks	44

4 Results	45
4.1 Weak convective motions ($Ri = 0.5$)	47
4.1.1 Upwind building heated	47
4.1.2 Downwind building heated	50
4.1.3 Ground and both buildings heated	53
4.2 Balance between convective and inertial motions ($Ri = 1.0$)	56
4.2.1 Upwind building heated	56
4.2.2 Downwind building heated	58
4.2.3 Ground and both buildings heated	62
4.3 Strong convection motions ($Ri = 1.5$)	65
4.3.1 Upwind building heated	65
4.3.2 Downwind building heated	68
4.3.3 Ground and both buildings heated	71
4.4 Discussion	74
4.4.1 Upwind building heated	74
4.4.2 Downwind building heated	76
4.4.3 Ground and both buildings heated	76
5 Conclusions	79

Abstract

Climate change has a strong impact on cities through severe phenomena such as droughts, floods and heat waves, causing tremendous repercussions on the human population, the built environment and the socioeconomic one, being all these parts strongly interconnected. Considering that the majority of the population of the world lives in cities and that this number is expected to increase in the next years, one of the biggest challenges of the research is the determination of the risk deriving from those natural hazards together with improving responses to climate-related disasters, for example by introducing in the urban context vegetation or built infrastructures that can improve the air quality. This constitutes the basic step for the decision-making process on future risk management and mitigation measures. A way to do so is by using Computational Fluid Dynamics (CFD) as a tool for the investigation of the urban climate, the portion of climate studies that focuses attention on the local climate of cities. In fact, CFD provides detailed resolution of fields of interest at the small scale of the cities and can be used to investigate wind flow, thermal comfort, pollutant dispersion and other related topics. In this work, we will focus our attention on high temperatures experienced by cities and investigate how different setups of the boundary and initial conditions set on an urban canyon generate different patterns of the dispersion of a pollutant. All the possible configurations obtained are then categorised according to how they influence the result of the simulation (e.g. how they impact the dispersion of the pollutant). To do so we will exploit the low computational cost of Reynolds-Averaged Navier-Stokes (RANS) simulations to reproduce the dynamics of an infinite array of two-dimensional square urban canyons. A pollutant is released at the street level to mimic the presence of traffic. RANS simulations are run using the $k - \varepsilon$ closure model and vertical profiles of significant variables of the urban canyon, namely the velocity, the turbulent kinetic energy and the concentration, are represented. This is done using the open-source software OpenFOAM and modifying the standard solver `simpleFoam` to include the concentration equation and the temperature by introducing a buoyancy term in the governing equations. The results of the simulation are validated with experimental results and products of Large-Eddy Simulations (LES) from previous works showing that the simulation is able to reproduce all the quantities under examination with satisfactory accuracy. Moreover, this comparison shows that despite LES are known to be more accurate albeit more expensive, RANS simulations represent a reliable tool if a smaller computational cost is needed. Overall, this work exploits the low computational cost of RANS simulations to produce multiple scenarios useful to evaluate how the dispersion of a pollutant changes by a modification of key variables, such as the temperature.

Abstract

I cambiamenti climatici hanno un enorme impatto sulle città attraverso gravi fenomeni come siccità, inondazioni e ondate di calore, causando tremende ripercussioni sulla popolazione umana, l'ambiente edificato e il tessuto socio-economico, essendo queste parti fortemente interconnesse. Dato che la gran parte della popolazione mondiale vive nelle città e considerando che questo numero è previsto in aumento nei prossimi anni, una delle più grandi sfide della ricerca è la determinazione del rischio derivante da questi fenomeni naturali, insieme alla ricerca di soluzioni ai disastri climatici, ad esempio introducendo nel contesto urbano vegetazione e infrastrutture atti a migliorare la qualità dell'aria. Ciò costituisce il passo fondamentale per il processo decisionale per la futura gestione del rischio e per misure di mitigazione. Un modo per fare ciò è utilizzare La Fluidodinamica Computazionale (CFD) come strumento per l'investigazione del clima urbano, la parte di studi climatici che focalizza l'attenzione sul clima locale delle città. Infatti, la CFD fornisce una risoluzione dettagliata dei campi di interessi alla piccola (rispetto a quella globale) scala urbana, e può essere usata per studiare i flussi d'aria, il comfort termico, la dispersione degli inquinanti e altri argomenti correlati. In questo lavoro di tesi si focalizzerà l'attenzione sulle alte temperature che si possono manifestare nelle aree urbane e si investigherà come differenti configurazioni delle condizioni iniziali e al contorno imposte su un canyon urbano possono generare differenti configurazioni della dispersione di un inquinante. Tutte le possibili configurazioni verranno poi categorizzate a seconda di come influenzano il risultato della simulazione. Per fare ciò verrà sfruttato il basso costo computazionale dato dalle simulazioni Reynolds-Averaged Navier-Stokes (RANS) per riprodurre la dinamica di un array infinito bidimensionale di un canyon urbano con aspect ratio $H/W = 1$. In esso, un inquinante è emesso al livello della strada per riprodurre la presenza del traffico. Le simulazioni RANS sono lanciate utilizzando il modello di chiusura $k - \varepsilon$, attraverso il software Open-source OpenFOAM e modificando il preesistente solver `simpleFoam` in modo da includere l'equazione di concentrazione e la temperatura introducendo un termine di galleggiamento nelle equazioni governatrici. I risultati delle simulazioni verranno poi validati sia con risultati sperimentali che con quelli ottenuti da simulazioni Large-Eddy Simulation (LES) di precedenti lavori presenti in letteratura, mostrando che le simulazioni RANS possono riprodurre tutte le quantità esaminate con soddisfacente accuratezza. In più, questo confronto mostrerà che nonostante le simulazioni LES siano note per essere più accurate anche se più costose a livello computazionale, le simulazioni RANS rappresentano uno strumento affidabile se è necessario un più basso costo computazionale. Per concludere, questo lavoro sfrutta quindi il basso costo computazionale per riprodurre più scenari utili a valutare come la dispersione degli inquinanti viene modificata a seguito di variazioni delle variabili importanti, come la temperatura.

Introduction

1.1 Objectives

The impact of climate change and meteorological hazards on both cities and the ecosystem is everyday more and more visible, hence nowadays the attention is on studying how to deal with the damages caused by these phenomena. In addition to that, urbanisation and the consequent increase in pollution contribute to the risk to which the ecosystem, people included, is exposed. Of particular interest is the evaluation of the pollutant dispersion mechanism within urban areas, both for sustainable city planning and also for policy decisions for public health. In 2020, 96% of the European urban population was exposed to levels of particulate matter above the health-based guideline level set by the World Health Organization (WHO) resulting in 238.000 premature deaths in the EU-27 (the 27 members of the European Union in 2020), but also causing lung cancer, heart and respiratory diseases. As concerns the Italian territory, the country ranked first for the absolute number of deaths in 2020 due to exposure to $PM_{2.5}$, NO_2 and O_3 [Health impacts of air pollution in Europe, 2022].

For these reasons, it is highly important to fully understand air circulation and pollutant dispersion in urban canyons. Urban areas, with their highly dense population, are particularly exposed to harmful effects such as health diseases and damage to the built and natural environment. In this context, Computational Fluid Dynamics (CFD) simulations represent a useful tool for examining and predicting flow characteristics within urban canyons, especially when it comes to pollutant dispersion.

The aim of this work is to elaborate a set of configurations reproducing diurnal heating of urban canyons to study the impact of convective motions on pollutant dispersion by means of the Reynolds-Averaged Navier-Stokes (RANS) approach and the $k - \varepsilon$ closure model. More specifically, it will be firstly elaborated a model of an urban canopy both in isothermal conditions and with the addition of thermal effects, and then it will be validated against reference data available in the literature. Once assessing the accuracy of the model, the different heating configurations will be generated and the results discussed.

RANS approach is widely adopted in the study of turbulent flows and dispersion in urban canyons because its practical and efficient application, especially when a low

computational cost is needed and multiple configurations are wanted to be explored in a reasonable time. Several authors explored this topic using RANS models. Nguyen et al. [1] implemented a numerical simulation of an urban street canyon using different closure models of the RANS equations, showing the ability of the numerical model to investigate flows and pollutant dispersion in urban street canyons. Salim et al. [2] compared results from RANS and LES simulations in reproducing pollutant dispersion within square urban canyons with avenue-like tree plantings finding that both LES and RANS simulations are in good agreement with experimental measures, but with the LES one improving the prediction of pollutant dispersion because of the wider range of turbulence eddies which is directly resolved by the model.

Since in the present work the aim is to explore several configurations of an heated urban canyon and in particular how convective motions influence the dispersion of a pollutant, the RANS approach is the one chosen to conduct such an investigation.

1.2 Planetary Boundary Layer and Urban Canyons

1.2.1 Planetary Boundary Layer

The study of the climate within the urban environment needs the preliminary definition of the *planetary boundary layer*. The *boundary layer* consists of the lowest 100 to 3000 m of the troposphere of the Earth. It is the portion of the atmosphere we live in and in direct contact with the ground, responding to the surface forcings (frictional drag, evaporation and transpiration, heat transfer, pollutant emission), with a time scale of approximately an hour. The height of the boundary layer ranges from hundred of meters to a few kilometres, depending also on the type of forcing and intensity to which it is subjected to. For example, a key characteristic of the boundary layer over land is the diurnal variation of temperature.

The solar radiation is partly absorbed by the boundary layer, but a greater amount is transmitted to the ground which warms and cools as a response to the solar energy. The resulting fluctuation in physical quantities is known as *turbulence*, a fundamental transport process characterising the boundary layer. Turbulence is superimposed on the mean wind and it usually consists of a variety of eddies of different sizes that behave in a well-ordered manner when displayed in the form of a spectrum. In the boundary layer, most of the turbulence is generated by forcings from the ground, for example solar heating which causes the raising of *thermals* of warmer air, or frictional drag from the flowing of air over the terrain, causing wind shears to develop. Moreover, obstacles present on the ground, such as trees or buildings, can deflect the flow and cause *turbulent wakes*, and disturbances in the atmosphere, near or downwind of the obstacle. The spectrum of the turbulent eddies ranges from the whole depth of the boundary layer, which is 100 to 3000 m in diameter, to the smallest ones with a size of the order of a few millimetres.

The former are the most intense, being directly produced by the forcings of the ground, while the smallest one are produced from the breaking of larger eddies, in a process called *energy cascade*, and are very weak. It is the great ability of turbulence in transporting quantities that allows the boundary layer to respond to the surface forcing and makes it the most important feature of such a layer. Hence, quantities such as moisture, heat, momentum and pollutants are transported horizontally by the mean wind (advection) and in the vertical by turbulence. Usually, the study of physical quantities in the boundary layer is done by splitting the variables into a mean and a perturbation part. The former accounts for the effects of the mean quantities, while the perturbation part either the wave effect or the turbulence one is superimposed on the mean wind [3].

Turbulence in the boundary layer is described in terms of the Reynolds number (Re), a dimensionless number which represents the ratio between inertial and viscous forces. A low Reynolds number indicates that the fluid is characterised by a laminar flow, while a high value of the Reynolds number describes a turbulent flow, with chaotic changes of pressure and velocity. The critical value of Re that marks the distinction between the two regimes of the flow depends on the nature and level of the disturbances: the critical Re_c in a pipe flow is approximately 2000, while for a water tank is 100. In a typical convective boundary layer, the Reynolds number is very high ($Re \sim 10^8$) thus the PBL turbulence is considered "fully developed".

Due to the daily variation of solar radiation, there are three main layers of the PBL:

- the *convective boundary layer* (CBL);
- the *residual layer*;
- the *stable boundary layer* (SBL).

A graphical visualisation of the diurnal variation of the PBL is shown in Fig. 1.1.

The *convective boundary layer* is the result of the daytime heating of the ground by solar radiation. The main mechanism driving the turbulence is thus the buoyancy which generates thermal instability and then turbulence. The convective boundary layer is in turn divided into three sub-layers: the *surface layer*, the *mixed convective layer* and the *entrainment zone*. The surface layer is in direct contact with the ground and is characterised by a negative vertical temperature gradient, while the entrainment zone is the layer at the top with a positive vertical temperature gradient. The mixed layer has a very weak temperature gradient. This partitioning of the CBL is displayed in Fig. 1.2 using the mean vertical profiles characterising it. In this way, following the static stability conditions, if a particle is released at the street it goes up toward the mixed layer up to the entrainment layer where it is pushed again down toward the street, and the

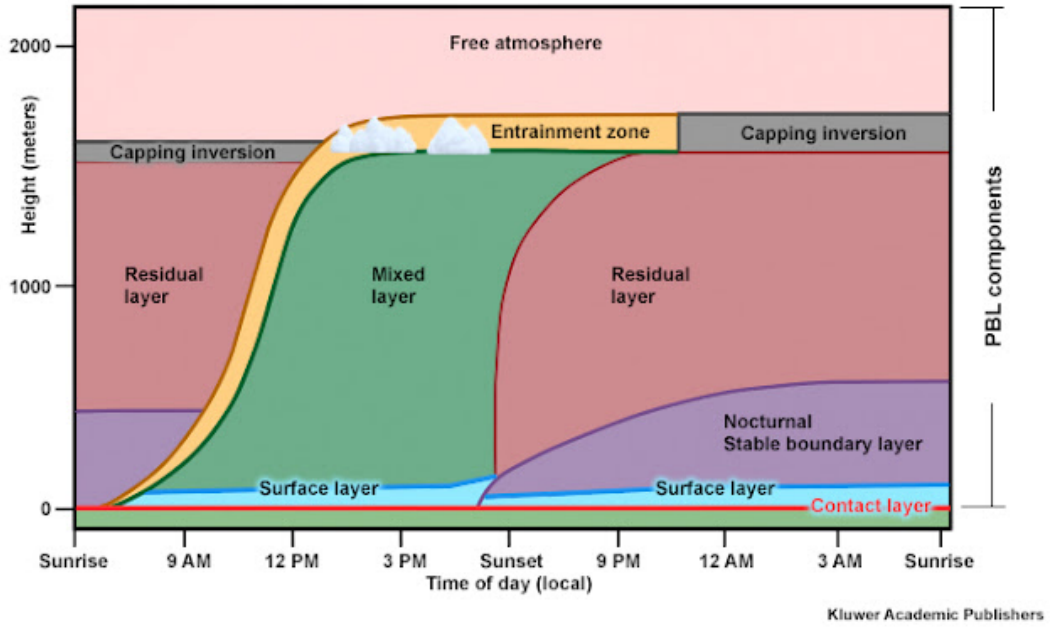


Figure 1.1: Diurnal variation of the planetary boundary layer. Image from [MetEd UCAR].

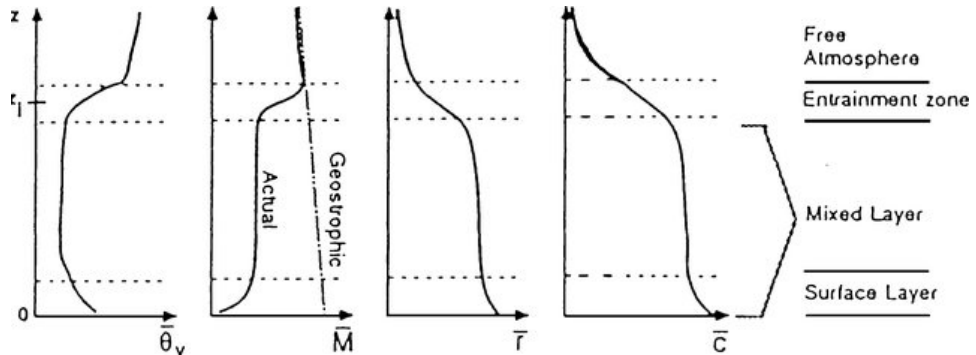


Figure 1.2: Typical daytime vertical profiles of mean virtual potential temperature θ_v , mean wind speed M (with $M^2 = u^2 + v^2$, where u and v are the components of the wind velocity), water vapor mixing ratio r and pollutant concentration c . Image from Stull [3].

overall layer acts like a trap for the pollutants.

Passing to the nighttime the forcing of the solar heating disappears and a negative

buoyancy flux is established which damps the turbulence. This results in the formation of a layer in which there are still some reminiscences of the turbulence (the *residual layer*) and below that, the *stable boundary layer*, characterised by statically stable air. Typical vertical profiles of physical quantities measured by Choi et al. [4] with radiosondes during nighttime are shown in Fig. 1.3. Finally, it is worth noticing that the residual layer is not a proper boundary layer as it is not in direct contact with the ground, thus it is not affected by turbulent transport at the surface, contrary to the definition of the boundary layer (Stull [3]).

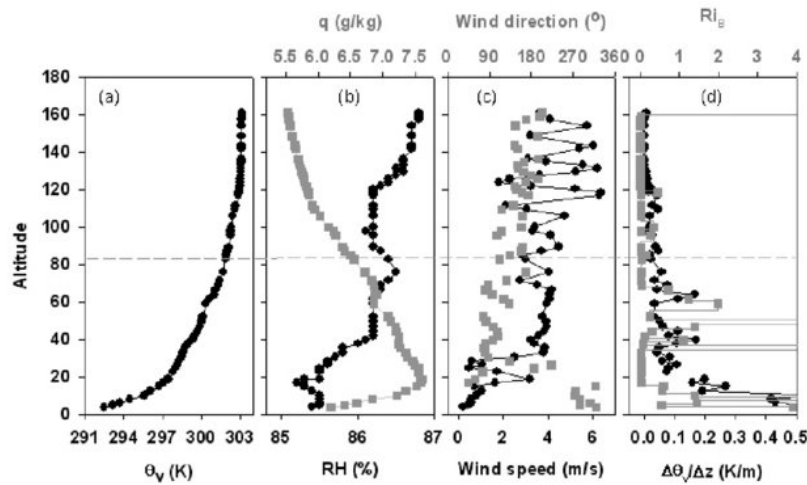


Figure 1.3: Typical nighttime vertical profiles of mean virtual potential temperature θ_v , specific (q) and relative (RH) humidity, wind speed and direction, and vertical gradient of θ_v and bulk Richardson number (Ri_b) for the radiosonde flight launched at 01:25 PST of 9 July 2009. Image from Choi et al. [4].

1.2.2 Urban Boundary Layer and Urban Canyons

In this context, Britter and Hanna [5] identified four major spatial scales to study the dynamics and the dispersion of materials: the *regional scale* ($\sim 100\text{ km}$), the *city scale* ($\sim 10\text{ km}$), the neighbourhood scale ($\sim 1\text{ km}$) and the street scale ($\sim 100\text{ m}$). The regional scale is characterised by mean synoptic meteorological patterns and a displacement of the streamlines of the flow field caused by the urban area, as well as changes to the surface-energy budget and the thermal structure. The diameter of the average urban area defines the city scale, and modifications in the flow and dispersion around buildings are for the most part average out. At the neighbourhood scale the attention is more focused on the dynamic within the canyon because the wind flow can be different moving from one neighbourhood to the next one. Finally, the street scale is the one where flow and

dispersion are studied within two streets, buildings and intersections, and the one used for assessing pedestrian comfort and pollutant exposure.

At the urban scale, three major sublayers can be recognised: the *urban canopy layer*, the *roughness sublayer* and the *inertial sublayer*. These are displayed in Fig. 1.4. In the inertial sublayer the boundary layer shows mostly a vertical displacement of the flow field, hence it is analysed through standard atmospheric boundary-layer formulas. In the urban canopy layer, the flow is directly influenced by the presence of obstacles, and this is even more evident in the urban canopy layer. Hence, in the inertial sublayer the mean wind profile is in the usual logarithmic form, while in the lower urban canopy layer the profile is essentially exponential.

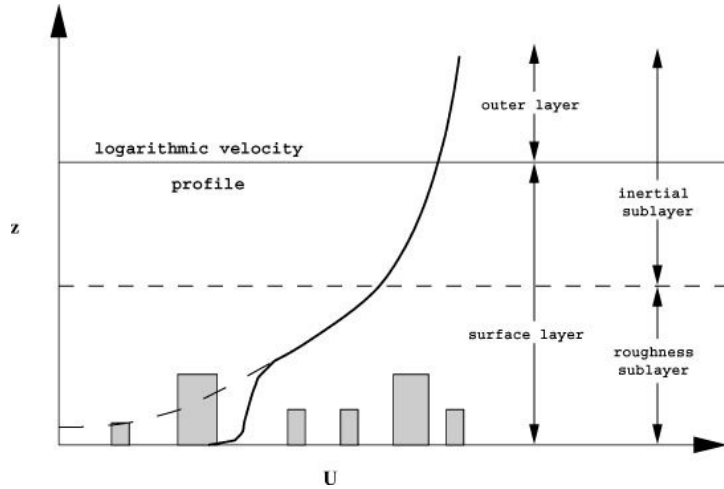


Figure 1.4: Spatially averaged mean velocity profile at the urban scale. Image from Britter and Hanna [5].

The *urban boundary layer* was first defined by Oke [6] as that portion of the boundary layer influenced from below by the urban area, and in particular by the presence of obstacles such as buildings, while the *urban canopy layer* refers to the portion of the air between the urban elements, i.e. buildings. If the former is a mesoscale concept, the latter is a microscale one, hence its climate is the result of the influence given by the elements and the materials therein contained. A schematic representation of those two concepts is displayed in Fig. 1.5.

The most important geometrical parameter defined in the urban canyon context is the *aspect ratio* H/W , where H is the mean building height and W is the mean building width. Depending on the aspect ratio, different flow regimes are established in the urban canyon, as it is illustrated in Fig. 1.6. Suppose that an ambient wind flows from the left side to the right side perpendicular to the canyon axes, the presence of the buildings generates a circulation inside the canyon and depending on the aspect ratio one of the flow regimes is established. When the buildings are well separated ($H/W < 0.3$) they act

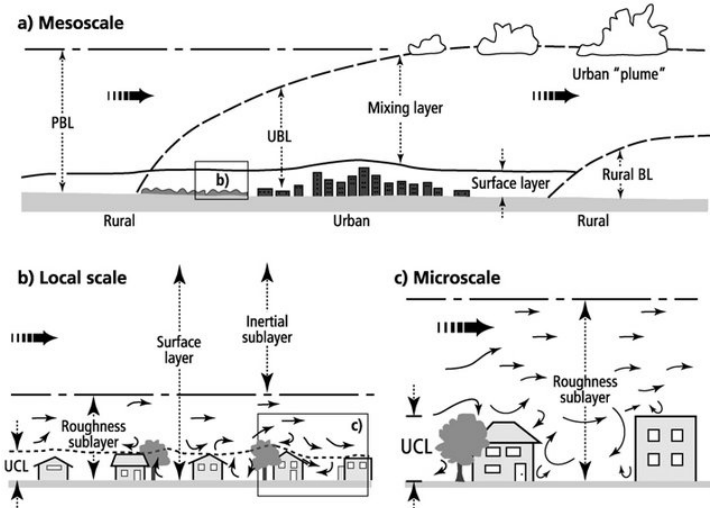


Figure 1.5: Different scales in urban areas. PBL: planetary boundary layer, UCL: urban canopy layer. Image from Oke [7].

as individual buildings and there is enough space between one obstacle and the following for the flow to readjust. This is the *isolated roughness regime*. Decreasing the distance between buildings, hence increasing the aspect ratio, the flow starts to be perturbed and the *wake interference regime* is found. At lower spacing between the buildings, the mesoscale flow above the canyon is almost decoupled from the one within the canyon and a vortex between the building driven by the weak tangential force provided by the outer flow is generated. This is the *skimming flow regime*. These mechanisms are well understood, but the critical value of the aspect ratio H/W at which one regime is discernible from the others is pretty limited [8].

Urban canyons have a large influence on the atmospheric boundary layer, affecting not only the wind flow but also the temperature and the air quality experienced within the canyon. In this way, they substantially define the life present within them.

1.2.3 Urban Heat Island and Heat Waves

Two main phenomena influence the temperature experienced in urban canyons, causing repercussions on human health and the social-economic environment.

The *Urban Heat Island* (UHI) effect consists in the temperature difference between an urban area and the natural surrounding environment due to the presence of darker surfaces in urban areas compared to the rural ones, thus absorbing more incoming solar radiation and becoming hotter. In particular, this is manifested through changes

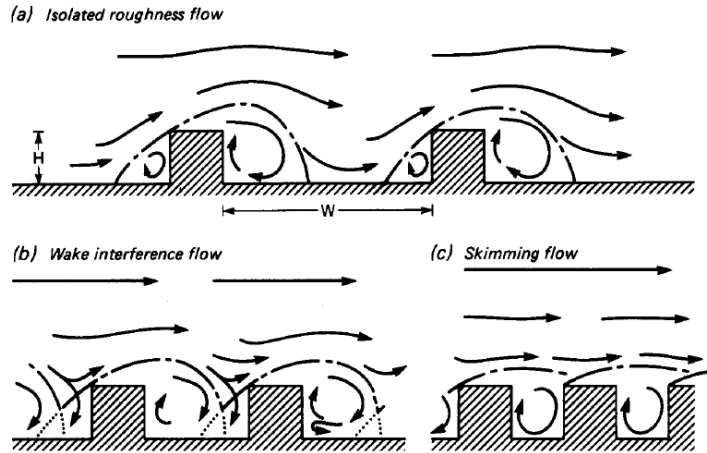


Figure 1.6: Flow regimes for different aspect ratios: (a) $H/W < 1$, (a) $H/W < 1$, (a) $H/W > 1$: skimming flow. Image from Oke [7].

in albedo, thermal capacity and roughness, modifying the overall surface-energy budget [9]. UHI shows seasonal behaviour, with a most noticeable effect during summer and winter. The impacts of UHI strongly depend on its intensity, ranging from advantageous warmer winter nights to negative consequences on human health and the socio-economic environment. UHI has also a significant indirect impact on the elements of the city, such as deterioration of both air and water quality, an increase in air conditioning loads and a reduction of the lifetimes of pavements [10]. UHI as a consequence of urbanisation was first documented by Howard in 1818 [11], hence the increase in the size of urban areas causes an increase also in the intensity of UHI [12]. Therefore, as UHI intensity grows and more and more people move to the cities, this effect is gaining every year more concern because of the repercussions on the health of the population.

Another important phenomenon that characterises cities is *heat waves* (HWs), periods with excessively hot temperatures, sometimes accompanied by high humidity. HWs strongly depend on the region so there is no formal, common definition, but only one with respect to the typical climate of the place and seasonal temperatures. The general definition given by the WMO (World Meteorological Organization) is periods longer than five days where the daily maximum temperature is higher than the average maximum temperature by $5C(9F)$ or more. Therefore, in studying the phenomenon, each author chooses the one he deems most appropriate [13]. The research on heat waves is gaining more importance within the field of climate change because of their impact on society; according to WHO, they are among the most dangerous natural hazards, with more than 166000 deaths caused in the period from 1998 to 2017. Guerreiro et al. [14] presented a study in which they asses the impact of future changes in floods, heat waves (HW),

and droughts for a database of European cities and found an increase in HW days across all cities, especially those in the south, with the higher HW temperature increase in the central European area. Focusing on the Italian territory, they found that Bologna, Cremona, Modena and Reggio nell'Emilia have a high probability of increased number and magnitude of HW and droughts.

In the Sixth Assessment Report of IPCC (Intergovernmental Panel on Climate Change) [15] it is stated that future urbanisation will contribute to amplifying the warming of urban areas due to the urban geometry, human activities and materials that make up cities, and also to increase the loss of biodiversity and material consumption, therefore a more inclusive and judicious urban planning is needed if the goal of more sustainable cities is wanted to achieve.

1.3 State of the Art

The definition of urban canyons and their microclimate dates back to the 70s with the studies conducted by T. R. Oke. In [6] he defines the urban canyon as the basic urban surface unit consisting of the walls and the ground between two adjacent buildings, surrounded at the top by an imaginary lid at the roof level and the bottom by the street. Even in the last century, the problems connected to urbanisation and pollution were well-known, hence the aim of Oke was to find a physical framework for better urban planning.

Air pollution in urban canyons is highly documented because of the huge importance of this topic on everyday life. Given the enormous extent of the subject, it requires research in multiple fields, such as basic fluid mechanics, meteorology, chemistry, mathematics and computer science, and requires both field measurement and laboratory experiments. For example, Taseiko et al. [16] proposed a semi-empirical mathematical model to estimate dispersion of vehicular air pollution in urban street canyons using detailed parameters to explicitly describe the arrangement of the buildings, while Ehrnsperger and Klemm [17] combined fast-response air quality measurements with highly resolved traffic information to examine temporal patterns and sources of air pollutants in urban canyons, making a clear statement about the urgency of decreasing traffic density within city centres to reduce exposure to air pollution of citizens.

Many parameters are involved in the description of the pollutant dispersion process, including ambient conditions (wind speed and direction), building geometry and street dimensions, and also vehicular movement. Laboratory experiments and their results are essential for the validation of numerical simulations. Measurements obtained in laboratories of air dispersion include water channel experiments, such as the one conducted by Li et al. [18] where the flow characteristics inside an urban street canyon were studied for different canyon aspect ratios. Another water channel experiment is the one

conducted by Chew et al. [19] for three different aspect ratio aimed to investigate the discrepancy found in the number of vortices arising in canyons with aspect ratio near the unity between results of reduced-scale experiments and one full-scale field measurements. Brown et al. [20] performed a wind tunnel experiment with six two-dimensional canyons to measure the three components of the velocity field where the flow reaches the equilibrium. Michioka et al. [21] investigated the pollutant removal mechanism from a two-dimensional street canyon with unity aspect ratio using both a LES simulation and a wind tunnel experiment, finding great agreement between the two. Other wind tunnel experiment examples from which concentration profiles are obtained are given by Pavageau et al. [22] and Meroney et al. [23], with the latter aiming to investigate the influence of street geometry in the dispersion of pollutants in street canyons. All of these studies are used in the present work for the validation of the model.

A common technique used to study urban canyons and predict flow patterns is using numerical simulations obtained by means of Computational Fluid Dynamics (CFD). Cintolesi et al. [24] used a Large-Eddy Simulation (LES) to show how introducing an obstacle on the building roof of an urban canyon can be effective in enhancing the removal of a pollutant within the canyon. The thermal effect, resulting from variations of the solar heating of canyons walls, can be included to have a better understanding of the flow behaviour during diurnal heating. Memon and Leung [25] conducted an investigation on how the velocity and temperature patterns change in urban canyons with different aspect ratio and heating configurations through RANS simulations, showing that the highest temperature within the canyon arises with the heating on the windward wall. Further considerations on the modification of the pollutants within the canyon under a similar heating configuration are presented by Cintolesi et al. [26], where a LES simulation was used to conduct such investigation, and Xie et al. [27], which used a Renormalisation Group (RNG) $k - \varepsilon$ turbulence theory to model the turbulent motions and transport. Another examination of the influence of thermal effects on tracers dispersion in urban canyons is given by Xie et al. [28], where the authors found that the heating of the leeward wall results in the strengthening of the primary vortex arising in neutral conditions, while for the windward heated wall such vortex is found divided in two counter-rotating vortices.

1.4 Structure of the thesis

The present work is organised as follows.

The first chapter, the present one, illustrates the background within which this work is contextualised, the urban boundary layer and the urban canyon, together with the effects of climate change experienced by the latter, and finally the state of the art of the research on urban canyons.

The second chapter will deal with the mathematical framework on which this thesis is based. More specifically, it will first introduce the set of the governing equations, then the basic idea behind Computational Fluid Dynamics (CFD) and the approach implemented in this work, the Reynolds-Averaged Navier-Stokes (RANS) simulations together with the turbulence model chosen, the $k-\varepsilon$ model, and finally the software used, OpenFOAM.

The third chapter will go deeper into the methodology implemented and the description of the problem. In the first part, the geometry of the case study, the algorithm and the numerical schemes applied will be described, together with the non-dimensional parameters that characterise the system and allow a comparison with other studies. The second part of this chapter is left for the validation of the model. In particular, will be first carried a validation of the CFD simulations under neutral conditions, then with the upwind building facade heated.

In the fourth chapter, the different configurations of heating of the building facades and the results of the simulations will be illustrated and discussed, with a final comparison between the same heating configurations under increased temperature difference between solid walls and air.

The fifth and final chapter is dedicated to the conclusions of the present thesis.

Simulation methodology

The purpose of this chapter is to provide an overview of the methodology used. It is divided into two main parts: the former deals with the mathematical framework while the latter with the modelling. In the second part of this chapter will be illustrated a description of the simulation approach and the Reynolds-Averaged Navier-Stokes (RANS) modelling, together with the equations involved. The chapter will conclude with a brief description of the software used.

2.1 Governing equations

The motion of a viscous fluid is described by the Navier-Stokes equations, partial differential equations arising from applying Newton's second law to fluid motion, mathematically expressing the conservation of momentum and conservation of mass for Newtonian fluids. They sometimes go with further equations that describe other properties of the system. The general formulation of the equations used in this work consists of the Navier-Stokes equations, i.e. the momentum equation and the conservation of mass, the equation of temperature and the equation of the concentration of a pollutant (both derived from the conservation of a passive scalar):

$$\left\{ \begin{array}{l} \frac{D\rho}{Dt} + \rho \frac{\partial u_j}{\partial x_j} = 0, \\ \frac{Du_i}{Dt} = -\delta_{i3}g + f\epsilon_{ij3}u_j - \frac{1}{\rho} \frac{\partial p}{\partial x_i} + \nu \frac{\partial^2 u_i}{\partial x_j^2}, \\ \frac{D\theta}{Dt} = \alpha \frac{\partial^2 \theta}{\partial x_j^2} + S_\theta, \\ \frac{Dc}{Dt} = \lambda \frac{\partial^2 c}{\partial x_j^2} + S_c. \end{array} \right. \quad (2.1a)$$

$$(2.1b)$$

$$(2.1c)$$

$$(2.1d)$$

where ρ is the density of the fluid, (i, j, k) are indices, the velocity vector u_i has three components (u, v, w) , $g = 9.81 \text{ m/s}^2$ is the gravity acceleration vector modulus, δ_{ij} is

the Kronecker delta, ϵ_{ijk} is the Levi-Civita symbol, p is the pressure, $\nu \equiv \mu/\rho$ is the kinematic viscosity, θ is the potential temperature, α is the thermal diffusivity, c is the concentration (mass per volume) of the tracer, λ is the molecular pollutant diffusivity, S_c and S_θ are the body source term, and where the material derivative is defined as

$$\frac{D}{Dt} \equiv \frac{\partial}{\partial t} + u_i \frac{\partial}{\partial x_i}.$$

This set of equations is very complex and no analytical solution is known. Moreover, the aforementioned set of equations needs satisfactory knowledge of the initial and boundary conditions to resolve the whole range of the turbulence scale, which we do not have. Hence, an approximate solution is the only option available. One can choose either to find a simplified subset of equations for which an analytical solution is possible, or to solve a more complete set of equations via numerical simulations. In this work, we choose to take the second path. Adopting the assumptions of incompressible fluid and the Boussinesq approximation for the buoyancy term, the governing equations 2.1 simplify as:

$$\left\{ \begin{array}{l} \frac{\partial u_i}{\partial x_i} = 0, \\ \frac{\partial u_i}{\partial t} + u_j \frac{\partial u_i}{\partial x_j} = -\frac{\partial p^*}{\partial x_i} + \nu \frac{\partial^2 u_i}{\partial x_j \partial x_j} - g_i \beta |T|, \\ \frac{\partial T}{\partial t} + u_i \frac{\partial T}{\partial x_i} = \alpha \frac{\partial^2 T}{\partial x_i \partial x_i}, \\ \frac{\partial c}{\partial t} + u_i \frac{\partial c}{\partial x_i} = \lambda \frac{\partial^2 c}{\partial x_i \partial x_i}. \end{array} \right. \quad (2.2a)$$

$$(2.2b)$$

$$(2.2c)$$

$$(2.2d)$$

where $p^* = (p - \rho_0 g_i x_i)/\rho_0$ is the pressure deviation from the kinematic hydrostatic pressure, ρ_0 is the constant reference density, β is the thermal expansion coefficient, T is the perturbation of the temperature given by $T = \theta - \theta_0$, where θ and θ_0 are the actual and ambient potential temperature, respectively, g_i is the gravity acceleration vector.

2.2 Numerical approach and modelling

The branch of fluid mechanics that uses numerical analysis and algorithms to solve problems involving fluid flows is Computational Fluid Dynamics (CFD). CFD is based on the governing equations of the system under examination. For this reason, CFD models are widely used in environmental modelling. Whatever the problem is, the standard procedure adopted by CFD models is the following:

1. The *pre-processing* involves the definition of the geometry and physical boundaries,

together with the creation of the grid of the computational fields and the physical modelling (i.e. the equations to be solved);

2. then, the *solver* computes the variables using the mathematical equations pre-scribed;
3. finally, the *post-processor* displays and analyses the numerical results.

In numerical simulation an important step involves the choice of the discretization method, meaning how to translate continuous functions and equations into a discrete equivalent. There are plenty of approaches to discretization depending on the problem considered, for example, if there is a time dependence. In this work, we deal with steady-state solutions of a two-dimensional system therefore a natural choice is that of the finite volume method (FVM). In this technique, the attention is focused on a finite region of the flow, reasonably large, instead of the whole flow field, and the fundamental physical principles are applied to the fluid inside the control volume and to that crossing it. Further considerations about different discretization methods can be found in [29].

The objective of computational modelling of turbulence flows is to realise a model able to predict quantities of interest by solving the set of equations characterising the problem. However, as previously mentioned, resolving the whole range of length scales of turbulence is excessively expensive, and sometimes we are not even interested in predicting all eddy motions, hence we instead choose a threshold eddy size below which are included only the statistical effects of turbulence. Depending on the range of scales resolved various turbulence models are available:

- *DNS* (Direct Numerical Simulations), where the Navier-Stokes equations are numerically solved without involving any turbulence model and resolving the whole range of the turbulence scales. These simulations are the most accurate possible but they are so computationally expensive that are used only to flows with low or moderate Reynolds numbers;
- *RANS* (Reynolds-averaged Navier-Stokes) with whom the mean velocity field is determined and the Reynolds stresses are obtained from a turbulent viscosity model;
- *LES* (Large Eddy Simulations), where the larger-scale turbulent motions are directly resolved, while the smaller ones are left to parametrisation. The computational expense is less than the DNS one, but greater than RANS, gaining in accuracy compared to the latter.

2.2.1 RANS

In this section, we will focus on Reynolds Averaged Navier Stokes (RANS) models and the RANS equations will be derived. More detailed information about the mathematical

framework here reported can be found in Pope [30].

Firstly, to derive the RANS set of equations from the Navier-Stokes equations we introduce the Reynolds decomposition in which the flow variables are separated into a mean and fluctuation part. Taking the velocity as an example we have:

$$u_i(\mathbf{x}, t) \equiv \langle u_i \rangle(\mathbf{x}, t) + u'_i(\mathbf{x}, t), \quad (2.3)$$

where $\langle u_i \rangle$ is the mean component and u' is the fluctuating part, and where the mean operation for a generic variable ψ is defined as:

$$\langle \psi \rangle = \frac{1}{T} \int_0^T \psi dt, \quad (2.4)$$

where T is longer than the turbulent time scale. Since the mean and the differentiation commute, from the continuity equation (Eq. 2.2a) we get:

$$\frac{\partial \langle u_i \rangle}{\partial x_j} = 0 \quad (2.5)$$

Now we derive the mean of the momentum equation (Eq. 2.2b). We start writing the material derivative in conservative form,

$$\frac{Du_j}{Dt} = \frac{\partial u_j}{\partial t} + \frac{\partial}{\partial x_i} (u_i u_j),$$

and taking the mean of this equation

$$\left\langle \frac{Du_j}{Dt} \right\rangle = \frac{\partial \langle u_j \rangle}{\partial t} + \frac{\partial}{\partial x_i} \langle u_i u_j \rangle. \quad (2.6)$$

The Reynolds decomposition of the nonlinear term of this equation reads

$$\begin{aligned} \langle u_i u_j \rangle &= \langle (\langle u_i \rangle + u'_i)(\langle u_j \rangle + u'_j) \rangle \\ &= \langle \langle u_i \rangle \langle u_j \rangle + u'_i \langle u_j \rangle + u'_j \langle u_i \rangle + u'_i u'_j \rangle \\ &= \langle u_i \rangle \langle u_j \rangle + \langle u'_i u'_j \rangle. \end{aligned}$$

where the nonlinear term

$$\tau_{ij} = \langle u'_i u'_j \rangle \quad (2.7)$$

is called *Reynolds stresses tensor*. Substituting Eq. 2.7 into Eq. 2.6 we obtain:

$$\left\langle \frac{Du_j}{Dt} \right\rangle = \frac{\partial \langle u_j \rangle}{\partial t} + \frac{\partial}{\partial x_i} (\langle u_i \rangle \langle u_j \rangle + \langle u'_i u'_j \rangle) = \frac{\partial \langle u_j \rangle}{\partial t} + \langle u_i \rangle \frac{\partial \langle u_j \rangle}{\partial x_i} + \frac{\partial}{\partial x_i} \langle u'_i u'_j \rangle. \quad (2.8)$$

Taking the mean of the momentum equation (Eq. 2.2b) without any body forces we obtain the equation for the mean-momentum

$$\left\langle \frac{Du_j}{Dt} \right\rangle = \frac{\partial \langle u_j \rangle}{\partial t} + \langle u_i \rangle \frac{\partial \langle u_j \rangle}{\partial x_i} - \frac{1}{\rho} \frac{\partial \langle p \rangle}{\partial x_j} + \nu \frac{\partial \langle u_i \rangle}{\partial x_j \partial x_j} + \frac{\partial}{\partial x_i} \langle u'_i u'_j \rangle. \quad (2.9)$$

For sake of clarity, we rewrite the set of the mean equations, together with the equation for the temperature:

$$\begin{cases} \frac{\partial \langle u_i \rangle}{\partial x_i} = 0, \end{cases} \quad (2.10a)$$

$$\begin{cases} \frac{\partial \langle u_i \rangle}{\partial t} + \langle u_j \rangle \frac{\partial \langle u_i \rangle}{\partial x_j} = -\frac{1}{\rho} \frac{\partial \langle p \rangle}{\partial x_j} + \nu \frac{\partial \langle u_i \rangle}{\partial x_j \partial x_j} - \frac{\partial \langle u'_i u'_j \rangle}{\partial x_j} \end{cases} \quad (2.10b)$$

$$\begin{cases} \frac{\partial \langle T \rangle}{\partial t} + \langle u_j \rangle \frac{\partial \langle T \rangle}{\partial x_j} = \alpha \frac{\partial^2 \langle T \rangle}{\partial x_j \partial x_j}. \end{cases} \quad (2.10c)$$

We now take a moment to briefly discuss the properties of the Reynolds stresses.

We can easily understand how Reynolds stresses $\langle u'_i u'_j \rangle$ have a crucial role in the momentum equation: in fact, the difference between the equations for $u_i(\mathbf{x}, t)$ and $\langle u_i(\mathbf{x}, t) \rangle$ can be associated with the presence of such term.

The RANS equation for the momentum can be rewritten as:

$$\frac{\partial \langle u_i \rangle}{\partial t} + \langle u_j \rangle \frac{\partial \langle u_i \rangle}{\partial x_j} = \frac{1}{\rho} \frac{\partial}{\partial x_j} \left[2\nu \frac{1}{2} \left(\frac{\partial \langle u_i \rangle}{\partial x_j} + \frac{\partial \langle u_j \rangle}{\partial x_i} \right) - \langle u'_i u'_j \rangle - p \delta_{ij} \right]. \quad (2.11)$$

The term in square brackets represents the sum of three stresses: the viscous stress, the isotropic stress $-p \delta_{ij}$ from the mean pressure field, and the stress arising from the fluctuation of the velocity field, $-\rho \langle u'_i u'_j \rangle$. Since the viscous term originates from momentum transfer at the molecular level, the Reynolds stresses arise from the momentum transfer by the fluctuating velocity field as well.

Another important property of the Reynolds stresses tensor is given by the fact that the turbulent kinetic energy $k(\mathbf{x}, t)$ can be derived from the trace of this term:

$$k \equiv \frac{1}{2} \langle u'_i u'_j \rangle = \frac{1}{2} \text{tr}(\tau_{ij}) \quad (2.12)$$

A further important feature of the Reynolds stresses arises from the following decomposition:

$$\tau_{ij} = \frac{2}{3} k \delta_{ij} + \langle u'_i u'_j \rangle - \frac{2}{3} k \delta_{ij}. \quad (2.13)$$

The first term is the isotropic stress, the last two terms correspond to the anisotropic stress τ_{ij}^a which is the only component effective in transporting momentum. Eq. 2.11 can be rewritten absorbing the isotropic stress in a modified mean pressure:

$$\frac{\partial \langle u_i \rangle}{\partial t} + \langle u_j \rangle \frac{\partial \langle u_i \rangle}{\partial x_j} = \frac{1}{\rho} \frac{\partial}{\partial x_j} (2\nu S_{ij} - \tau_{ij}^a) - \frac{1}{\rho} \frac{\partial}{\partial x_j} \left(\langle p \rangle \delta_{ij} + \frac{2}{3} k \delta_{ij} \right). \quad (2.14)$$

At this point we have four equations, three from the momentum equations (Eq. 2.14) and the other one given by the continuity equation (Eq. 2.10a), However, considering also the Reynolds stress, we get to ten unknowns: this is addressed as the *closure problem*. To solve the system we need more equations from which Reynolds stresses can be determined. A way to do so is by using *turbulent viscosity models* which are based on the *eddy-viscosity hypothesis*. According to the hypothesis, the Reynolds stresses are given by

$$\tau_{ij}^a = \langle u'_i u'_j \rangle - \frac{2}{3} k \delta_{ij} = -\nu_T \left(\frac{\partial \langle u_i \rangle}{\partial x_j} + \frac{\partial \langle u_j \rangle}{\partial x_i} \right) = -2\nu_T S_{ij}, \quad (2.15)$$

The next step consists in determining an appropriate specification of the turbulent viscosity $\nu_T(\mathbf{x}, t)$. This can be written as the product of a velocity $u^*(\mathbf{x}, t)$ and a length $l^*(\mathbf{x}, t)$:

$$\nu_T = u^* l^*, \quad (2.16)$$

and in this way ν_T can be assigned by specifying u^* and l^* . In two-equation models as the $k - \varepsilon$ model, as we'll later see, u^* and l^* are related to k and ε , for which modelled transport equations are solved.

The turbulent-viscosity model although having some limitations, still allows a simplification of the equations of motion and a closure for the system:

$$\begin{cases} \frac{\partial \langle u_i \rangle}{\partial x_i} = 0, \end{cases} \quad (2.17a)$$

$$\begin{cases} \frac{\partial \langle u_i \rangle}{\partial t} + \langle u_j \rangle \frac{\partial \langle u_i \rangle}{\partial x_j} = -\frac{1}{\rho} \frac{\partial \langle p \rangle}{\partial x_i} + \frac{\partial}{\partial x_j} \left[(\nu + \nu_T) \frac{\partial \langle u_i \rangle}{\partial x_j} \right]. \end{cases} \quad (2.17b)$$

Since in this work we deal with scalars too, it is worth recalling also the gradient-diffusion hypothesis. Considering the temperature, this hypothesis reads:

$$\langle u'_i T' \rangle = -\alpha_T \frac{\partial \langle T \rangle}{\partial x_i}. \quad (2.18)$$

where α_T is the turbulent diffusivity. Eq. 2.18 express the fact that the scalar flux $\langle u'_i T' \rangle$ is aligned with the mean scalar gradient. Hence, the temperature equation (Eq. 2.10c) becomes

$$\frac{\partial \langle T \rangle}{\partial t} + \langle u_j \rangle \frac{\partial \langle T \rangle}{\partial x_j} = \frac{\partial}{\partial x_j} \left[(\alpha + \alpha_T) \frac{\partial \langle T \rangle}{\partial x_j} \right]. \quad (2.19)$$

The turbulent Prandtl number Pr relates ν_T with α_T :

$$\alpha_T = \frac{\nu_T}{Pr} \quad (2.20)$$

2.2.2 The $k - \varepsilon$ model

The $k - \varepsilon$ is an example of *two-equation models*, in which model transport equations are solved for the turbulent kinetic energy (TKE) k and ε .

In the $k - \varepsilon$ model the turbulent viscosity ν_T is given by

$$\nu_T = C_\mu \frac{k^2}{\varepsilon}, \quad (2.21)$$

where $C_\mu = 0.009$ is empirically determined.

Expression for k and ε are found from the equation describing the evolution of a general fluid dynamic quantity:

$$\frac{D\phi}{Dt} = \text{diffusion} + \text{production} - \text{dissipation} \quad (2.22)$$

Expanding this equation and writing it for both the TKE k and the dissipation ε , the equations that close the system 2.10 are:

$$\left\{ \begin{aligned} \frac{\partial k}{\partial t} + \langle u_i \rangle \frac{\partial k}{\partial x_i} &= \frac{\partial}{\partial x_j} \left(\frac{\nu_T}{\sigma_k} \frac{\partial k}{\partial x_j} \right) + P_k - \varepsilon \\ \frac{\partial \varepsilon}{\partial t} + \langle u_i \rangle \frac{\partial \varepsilon}{\partial x_i} &= \frac{\partial}{\partial x_j} \left(\frac{\nu_T}{\sigma_\varepsilon} \frac{\partial \varepsilon}{\partial x_j} \right) + C_{1\varepsilon} \frac{\varepsilon}{k} P_k - C_{2\varepsilon} \frac{\varepsilon^2}{k} \end{aligned} \right. \quad (2.23a)$$

$$\left. \begin{aligned} \frac{\partial \varepsilon}{\partial t} + \langle u_i \rangle \frac{\partial \varepsilon}{\partial x_i} &= \frac{\partial}{\partial x_j} \left(\frac{\nu_T}{\sigma_\varepsilon} \frac{\partial \varepsilon}{\partial x_j} \right) + C_{1\varepsilon} \frac{\varepsilon}{k} P_k - C_{2\varepsilon} \frac{\varepsilon^2}{k} \end{aligned} \right. \quad (2.23b)$$

where P_k is the production rate of k by the mean flow. From the turbulent viscosity model:

$$P_k = \nu_T \left(\frac{\partial \langle u_i \rangle}{\partial x_j} + \frac{\partial \langle u_j \rangle}{\partial x_i} \right) \frac{\langle u_i \rangle}{\partial x_j}. \quad (2.24)$$

The $k - \varepsilon$ model constants are adjustable; in this work they are set to $C_{1\varepsilon} = 1.44$, $C_{2\varepsilon} = 1.92$, $\omega_k = 0.09$, $\omega_\varepsilon = 1.11$.

2.2.3 OpenFOAM

OpenFOAM (Open Source Field Operation and Manipulation) is a free open-source software for computational fluid dynamics from the OpenFOAM Foundation [OpenFOAM]. More specifically, OpenFOAM is a C++ library used to create executables, known as applications, which are precompiled but the user can also create their own or modify existing ones. There are two main categories of applications:

- *solvers*, designed to solve a specific problem in computational continuum mechanics;
- *utilities*, that perform simple pre-and post-processing tasks, mainly involving data manipulation and algebraic calculations.

In this thesis, it has been used version 6 of the OpenFOAM.

A standard steady-state solver for an incompressible, turbulent flow is `simpleFoam` which uses the SIMPLE algorithm. Here `simpleFoam` has been adapted to include the buoyancy term into the momentum equation and to solve the equation of the concentration too, as can be seen in Eqs. 2.2, and where the temperature equation (Eq. 2.2c) and the momentum equation (Eq. 2.2d) has been written in terms of the buoyancy force $b_i = \beta g_i T$.

The source code for the momentum equation of the SIMPLE algorithm is contained in the `UEqn.H` file, where the stationary Eq.2.2(b) is resolved. The additional buoyancy term has been introduced by adding a buoyancy force written in terms of `b`, the magnitude of the buoyancy force, and `l`, the unity vertical vector directed downward.

```

1 // Momentum predictor
2
3 MRF.correctBoundaryVelocity(U);
4
5 tmp<fvVectorMatrix> tUEqn
6 (
7     fvm::div(phi, U)
8 //     + MRF.DDt(U)
9     + turbulence->divDevReff(U)
10    ==
11 //    Added to pull gravity out of pressure term
12    - b*l
13    + fvOptions(U)
14 );
15 fvVectorMatrix& UEqn = tUEqn.ref();
16
17 UEqn.relax();
18
19 fvOptions.constrain(UEqn);
20
21 if (simple.momentumPredictor())
22 {
23     solve(UEqn == -fvc::grad(p));
24
25     fvOptions.correct(U);
26 }
```

The file `bEqn.C` contains the source code for the temperature equation 2.2(c) in a stationary form, written in terms of the buoyancy force. The first lines of the code show the calculation of the turbulent thermal diffusivity and the "effective" thermal diffusivity, given by the sum of the molecular and the turbulent ones. Then, the buoyancy equation

is discretised and resolved.

```

1 // Buoyancy equation
2
3 {
4     alphat = turbulence->nut()/Prt;
5     alphat.correctBoundaryConditions();
6
7     volScalarField alphaEff("alphaEff", turbulence->nu()/Pr + alphat);
8
9     fvScalarMatrix bEqn
10    (
11        + fvm::div(phi, b)
12        ==
13        + fvm::laplacian(alphaEff, b)
14    );
15
16     bEqn.relax();
17
18     fvOptions.constrain(bEqn);
19
20     bEqn.solve();
21
22     fvOptions.correct(b);
23 }
```

Lastly, the code below refers to the `cEqn.C` file containing the source code for the resolution of the stationary form of the concentration equation 2.2(d). As before, firstly the turbulent molecular diffusivity and the "effective" molecular diffusivity, given by the sum of the molecular and the turbulent ones, are calculated, then the concentration equation is discretised and resolved. The final clipping part is added to delete all the possible negative values of the concentration, thus stabilising the calculation.

```

1 // Concentration equation
2
3     lambdat = turbulence->nut()/Sct;
4     lambdat.correctBoundaryConditions();
5
6     volScalarField lambdaEff("lambdaEff", turbulence->nu()/Sc + lambdat);
7
8     fvScalarMatrix cEqn
9     (
10         fvm::div(phi, c)
11         ==
12         fvm::laplacian(lambdaEff, c)
13     );
14
15     cEqn.relax();
16     cEqn.solve();
17
18 // clipping
19     scalar n=0.0;
20
21     forAll(c,pIt)
22     if(c[pIt]<0)
```

```
23     {
24         c[pIt] = scalar(0.0);
25         n=n+1;
26     }
27
28     Info << "           Number of clipped cells: " << n << endl;
29
30 // end clipping
```

Problem description and Validation

This chapter aims to describe the geometry considered and the numerical settings and to provide a validation of the model with numerical and field-experiment datasets.

3.1 Numerical Setup and Physical Parameters

3.1.1 Geometry and computational domain

The case study reproduces an infinite array of two-dimensional square urban canyons with a horizontal background flow perpendicular to the canyon axis. In the centre of the street a constant flux of a passive scalar is released. This work aims to analyse multiple configurations of heating of the solid walls, both horizontal and vertical. For the purpose of the validation, each solid boundary is at the same temperature. Then, imposing a fixed temperature difference on the wall to be heated, the different configurations are obtained. The case geometry is depicted in Fig.3.1. The height and the width of the canyon are $H = 1.0$ m and $W = 1.0$ m (aspect ratio $H/W = 1$) and the computational domain is $2H \times 3H$ long in the streamwise (x) and vertical (y) directions. The ambient flow is directed along the x -direction and is characterised by a free-stream velocity U_{ref} . The pollutant is characterised by a concentration c and it is released at the street level, in a band of width $0.7H$ without extending it to the whole canyon to better reproduce the emission from a roadway. The walls of the buildings are considered as smooth surfaces.

The computational mesh used is the same used by Cintolesi et al. [26]. Starting from this 3D mesh, the 2D mesh has been obtained employing the `extrudeMesh` utility. In summary, the mesh is composed of $144 \times 144 \times 1$ cells in the x, y, z directions, respectively. Furthermore, at the roof level ($z/H = 1$) the cells are stretched to obtain a denser distribution. More information about the refinement procedure can be found in Cintolesi et al. [26]. The final mesh is composed of 20605 cells.

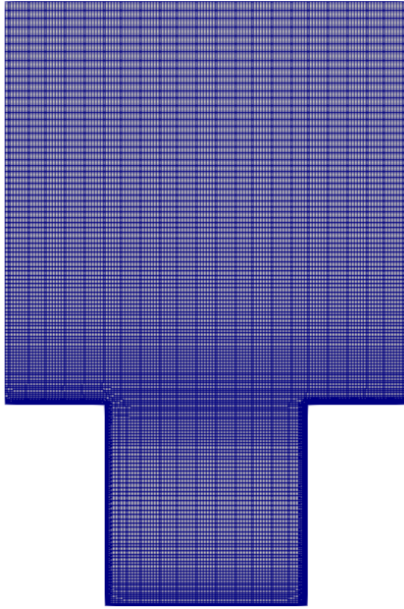


Figure 3.1: Computational mesh

3.1.2 Algorithm and numerical schemes

As mentioned in the previous chapter, the model used in this thesis is the $k-\varepsilon$ turbulence model with constants $C_{1\varepsilon} = 1.44$, $C_{2\varepsilon} = 1.92$, $\omega_k = 0.09$, $\omega_\varepsilon = 1.11$.

Tab. 3.1 summarises the numerical schemes adopted for each term of the equations, such as derivatives and gradients, calculated during the simulations.

As concerns the equation solvers, these are set up as follows. The solver for the pressure p is **GAMG**, while for the other variables, namely U, b, c, k, ε , **smoothSolver**. The **smoother** chosen for all the variables is the **GaussSeidel**. Furthermore, the solver tolerance, **tolerance**, on p is set to 10^{-6} , while on the other quantities on 10^{-12} . Finally, the solver relative tolerance, **relTol**, is set to 0.01 for all of them. The difference between these two last entries is that the solver tolerance represents the level at which the residual is small enough to consider the solution accurate, whereas the solver relative tolerance limits improvements from the initial to the final solution.

Different from the *linear-solver* described above is the *application solver*, in this case a modified **simpleFoam**, which contains the set of equations and algorithms to solve the problem. How this has been modified is illustrated in Section 2.2.3.

sub-dictionary	keyword	scheme
ddtSchemes		steadyState
gradSchemes		Gauss linear
	div(phi,U)	bounded Gauss limitedLinearV 1
	div(phi,epsilon)	bounded Gauss limitedLinear 1
	div(phi,k)	bounded Gauss limitedLinear 1
	div(phi,c)	bounded Gauss limitedLinear 1
	div(phi,b)	bounded Gauss limitedLinear 1
	div((nuEff*dev2(T(grad(U)))))	Gauss Linear
laplacianSchemes		Gauss linear limited corrected 0.33
interpolationSchemes		linear
snGradSchemes		limited corrected 0.33

Table 3.1: Numerical schemes

3.1.3 Initial and boundary conditions

To initialise the simulation a uniform velocity field equal to $u_x = 0.05 \text{ ms}^{-1}$ is imposed, while the other variables are set to zero. To reproduce a flow driven by a pressure gradient, the streamwise velocity at the top boundary is set to $U_{ref} = 20 \text{ ms}^{-1}$. Regarding the boundary conditions, cyclic conditions are imposed for all the variables at the vertical faces to mimic the infinite extension of the case; at the solid walls, no-slip conditions are imposed for velocity, while zero-gradient for pressure and concentration. At the top boundary of the latter, a zero value is imposed, while at the centre of the street boundary a constant flux. At the top boundary, the zero-gradient condition is imposed for all the variables, except for the velocity where, as previously mentioned, a $U_{ref} = 20 \text{ ms}^{-1}$ is imposed. When adding the heating of the solid surfaces, boundary conditions of the buoyancy variable are zero at the top boundary and all the walls are set at the same ambient temperature. Finally, the `nutkWallFunction` is imposed at the vertical boundaries and the street of the turbulent kinetic energy. This condition provides a wall function for the turbulent viscosity based on the turbulent kinetic energy, and an accurate reproduction of the viscous sublayer. In fact, being this layer strongly affected by viscosity, the wall bounded turbulent flow is difficult to reproduce especially for turbulence models, such as the $k - \varepsilon$, that are only valid where the turbulence is fully developed and they do not perform well close to the walls. Therefore, wall functions help with the reproduction of the near wall region. But, to ensure the accuracy of the results, the first cell centre of the turbulence fully developed needs to be in the log-law region, i.e. above the viscous sublayer. This condition can be checked by means of the `yplus` function, defined as

$$y^+ = \frac{yu_\tau}{\nu}$$

where y is the distance from the wall, u_τ is the friction velocity, and ν is the kinematic viscosity. Thus, y^+ represents a non-dimensional distance from the wall, and the condition reads $30 < y^+ < 300$. It is this condition that led to the choice of a U_{ref} of a few orders of magnitude higher than the typical wind values used in this type of experiment.

3.1.4 Non-Dimensional Parameters

The dynamic of the urban canyon is described by means of the *Reynolds number*, defined as

$$Re = \frac{U_{ref}H}{\nu}, \quad (3.1)$$

where ν is the air kinematic viscosity. The Reynolds number is a dimensionless number and a useful indicator of the regime of the flow, being the ratio of inertial to

viscous forcings. At low Reynolds number the flow is laminar, while at high Reynolds number it becomes turbulent. The transition from laminar to turbulent flow occurs when the *critical Reynolds number* has reached, with it ranging from approximately 2300 to 4000. The boundary layer is characterised by $Re \approx O(10^7)$, therefore it is fully turbulent.

The *Grashof number* is defined as the ratio between the buoyancy force and the viscous force acting on the fluid:

$$Gr = \frac{g\beta TH^3}{\nu^2}. \quad (3.2)$$

The Gr can be used to describe natural convection, meaning the fluid motion generated in absence of any external sources but only by the density difference produced by temperature differences within the fluid.

Another important description of the fluid is given in terms of the *Richardson number*, the dimensionless number expressing the ratio between the buoyancy term and the flow shear:

$$Ri = \frac{g\beta TH}{U_0^2} = \frac{Gr}{Re^2} = \frac{U_b^2}{U_0^2} \quad (3.3)$$

where $b = g\beta T$ is the buoyancy force per unit mass between the walls of the canyon, thus $U_b = \sqrt{g\beta TH}$ is the characteristic buoyancy velocity. In this way, Ri can be used to investigate the flow regimes in the canyon. When the Richardson number is less than unity, buoyancy is irrelevant, the flow is inertially-driven and there is no convection; if Ri exceeds unity buoyancy is the dominant force and the canyon is characterised by a natural convection flow. For Ri of the order unity, both forces, thermal and inertial, are significant.

To make a comparison between simulations and experimental data each quantity is made non-dimensional by means of a reference parameter. Velocities profiles are obtained using the free stream velocity U_{ref} . The analyses of the vertical profiles of the concentration are done using the non-dimensional pollutant concentration

$$C^* = \frac{c}{C_{ref}}, \quad (3.4)$$

where $C_{ref} = q/U_{ref}$ is the reference concentration and $q = \lambda \frac{\partial c}{\partial n}$ is the constant pollutant flux per unit area, and where λ is the molecular diffusivity, n is the surface-normal direction.

When one of the solid surfaces is heated up, vertical profiles of the temperature perturbation are shown in terms of a non-dimensional fluctuation temperature given by:

$$T^* = \frac{T}{\Delta T}. \quad (3.5)$$

Reynolds	Re		2.00×10^6
Grashof	Gr		8.17×10^{12}
Prandtl	Pr		0.70
Turbulent Prandtl	Pr_t		0.70
Schmidt	Sc		0.85
Turbulent Schmidt	Sc_t		0.85
Free-stream velocity	U_0	$m s^{-1}$	20
Gravity acceleration	g	$m s^{-2}$	9.81
Kinematic viscosity	ν	$m^2 s^{-1}$	1.00×10^{-5}
Thermal conductivity	α	$m^2 s^{-1}$	1.43×10^{-5}
Concentration conductivity	λ	$m^2 s^{-1}$	1.18×10^{-5}
Expansion coefficient	β	K^{-1}	3.33×10^{-3}

Table 3.2: Physical and non-dimensional parameters.

where T is the perturbation temperature and ΔT is the temperature difference between the walls. All non-dimensional parameters characterising the system are listed in Tab. 3.2.

The Reynolds number independence criterion states that flow fields are invariant with Re if above a certain critical number which value is under debate, but with $Re_c = 11.000$ the one commonly adopted [19]. As can be seen in Tab. 3.2, when studying the isothermal case we are well above this critical value, hence we can be sure that the modelling can represent a realistic urban flow. This certainty is not granted when the thermal heating of the canyon is introduced since a convective motion is generated and there is no sufficient knowledge of such phenomena to state that.

3.2 Convergence assessment

Careful attention has been given to assessing stability and the convergence criteria of the simulations performed during the present work. In particular, three main tools implemented in OpenFOAM have been used: **residuals**, **relaxation factors**, **probes**.

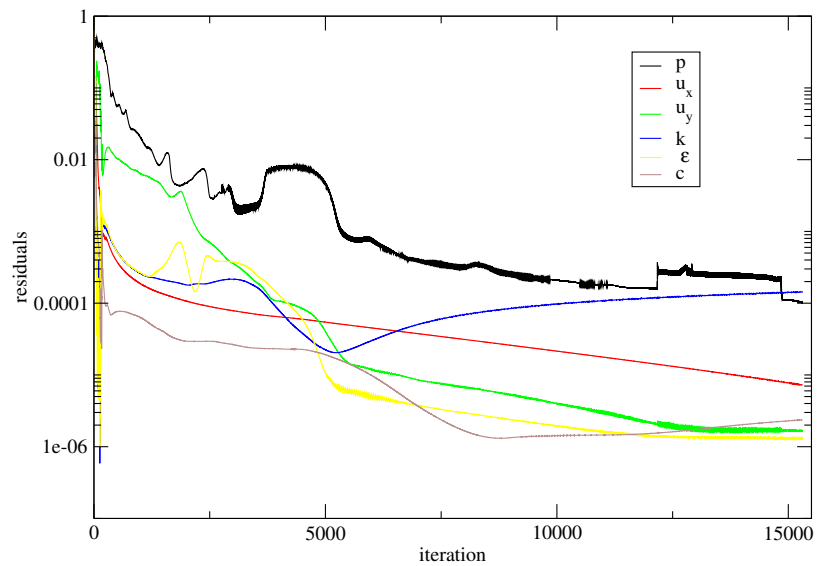
A way to check if a simulation has reached a stable configuration is by checking the **residuals**. It is the most used measure of the convergence of an iterative solution because it directly quantifies the error in the solution of the system of equations. The numerical solution of the equations is calculated by solving the associated linear system $\mathbf{Ax} = \mathbf{b}$ and, for an iterative algorithm, the initial residual is defined as $\mathbf{r} = \mathbf{b} - \mathbf{Ax}$. In this way, \mathbf{r} measures the difference in the value of a variable between two consecutive iterations. Then, the global residual is given by the average of the residuals in each cell:

$$\mathbf{r} = \frac{1}{n} \sum |\mathbf{b} - \mathbf{Ax}|$$

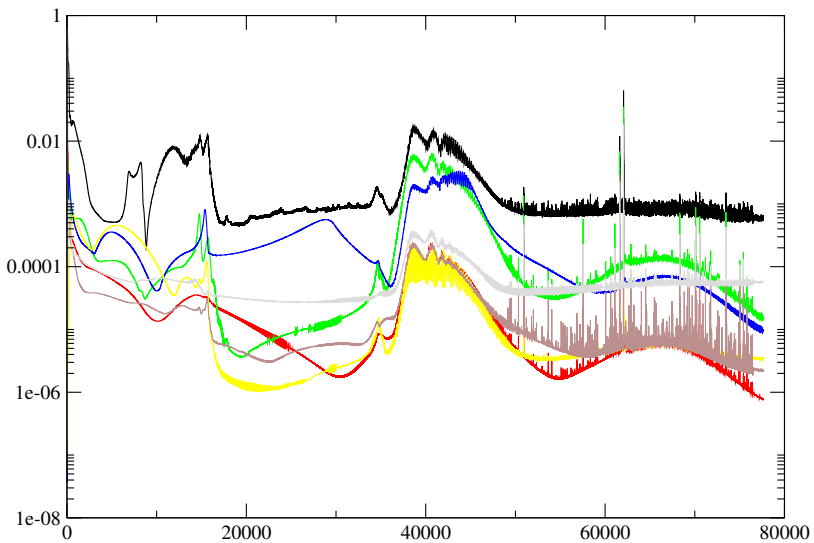
where n is a suitable normalisation factor. The simulation stops when the residual has reached the threshold imposed by the user. Fig. 3.2 shows residuals for the two simulations performed for the validation. It is evident the difference between the two plots. In the first one (Fig. 3.2(a)), representing residuals for the neutral case simulation, such quantities decrease almost linearly, despite some oscillation at the very beginning of the simulation and in the final phase of residuals of the pressure. Overall, since the simulation stopped, we can claim that each quantity has reached the given threshold for the residuals and that the simulation has reached a stable configuration. On the other hand, residuals for the heated case (Fig. 3.2(b)) show very different behaviour. In this case, we see an oscillating behaviour for almost any variables and especially from iteration 50000, with some exceptions starting from about the 20000 to the 30000 iterations. Therefore, we choose to consider reliable solutions the ones given in the almost linear region, where residuals indicate that the solutions between an iteration and the following one are not considerably different from each other, and the mean profiles resulting from the linear region were reasonable ones while after this range of iterations they were not anymore physical.

Together with residual thresholds, the user can also choose *under-relaxation factors*, controlled by the sub-dictionary **relaxationFactors**, a technique used for improving the stability of computation, particularly in solving steady-state problems [31]. The basic idea is to limit the amount by which a variable changes from one iteration to the next. In fact, if the solution widely changes between two consecutive iterations it can cause instability. Defining α as the under-relaxation factor, $\alpha = 0$ means no change in the solution with successive iteration, whereas $\alpha = 1$ guarantees a solution matrix diagonal. In this work, under-relaxation factors have been carefully chosen to ensure the correct stability of the simulations performed.

Finally, **probes** is a useful function for probing data. The basic idea behind the probing process is to provide some point locations and the fields interested in probing, and then the function writes out the values of those fields in the specified points. In particular, **probes** identifies the cells closest to the given points and writes out the values of the fields in those cells. As an example, Fig. 3.3 shows probes for the streamwise velocity in the heated case at a fixed point along the centre of the canyon ($y/H = 0.1, 0.5, 0.9, 1.0, 1.3, 1.6$). We can see how approaching what has been chosen as the end of the simulation, i.e. near the 20000 iteration, the solutions reach a stable value in each probe location.



(a)



(b)

Figure 3.2: Residuals in the (a) neutral case and (b) heated case.

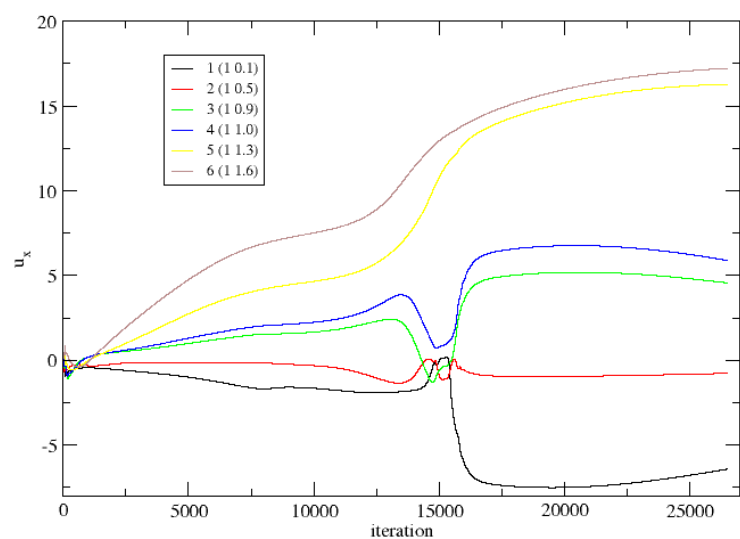


Figure 3.3: Probes of the streamwise velocity in the heated case.

3.3 Validation

In this section the accuracy of the simulation method will be assessed, both for the neutral case, i.e. in absence of thermal stratification and temperature gradients, and the case in which the upwind facade is heated, also in this case without stratification. Vertical profiles of the velocities are obtained using the `singleGraph` utility along three vertical lines within the canyon near the upwind building ($x/H = 0.75$), the centre of the canyon ($x/H = 1.00$) and the downwind building ($x/H = 1.25$).

3.3.1 Neutral case

Simulation of the neutral case has been compared with four experimental datasets and two numerical simulations for the velocity components. The four datasets include: Brown et al. [20], Chew et al. [19], Li et al. [18], Michioka et al. [21]. The two numerical simulations used are from Michioka et al. [21] and Cintolesi et al. [26]. Regarding the concentration profiles, the validation is made against the LES of Michioka et al. [21], measurements of Meroney et al. [23], Pavagenau and Schatzmann [22] and the LES simulation by Cintolesi et al. [26].

The vertical profiles of the non-dimensional streamwise velocity component are shown in Fig. 3.4. Overall, the three plots show a good agreement between the RANS simulation and the reference data. Fig. 3.5 shows the vertical component of the velocity field. In this case, reference data and the simulation in the centralline of the canyon exhibit different behaviour. Chew et al. [19] and Li et al. [18] measure a positive vertical velocity with the maximum halfway up the canyon, while the RANS simulation shows the same behaviour of Brown et al [20] and the LES simulation performed by Cintolesi et al. [26], i.e. an almost zero vertical velocity. As concerns the profiles near the upwind and the downwind buildings, the RANS simulation shows a good agreement in both cases.

General considerations about the mechanisms involved in a typical urban street canyon under neutral stratification conditions can be done by looking at the velocity streamlines pattern and the concentration distribution shown in Fig. 3.6. A clockwise vortex develops in the centre of the street canyon, with a skimming flow above and, in between the two, at $z/H = 1$, a shear layer. The pollutant is being transported toward the upwind facade by the primary vortex (Fig. 3.6b), where the majority of the pollutant is found. Of the three secondary counterclockwise vortices only the one in the bottom-left corner of the canyon is visible. The interface between the canyon and the ambient region ($z/H = 1$) is almost a flat line coinciding with the roof level. Following Li et al. [32] the flow characterising the urban canopy layer can be divided into three parts: an external flow outside the canyon, a cavity shear layer at the roof level, and a cavity flow inside the canyon.

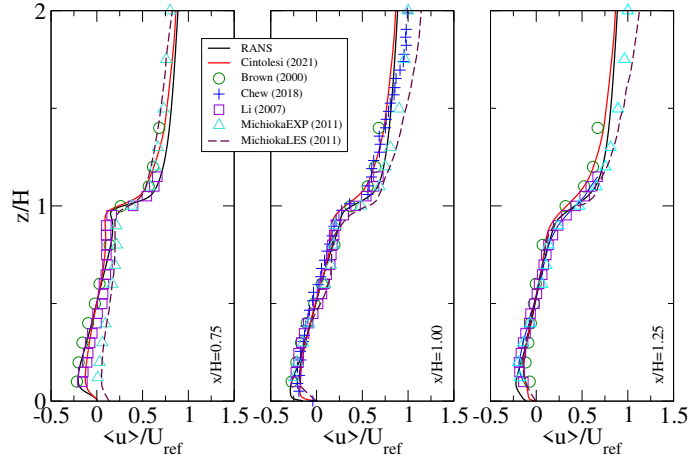


Figure 3.4: Non-dimensional streamwise velocity component along three vertical lines: $x/H = 0.75, 1.00, 1.25$. The RANS simulations is displayed by a black solid line. Symbols represent: red solid line, Cintolesi et al. [26]; green \circ , Brown et al. [20]; purple \square , Li et al. [18]; blue + Chew et al. [19]; cyan Δ , Michioka et al. (EXP) [21]; maroon dashed lines, Michioka et al. (LES) [21].

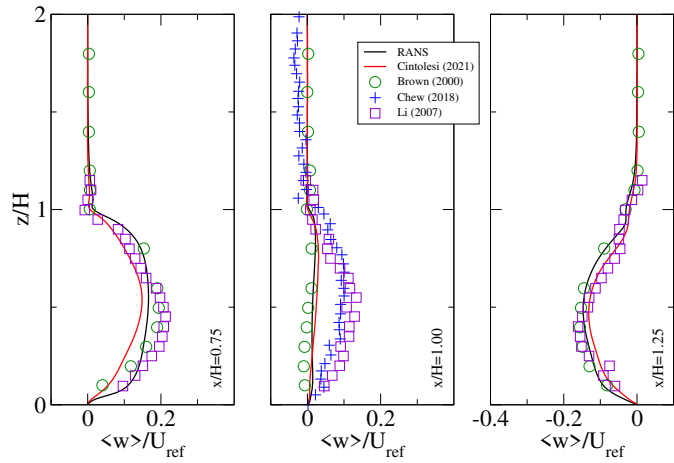
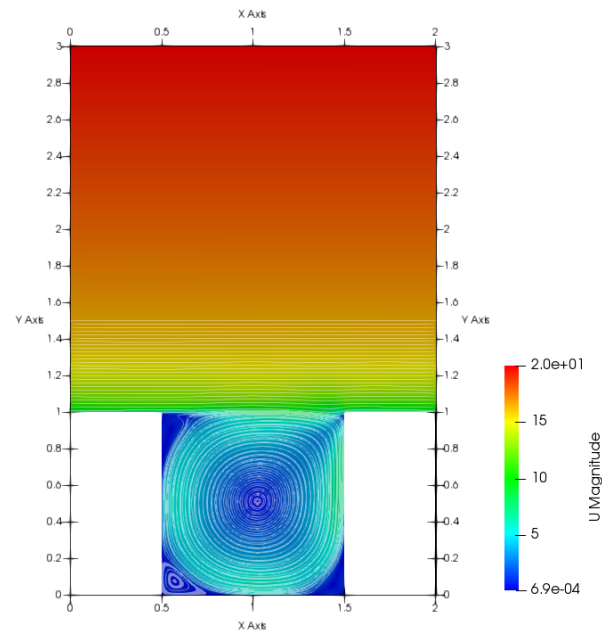
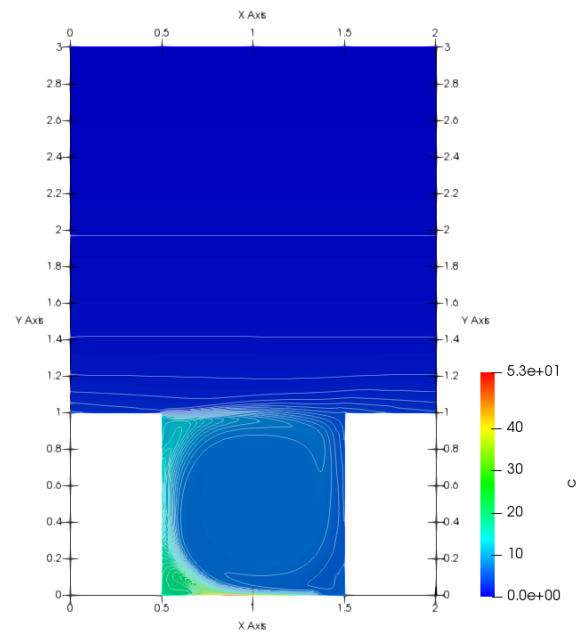


Figure 3.5: Non-dimensional vertical velocity component along three vertical lines: $x/H = 0.75, 1.00, 1.25$. The RANS simulations is displayed by a black solid line. Symbols represent: red solid line, Cintolesi et al. [26]; green \circ , Brown et al. [20]; purple \square , Li et al. [18]; blue + Chew et al. [19].



(a)



(b)

Figure 3.6: (a) Flow field streamlines and (b) concentration distribution in the neutral case.

The vertical profile of the non-dimensional concentration C^* are shown in Fig. 3.7. Near the upwind facade, the RANS profile underestimates pollutant concentration measured by the experimental reference data, while it better reproduces profiles of experimental data in the centre and downwind regions, slightly overestimating the latter compared to experimental data close to the roof level. Near the upwind facade and in the centre of the canyon, the RANS overestimates the LES profile expected by Cintolesi et al. [26], while it almost collapses on it at $x/H = 1.25$. At the top region outside the canyon, i.e. at $z/H = 1.00$, the pollutant is dispersed in the free atmosphere hence the concentration rapidly goes to zero. This can be obtained by numerically imposing a zero boundary condition at the top. The slight peak at the roof level after which concentration rapidly goes to zero shows how almost all of the pollutant is concentrated inside the canyon. Eq. 2.2d express the two pollutant dispersion processes: advection, due to the mean wind fields, and diffusion, given by the turbulent mixing. Being all three profiles nearly constant in the inside region demonstrates that in neutral conditions turbulent motions represent the only removal mechanism of a pollutant.

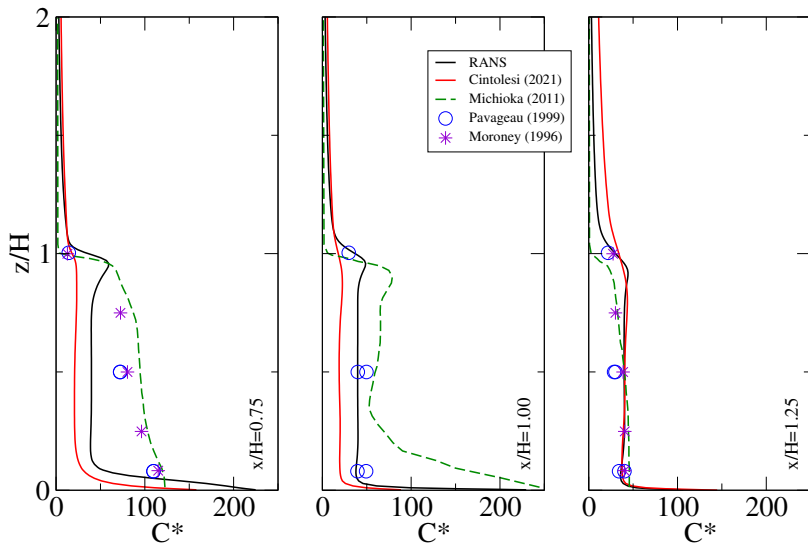


Figure 3.7: Non-dimensional pollutant concentration along three vertical lines: $x/H = 0.75, 1.00, 1.25$. The RANS simulations is displayed by a black solid line. Symbols represent: red solid line, Cintolesi et al. [26]; cyan Δ , Michioka et al. (EXP) [21]; blue \circ Pavagenau et al. [22]; purple $*$, Meroney et al. [23].

In Fig. 3.8 are shown the vertical profiles of the turbulent kinetic energy (TKE), previously made non dimensional by means of the reference velocity U_{ref} . Plots show a

good agreement between the simulation and the data in the internal region of the canyon. It can be noticed that among the reference data, only the LES by Cintolesi et al. [26] and data from Li et al. [18] are capable of reproducing the TKE peak at the roof level ($z/H = 1$). Also, the present RANS is able to capture this feature, slightly overestimating it, though. This is a well-known characteristic of $k - \varepsilon$ turbulence models. This peak of the TKE is a highly important feature in urban canyon studies because it suggests that turbulent mixing is responsible for the removal of the pollutant from the internal region of the canyon. Furthermore, it is also well-documented how the distributions of the TKE differs for different PBL conditions. An example is given in [33]. The increasing instability conditions of the PBL results in an increase in the TKE field within the street canyon, with consequences of the turbulent diffusion processes of pollutants. In unstable atmospheric conditions, the turbulent diffusion processes are stronger, and the mixing of pollutants, and consequently its removal, is enhanced. Outside the canyon, RANS simulation completely differs from the reference profiles. This feature requires additional investigations to be fully understood and it is probably imputable to the turbulence model used.

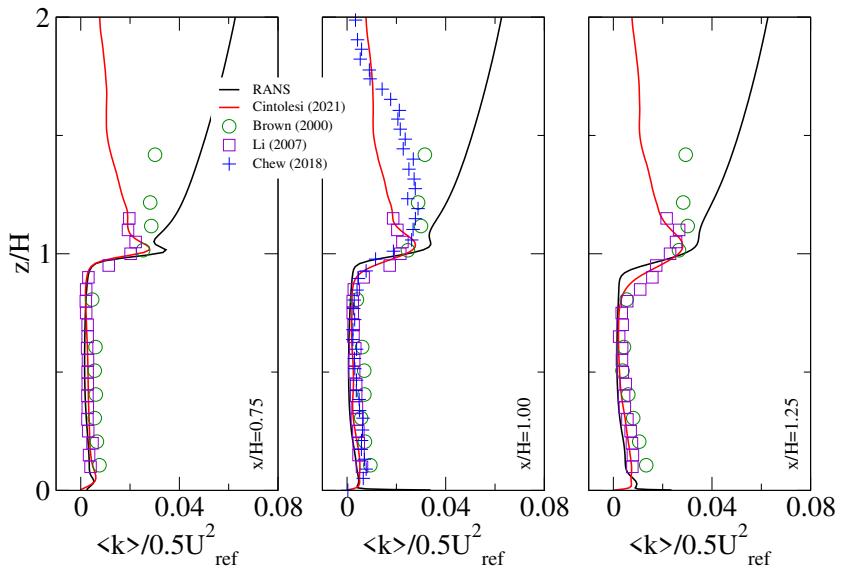


Figure 3.8: Non-dimensional turbulent kinetic energy along three vertical lines: $x/H = 0.75, 1.00, 1.25$. The RANS simulations are displayed by a black solid line. Symbols represent: red solid line, Cintolesi et al. [26]; green \circ , Brown et al. [20]; purple \square , Li et al. [18]; blue + Chew et al. [19].

3.3.2 Heated case

Starting from the neutral case, the upwind facade is now heated bringing it to a higher temperature compared to the other solid walls and chosen in a way that the resulting Richardson number is equal to $Ri = 2.05$, which corresponds to a significant convective motion within the canyon. This is done by imposing the same temperature on all the solid walls except the upwind facade, where the temperature difference chosen is fixed. The validation is carried out by comparing results from the RANS simulation with the same configuration investigated by Cintolesi et al. [26]. With the addition of a thermal force, a convective motion is generated which is superimposed on the inertially-driven motion discussed in the neutral case.

Fig. 3.9 shows vertical profiles of the non-dimensional streamwise component of the velocity along the three vertical lines, as before. RANS simulation almost perfectly reproduces the LES profiles, with a small overestimation up to $z/H = 0.5$ and an underestimation above. The major differences are noticeably approaching the roof level and outside the canyon, where the RANS undervalues the magnitude of the streamwise velocity in all the three regions.

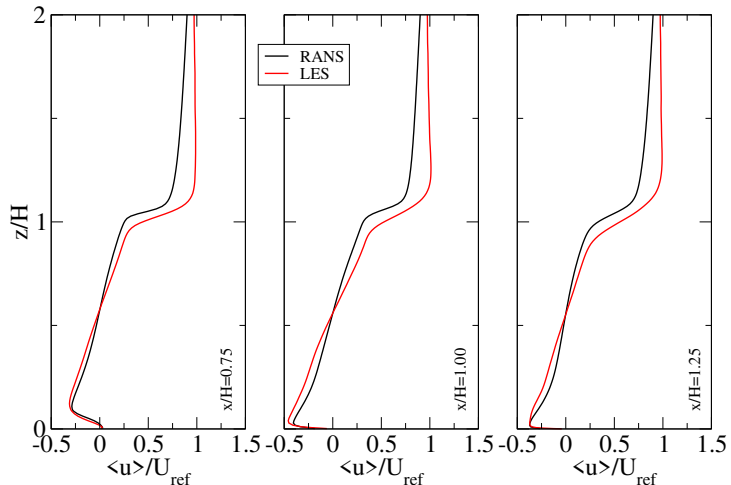


Figure 3.9: Non-dimensional streamwise velocity component along three vertical lines: $x/H = 0.75, 1.00, 1.25$. The RANS simulation is displayed by a black solid line, LES simulation by Cintolesi et al. [26] in red solid line.

Major differences can be seen in the vertical profiles of the non-dimensional vertical velocities, shown in Fig. 3.10. The RANS simulation profile almost collapses on the LES profile in the central part of the canyon, while it is not greatly capable to appreciate

variations of the vertical velocity near the upwind and downwind facades, with the RANS simulation underestimating the peak of the vertical velocity compared to the one obtained by the LES, and resulting in weaker vertical velocities near the two building facades.

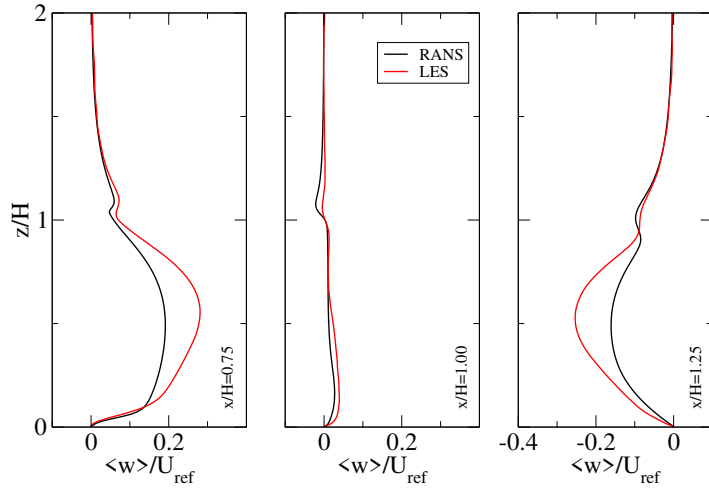
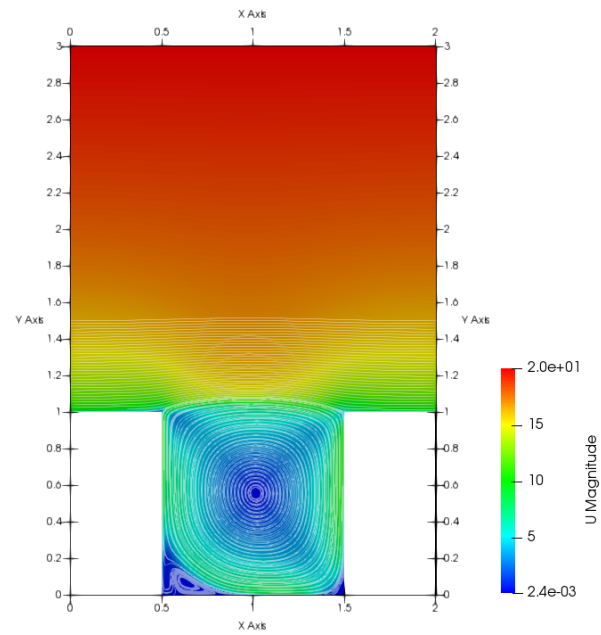
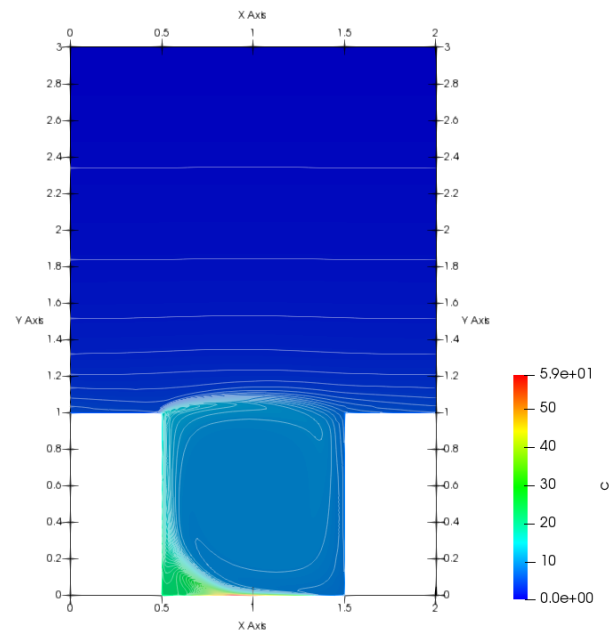


Figure 3.10: Non-dimensional vertical velocity component along three vertical lines: $x/H = 0.75, 1.00, 1.25$. The RANS simulation is displayed by a black solid line, LES simulation by Cintolesi et al. [26] in red solid line.

As in the neutral case, looking at the streamline of the velocity field we can make considerations about the overall motion within the canyon. These are shown in Fig. 3.11a. It can be seen the superimposed motion destroys the minor vortexes present in the up-left and the bottom-right corners and which raises the interface reaching its maximum at $x/H = 1.0$. As a result of the superimposed thermal convection, the primary vortex velocities are increased both near the downwind facade and in the centre of the street canyon. As concerns the concentration distribution (Fig. 3.11b), the pollutant is transported toward the upwind building as in the neutral case but, following the upward displacement of the shear layer, also the concentration distribution shows such a feature.



(a)



(b)

Figure 3.11: (a) Flow field streamlines and (b) concentration distribution in the heated upwind facade case.

Vertical profiles of the non-dimensional concentration in the case of the upwind facade heated up are shown in Fig. 3.12. It is easily noticeable the overestimation resulting from the RANS simulation. Moreover, it still reproduces the peak at $z/H = 1$ seen in the neutral case, no anymore visible in the LES simulation, suggesting the idea that the RANS simulation, contrary to the LES, predicts a primary vortex which is similar in strength to the one resulting in isothermal conditions, hence still capable of transporting pollutant toward the downwind building.

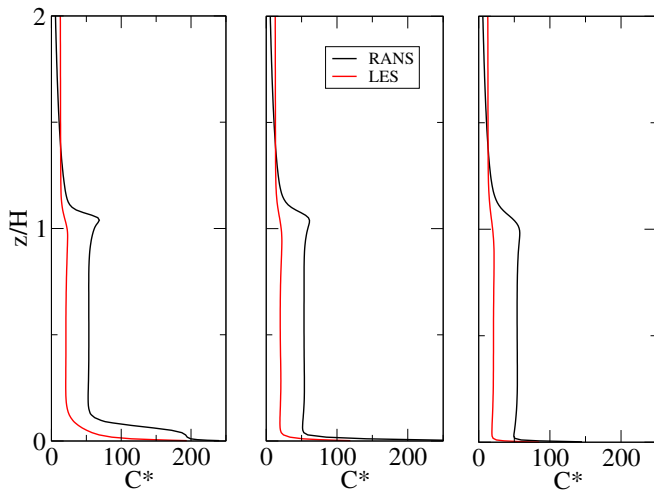
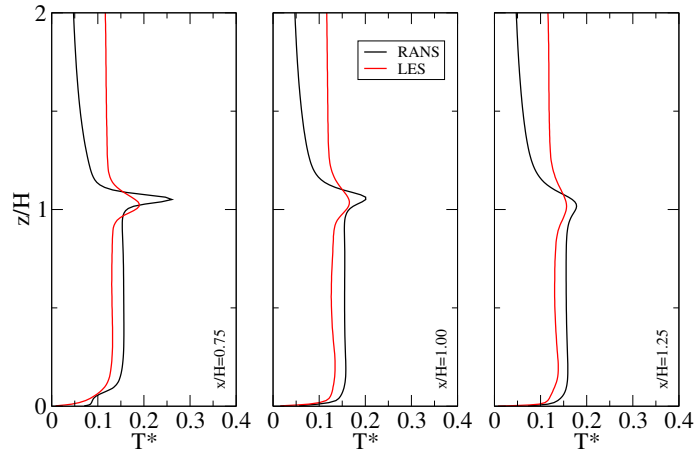


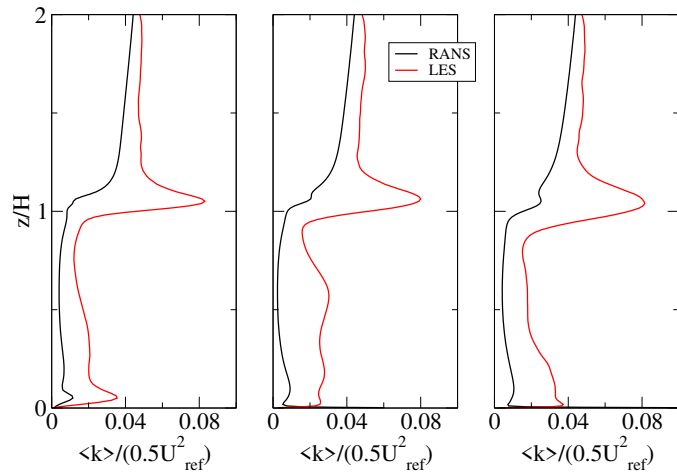
Figure 3.12: Non-dimensional concentration along three vertical lines: $x/H = 0.75, 1.00, 1.25$. The RANS simulation is displayed by a black solid line, LES simulation by Cintolesi et al. [26] in red solid lines.

Fig. 3.13a shows vertical profiles of temperature perturbation, previously made non-dimensional using Eq. 3.5. From those three profiles we can say that with respect to the LES simulation, the RANS simulation firstly overestimates the temperature inside the canyon, then presents a more enhanced peak at the roof level $z/H = 1$, and finally shows a sharper decrease outside the canyon. Furthermore, it can be noticed how for $z/H > 1$ the LES simulation expects, after a short peak, the same temperatures found inside the canyon, while the RANS temperatures are more than a half smaller compared to that in the inside region. Moreover, thermal convection is a difficult phenomenon to reproduce even for more advanced numerical techniques, hence we do not expect accurate results in the reproduction of this mechanism.

Regarding the second-order statistics, vertical profiles of the non-dimensional turbulent kinetic energy k are shown in Fig. 3.13b. A clear underestimation of this quantity can be seen for each plot. The profile shown in the neutral case is almost not anymore



(a)



(b)

Figure 3.13: Non-dimensional (a) temperature perturbation and (b) concentration along three vertical line: $x/H = 0.75, 1.00, 1.25$. The RANS simulation is displayed by a black solid lines, LES simulation by Cintolesi et al. [26] in red solid lines.

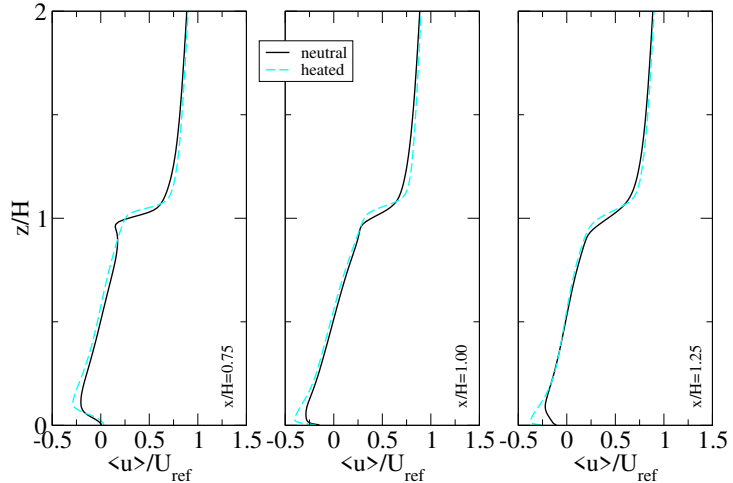
visible for the present RANS, while the profile of the LES in the heated case still reminds the one obtained in the neutral case.

3.3.3 Comparison between the neutral and heated cases

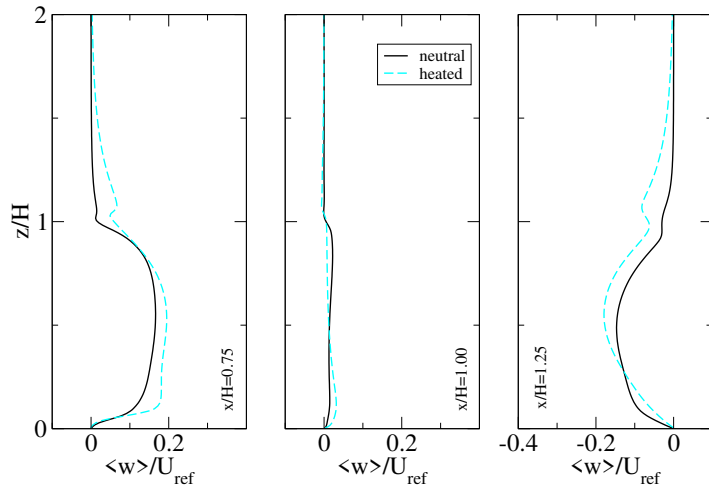
We now compare the results given by the RANS simulations in the two cases previously discussed.

As we previously mentioned, the addition of a buoyancy force, which is a force directed upward, results in a convective motion superimposed on the motion present in the neutral case. The characteristics of this motion can also be analysed by looking at the vertical profiles of the streamwise and vertical velocity components displayed in Fig. 3.14. Focusing on the streamwise component in Fig. 3.14(a), we can see that the major displacement between the two profiles can be appreciated only at the street and roof levels, with an almost perfect overlapping in the other regions, both inside and outside the canyon. Moving now the attention to the vertical velocity in Fig. 3.14(b), the thermal effects can be better appreciated. These plots show an increase in the vertical velocity near the upwind building and a decrease of that component nearby the downwind building, both extending also in the interface between the canyon and the external region. This suggests the idea that the thermal forcing acts by strengthening both the downwind and the upwind sides of the inertially-driven vortex generated in isothermal conditions.

We can see the effects of this overall motion on the dimensionless concentration profiles shown in Fig. 3.15. The present RANS expects an increase of the concentration of pollutants in both the three regions, i.e. near both the upwind and downwind building, and in the centre of the canyon, whereas Cintolesi et al.[26] found a decrease of such quantity. This means that the RANS model predicts an overall motion that does not enhance the dispersion of pollutants but, on the contrary, decreases it.



(a) Streamwise velocities



(b) Vertical velocities

Figure 3.14: Comparison of the nondimensional velocity components in the two cases along three vertical line: $x/H = 0.75, 1.00, 1.25$. Black solid line is for the neutral case, dashed cyan line for the heated case.

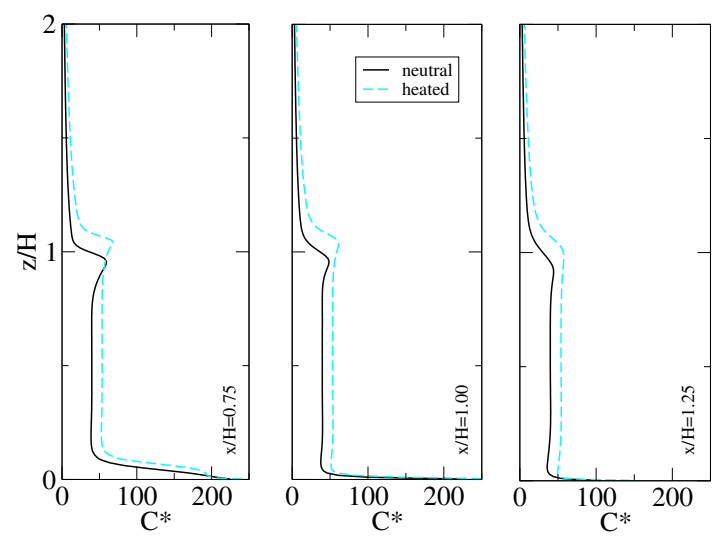


Figure 3.15: Comparison of the nondimensional concentration in the two cases along three vertical line: $x/H = 0.75, 1.00, 1.25$. Black solid line is for the neutral case, dashed cyan line for the heated case.

3.4 Final remarks

Validation of the neutral case, i.e. every solid wall at the same ambient temperature, and the case in which the upwind facade is heated have been conducted in terms of first- and second-order statistics through non-dimensional quantities and comparing simulation profiles with experimental data and LES simulations present in literature. In the first case, the validation suggests a satisfactory accuracy of RANS simulation in reproducing vertical profiles of mean flows and turbulent quantity. In the second case, the heated one, this accuracy can be found only for the mean flows, given the great discrepancies found for the turbulent kinetic energy between the RANS and LES simulations. In light of the validation results and acknowledging the limitations found, the setup of the simulation can be recognised as sufficiently adequate to conduct the studies on the different heating configurations, but only first-order statistics will be analysed, confident of the results obtained.

Results

In this chapter will be shown the results of the RANS simulations obtained by imposing a temperature difference between the solid boundaries and the air. In particular, three configurations will be explored:

- upwind building heated;
- downwind building heated;
- both buildings and street heated.

Those three configurations aim to mimic the scenarios with the sun at the right, at the left, and the direct sunshine, respectively, as displayed in Fig. 4.1.

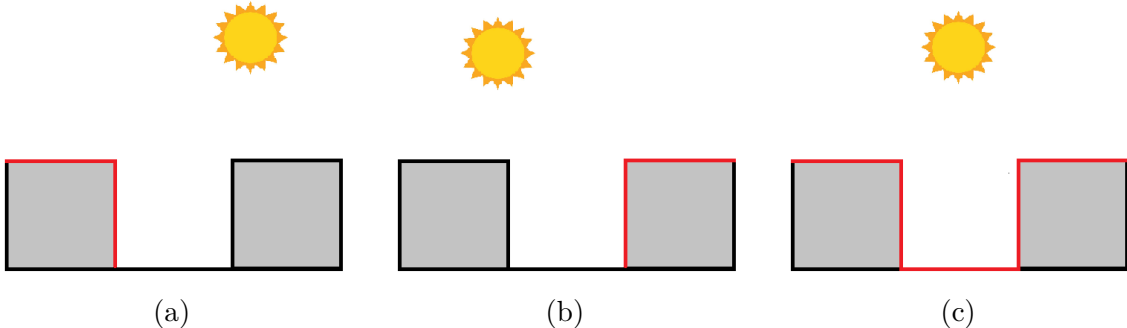


Figure 4.1: The three configurations explored: (a) upwind facade heated, (b) downwind facade heated and (c) all facades heated.

Three temperature differences are imposed on the boundaries given by three values of the Richardson number defined in Eq. 3.3, $Ri = 0.5, 1.0, 1.5$. The aim here is to conduct a parametric study based on nondimensional numbers by reproducing several configurations and setups describing different motion regimes, and then evaluate how each configuration affects the distribution of physical variables inside the canyon. As discussed in sec. 3.1.4, the Richardson number is useful to describe the nature of the

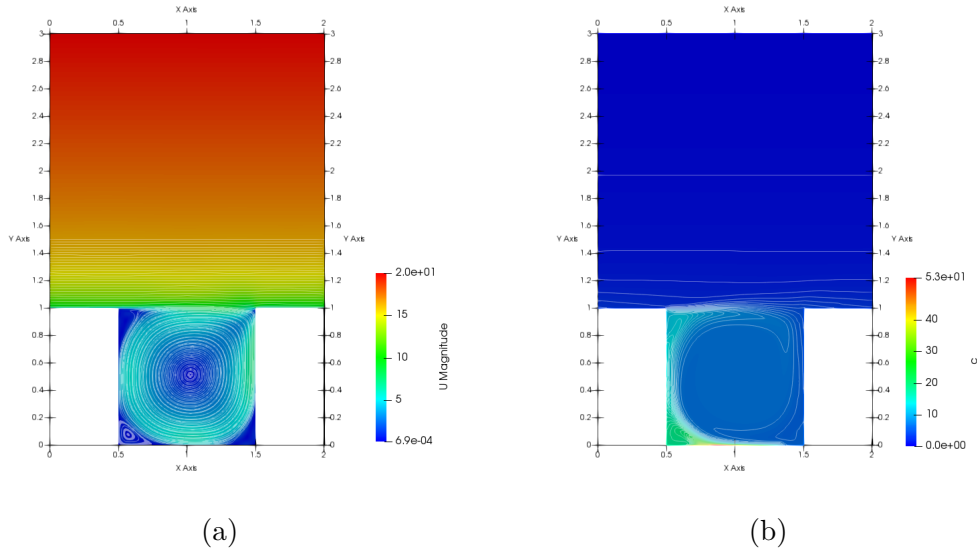


Figure 4.2: (a) Flow field streamlines and (b) contour of the concentration for the neutral case.

flow within the canyon. In this way, $Ri = 0.5$ represents a motion driven by the inertial forces, $Ri = 1.0$ a motion generated by the balance of the inertial forces and the buoyancy, and $Ri = 1.5$ a convective motion.

The results of the RANS simulations are organised in three sections depending on the temperature difference imposed. In each section, the three configurations studied are then described.

As described in sec. 3.3.1, when each solid boundary, both horizontal and vertical, is at the same temperature and an ambient wind U_{ref} flows from the left-hand side to the right-hand side, the motion generated in the street canyon by the ambient wind displays in the form of a primary clockwise vortex with three recirculating regions at the top-left, bottom-left and bottom-right corners of the canyon, as shown in Fig. 4.2(a). The interface between the canyon and the outside region is a sharp horizontal shear layer which serves as a solid boundary and acts like a barrier between the two dynamics, the one internal to the canyon and the external one. As a consequence of both the ascendant flow near the upwind facade and the bottom-right recirculating region, the higher concentration of pollutants is found at the upwind side of the urban canyon (Fig. 4.2(b)).

4.1 Weak convective motions ($Ri = 0.5$)

4.1.1 Upwind building heated

When the upwind facade is heated the resulting internal circulation is the one depicted in Fig. 4.3a. Overall, the main clockwise vortex generated by the ambient wind in isothermal conditions is preserved, but the two recirculating regions at the top-left and bottom-right corners vanish with the one in the bottom-left corner the only one to endure, and a slightly perceptible upward bending of the interface can be noticed. To better understand the characteristics of this motion compared to the one arising in neutral conditions, we look at the dimensionless vertical profiles of the streamwise and vertical velocity components, shown in green dashed lines in Fig. 4.4(a) and Fig. 4.4(b), together with the neutral vertical profile in black solid line. The streamwise component is almost the same of that in the neutral case, with major differences detectable at the rooftop level $z/H = 1$ near the upwind facade, where the top left recirculating region vanishes, and at the street level up to $z/H = 0.1$ near the downwind facade, corresponding to the shrinking of the bottom right counter-clockwise vortex. The vertical velocity is the one more influenced by the addition of the buoyancy term; Fig. 4.4(b) shows that vertical velocity near the upwind building slightly increases at $z/H = 0.2$, then it almost collapses on the neutral profile, and finally decreases from $z/H > 0.55$ toward the roof level. At $z/H = 1$ this component is slightly higher than in the neutral case. Moving on to the central region of the canyon, at $x/H = 1.00$, the vertical profile is practically constant, and the vertical velocity does not show a significant change in this region. The vertical velocity profile near the downwind facade shows the same behaviour as the upwind region, i.e. an increase moving halfway up the canyon and then a decrease which, contrary to the downwind side, continues outside the canyon too. Hence, the thermally-driven motion is a clockwise circulation that superimposes on the inertially-driven one, shrinking the recirculating region at the bottom-right corner and dissolving the one at the top-left corner. This circulation shows a similar strength to the one in isothermal conditions. The non-dimensional velocity vertical profiles show that at the bottom of the canyon is formed what Cintolesi et al.[26] named zero-velocity region.

Fig. 4.3(b) shows the distributions of the temperature perturbation in terms of the buoyancy. When the upwind facade is heated, the clockwise vortex transports the temperature from the upwind building to the interface region, and then downward at the side of the downwind facade. As also demonstrated by the peaks at the roof level in Fig. 4.4(c), the maximum temperature differences are detectable at the interface where it is transported by the horizontal branch of the vortex, and right above the street level. The interior of the canyon does not show any vertical stratification, with the vertical profile being constant from above the street level.

Regarding the concentration, the dispersion patterns generated by this configuration

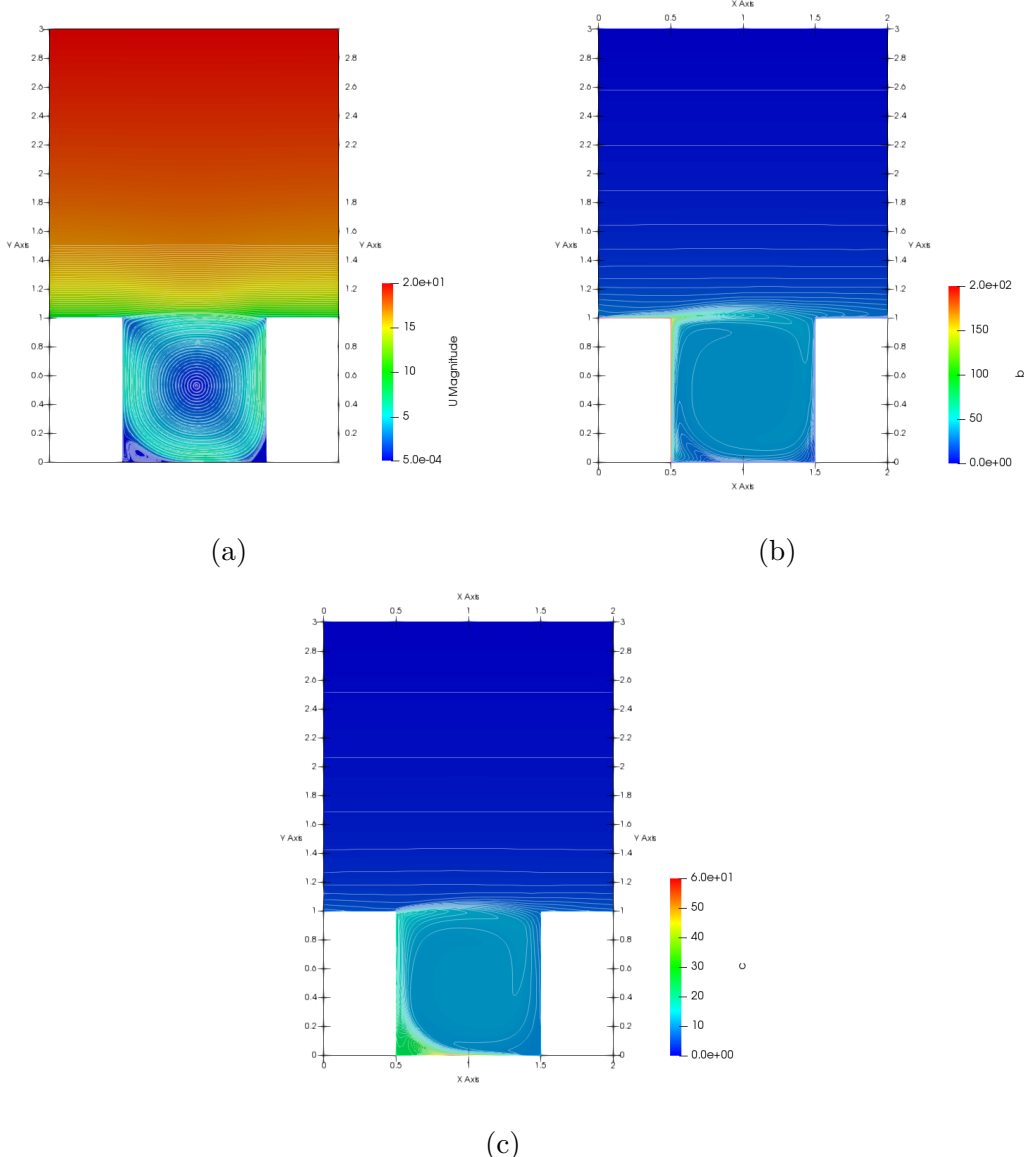


Figure 4.3: (a) Flow field streamlines, (b) contour of the buoyancy, (c) contour of the concentration for the upwind heated case when $Ri = 0.5$.

is shown in Fig. 4.3(c). The convective motion generated by the heating of the upwind facade is not sufficient to reinforce the pollutant removal from the canyon, and a high concentration can be found at the street level near the upwind building, and at the roof level where it is transported by the horizontal branch of the circulating motion. From the vertical profiles of the non-dimensional concentration (Fig. 4.4(d)) the concentration inside the canyon is higher compared to the neutral case, with two peaks, one at $z/H <$

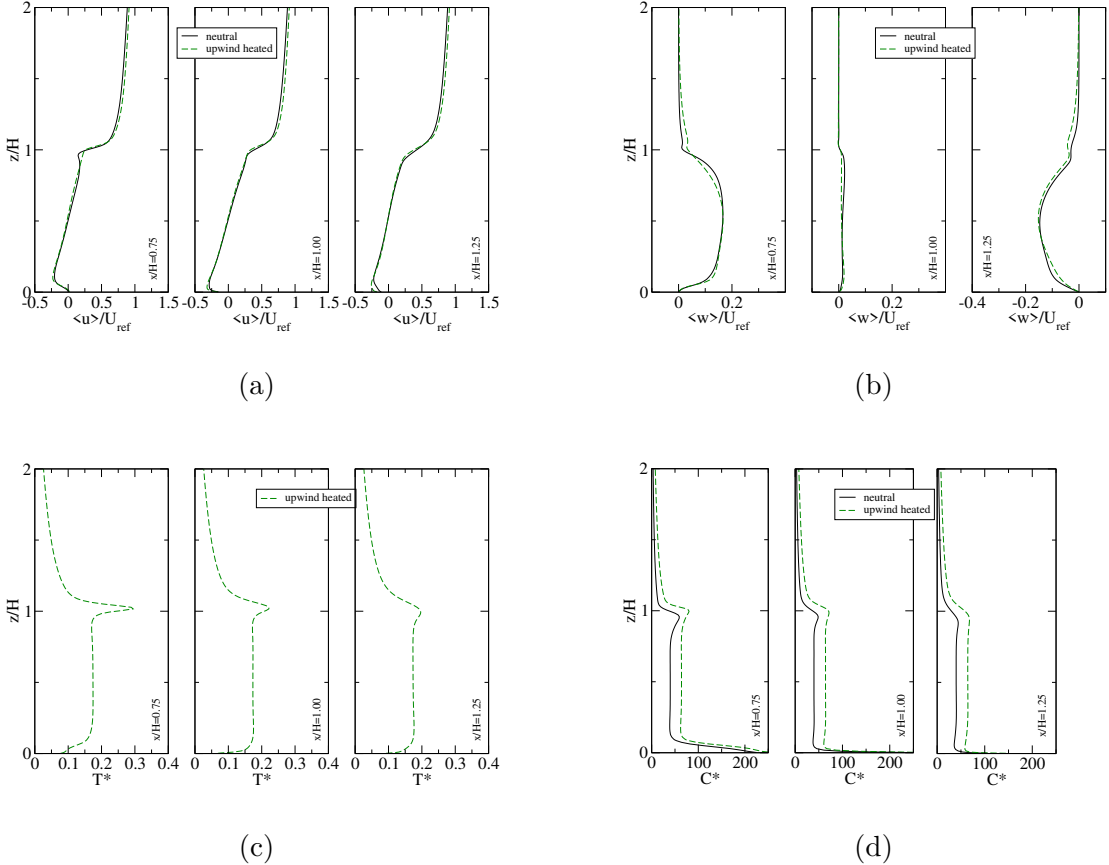


Figure 4.4: Dimensionless vertical profiles of the (a) streamwise velocity and (b) vertical velocity, (c) temperature perturbation, (d) concentration, when the upwind building is heated and $Ri = 0.5$: black solid line represents the neutral case, green dashed line the upwind heating case.

0.2 and the other at $z/H = 1.0$, with the latter moved upward because of the upward displacement of the interface. Same behaviour can be seen in the other two profiles, with all of three showing a constant concentration inside the canyon.

4.1.2 Downwind building heated

Heating the downwind facade and its roof generates the flow field depicted in Fig. 4.5(a). In this case, the primary vortex visible in the neutral case is shrunk in the upper region of the canyon, above $z/H = 0.5$, by the enlargement and the merging of the bottom recirculating regions, generating a circulation composed of two vortices, one above the other, and a perfectly flat interface. Moreover, the enlargement of the bottom-left recirculating region moves the centre of the primary vortex towards the downwind building. Looking at the vertical profiles of the non-dimensional velocity components in Fig. 4.6(a) and (b) it can be noticed that in all three regions, the streamwise velocity increases in the bottom half of the canyon ($z/H < 0.50$), while decreasing in the upper half and the outside region ($z/H > 0.50$). For $z/H < 0.75$ the vertical velocity is given by the weak vertical velocity of the one big recirculating region and for $z/H > 0.75$ by what remains of the primary vortex. Hence, at the side of the two facades, the convection meets the opposite flow generated by the ambient wind. As in the previous case, a zero-velocity region is detectable at the street level, especially near the downwind facade.

In this case, a vertical stratification within the canyon is generated, as can be seen in Fig. 4.5(b). Given the circulating motion previously illustrated, it can be understood that at the interface between the main vortex and the counter-rotating one, the warm air is moved from the downwind facade toward the centre and then in opposite vertical directions near the upwind region. Vertical profiles of the non-dimensional temperature perturbation (Fig. 4.6)(c) show that this stratification slightly weakens moving away from the heated facade towards the upwind building.

Heating the downwind facades results in the distribution of the concentration shown in Fig. 4.5(c). It can be seen that, due to the counterclockwise motion of the vortex in the lower part of the canyon, the pollutant is no anymore dispersed in the canyon but it accumulates near the heated facade. Hence, from vertical profiles in Fig. 4.6(c), the maximum concentration is found at the street level where the pollutant source is located, particularly at $x/H = 1.25$, and the peak at the roof level flattens. All that given, near the upwind building the overall concentration within the canyon is lower because it gets accumulated at $z/H < 0.25$ near the downwind building (Fig. 4.5(c)).

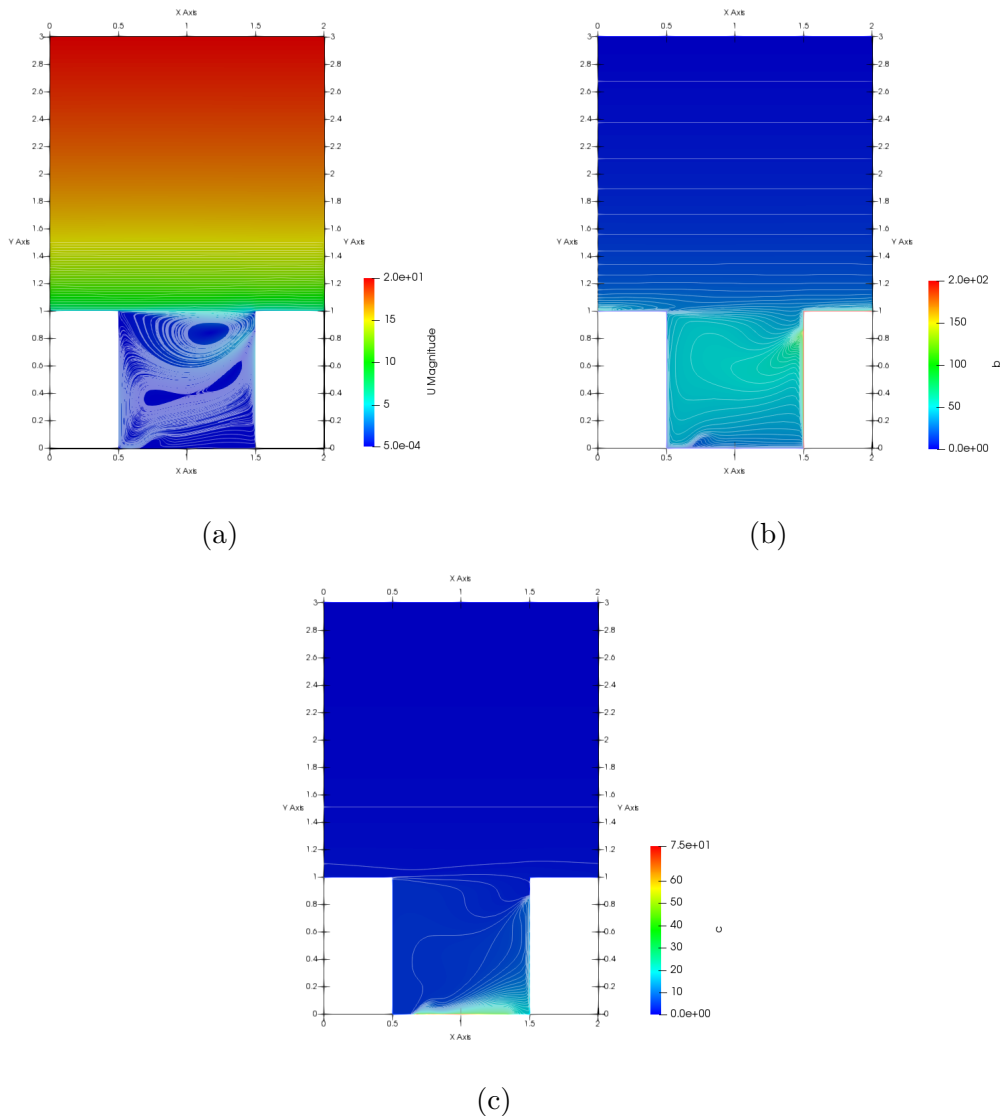


Figure 4.5: (a) Flow field streamlines, (b) contour of the buoyancy, (c) contour of the concentration for the downwind heated case when $Ri = 0.5$.

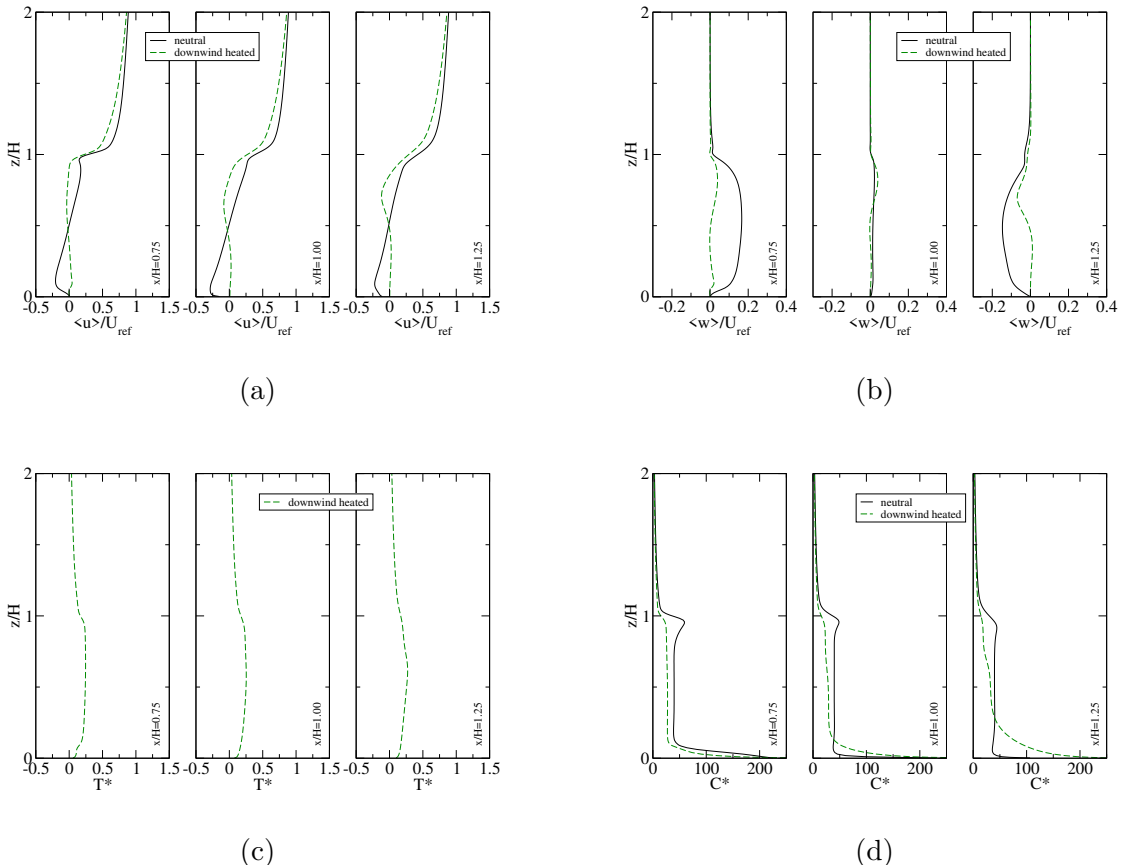


Figure 4.6: Dimensionless vertical profiles of the (a) streamwise velocity and (b) vertical velocity, (c) temperature perturbation, (d) concentration, when the downwind building is heated and $Ri = 0.5$: black solid line represents the neutral case, green dashed line the upwind heating case.

4.1.3 Ground and both buildings heated

When all the surfaces are heated up, the convective motion almost restores the circulation under neutral conditions, but enlarges the minor vortex at the bottom-right of the canyon, removing the two recirculating regions in the left-side corners, and lifting upward the interface (Fig. 4.7(a)). The non-dimensional vertical profiles of the streamwise velocity (Fig. 4.8(a)) almost collapses on the neutral profiles inside the canyon, with the two exceptions of the roof level $z/H = 1$ near the upwind facade where the minor vortex no longer exists, and near the upwind facade where the bottom peak moves upward to $z/H = 0.25$, showing that the centre of the recirculating region in this location has moved upward. As can be seen in Fig. 4.8(b), the downward motion near the downwind building decreases because of the reinforcement of the recirculating region generated by the additional buoyancy force, showing a peak at $z/H = 0.25$ corresponding to a strong downward velocity of that vortex.

The heating of all the boundaries of the canyon generates the temperature perturbation distribution of Fig. 4.7(b). As in the neutral case, the warm air is transported from the principal vortex towards the interface, then downward beside the downwind facade, and here both the primary vortex and the recirculating region move the air downward toward the street, where it encounters the horizontal bottom branch of the principal vortex which pushes the air again at the upwind building. Being a circular motion present, stratification is absent. From non-dimensional vertical profiles of the temperature perturbation (Fig. 4.8(c)), it can be seen that within the canyon the temperature is practically constant, with two exceptions, at the street level $z/H < 0.25$ near the downwind building where the enforced recirculating vortex is located and transports the warm air upward, and at the roof level at $x/H = 0.75$ and $x/H = 1.00$ where it is transported by the interface.

Lastly, the two-vortices circulation generated by the heating of all the surfaces (Fig. 4.7(a)) moves the pollutant all over the canyon following its motion, with the tracer being accumulated in the bottom-right corner by the enforced recirculating region which rotates counter-clockwise. This results in what can be seen by the vertical profiles in Fig. 4.8(d), where the concentration within the canyon is higher compared to the isothermal case because of the absence of an effective transport mechanism, and a peak at $z/H = 0.2$ near the downwind building given by the transport of the enforced recirculating region.

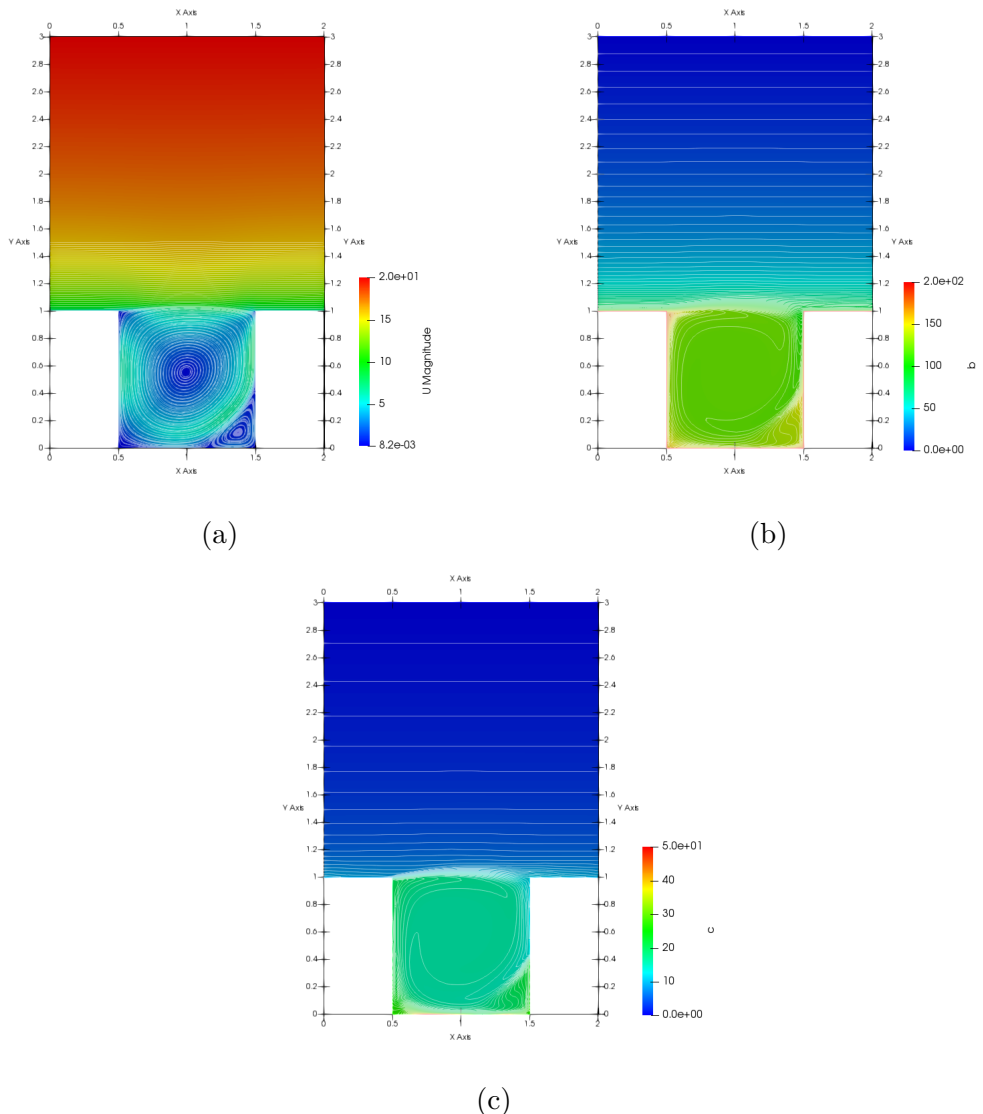


Figure 4.7: (a) Flow field streamlines, (b) contour of the buoyancy, (c) contour of the concentration for the all surfaces heated case when $Ri = 0.5$.

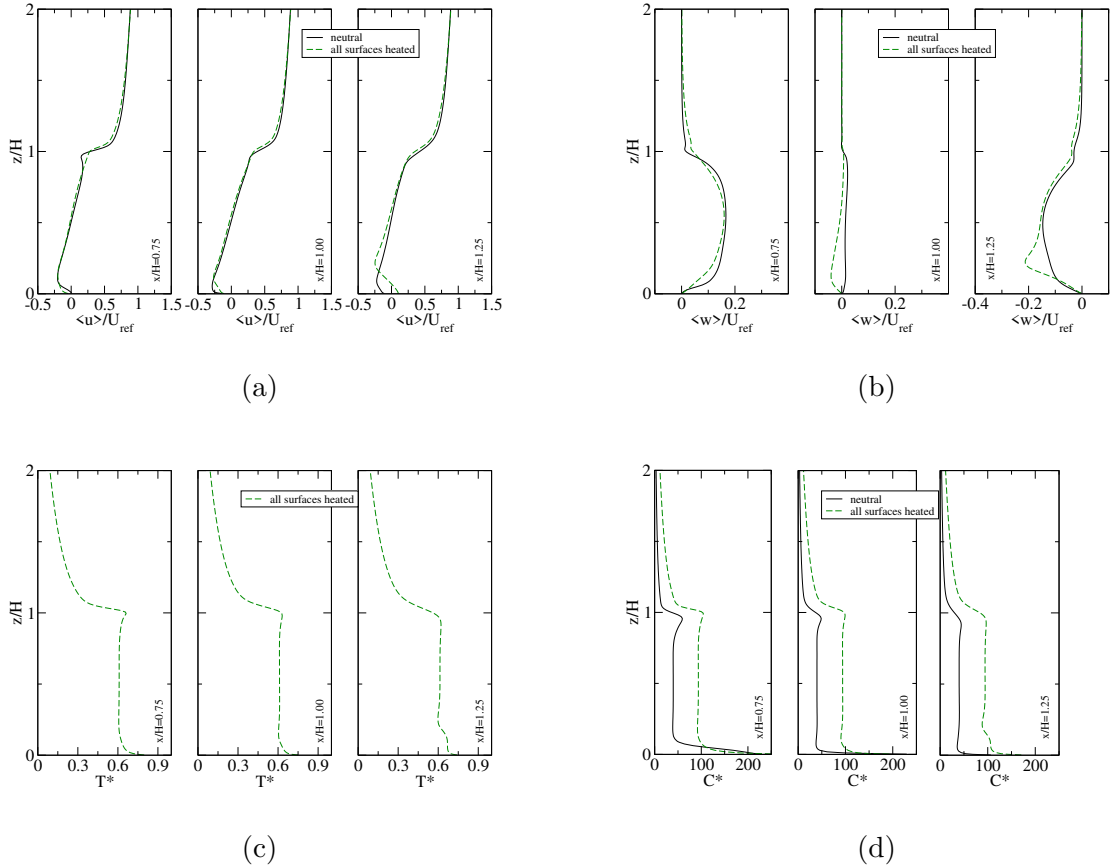


Figure 4.8: Dimensionless vertical profiles of the (a) streamwise velocity and (b) vertical velocity, (c) temperature perturbation, (d) concentration, when all surfaces are heated and $Ri = 0.5$: black solid line represents the neutral case, green dashed line the upwind heating case.

4.2 Balance between convective and inertial motions ($Ri = 1.0$)

We now show the RANS simulation results for the three heating configurations where the Richardson number is increased to $Ri = 1.0$ by increasing the temperature difference between solid walls.

4.2.1 Upwind building heated

The circulating motion arising from the heating of the upwind building is shown in Fig. 4.9(a). The resulting flow field is a primary clockwise vortex which extends throughout the canyon, eliminating the recirculating regions in the top-left and bottom-right corners arising in the neutral case. Moreover, the horizontal interface bends upward reaching its maximum slightly before the centre of the canyon. The peak of the streamwise velocity at the street level near the downwind facade (Fig. 4.10(a)) testifies the loss of the secondary vortex in the bottom-right corner of the canyon, while the opposite branch remains almost the same but slightly moved upward, except for the top-left corner where the streamwise velocity slightly increases as the recirculating vortex disappears. From the non-dimensional vertical profiles in Fig. 4.10(b) it can be noticed that the downward motion near the downwind facade is slightly intensified in the upper region of the canyon ($z/H > 0.5$), and below that it weakens, while the upward motion, at the left side of the canyon, is intensified in two points, in the upper corner at $z/H = 1.0$ because of the removal of the recirculating region present in neutral conditions, and at $z/H = 0.2$.

From the temperature perturbation distribution in Fig. 4.9(b) it can be noticed a horizontal transport of the temperature from the upwind to the downwind facade which confines the highest temperatures in the left side of the canyon. In fact, the vertical profiles of the non-dimensional temperature perturbation in Fig. 4.10(c) show a constant temperature difference inside the canyon and a peak at the roof level which weakens moving toward $x/H = 1.25$ and a downward transport near the downwind building. At the street level near the upwind building, the mixing role of the recirculating region can be seen by the raising of the peak. Hence, the highest temperatures are located at the upwind side and at the top left corner.

The transport of pollutants takes place due to the motion of the main vortex, the only element of circulation in this configuration. From the concentration distribution displayed in Fig. 4.9(c), it can be noticed that the principal vortex spreads the pollutant all over the canyon transporting it with its motion, and accumulates it in the bottom-left corner in the recirculating area. Looking at the vertical profiles in Fig. 4.10(d), the concentration within the canyon along the three vertical lines is almost constant, with the only peak, besides the one at the street level where the pollutant is emitted, near

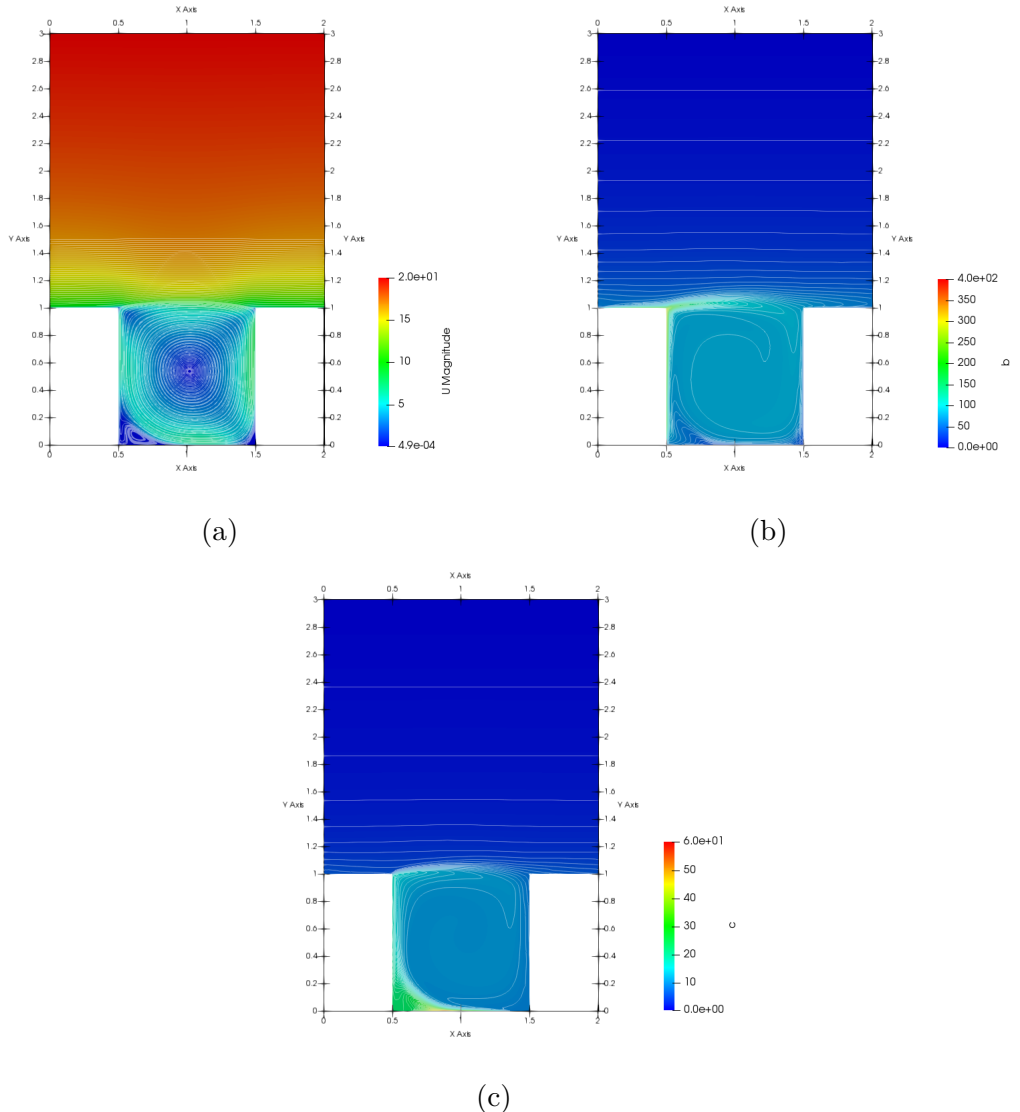


Figure 4.9: (a) Flow field streamlines, (b) contour of the buoyancy, (c) contour of the concentration for the upwind heated case when $Ri = 1.0$.

the upwind facade due to the horizontal transport. The overall concentration is higher than the one in isothermal conditions.

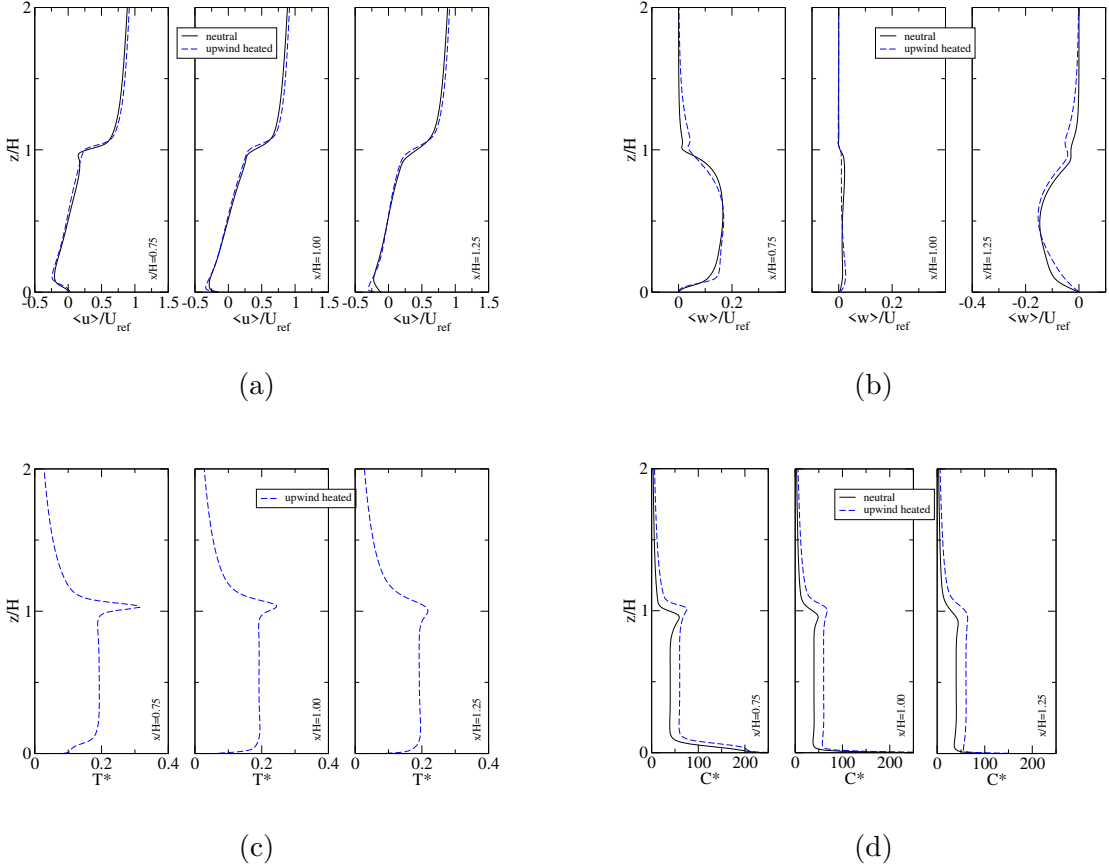


Figure 4.10: Dimensionless vertical profiles of the (a) streamwise velocity and (b) vertical velocity, (c) temperature perturbation, (d) concentration, when the upwind building is heated and $Ri = 1.0$: black solid line represents the neutral case, blue dashed line the upwind heating case.

4.2.2 Downwind building heated

As discussed in sec.4.1 for the downwind heated case, heating the downwind facade results in the shrinking of the primary vortex until it is confined in the upper region of the canyon due to the expansion of the two recirculating regions in the bottom corners. The flow field in this case is shown in Fig. 4.11. As before, the centres of the vortices are displaced toward the downwind facade and the right vortex extends almost for the whole canyon height, higher than in the case with a lower temperature difference imposed. From the vertical profiles of the non-dimensional streamwise velocity (Fig. 4.12(a)) it can be seen that the horizontal branch of the bottom vortex is very weak, given its almost zero horizontal velocity, and the previously mentioned zero-velocity region is

present. Regarding the vertical velocity in Fig. 4.12(b), it can be noticed the division of the canyon in the two counter-rotating vortices, with the bottom one being the weakest near the downwind facade.

The stratification inside the canyon resulting from this configuration is shown in Fig. 4.11(b). The highest temperature differences are localised near the downwind building because of the upward transport by the recirculating region. From there, warm air is then transported toward the upwind facade at the interface between the primary vortex and the recirculating region. Hence, the presence of warm air on the left side of the canyon can be attributed to the expansion of the recirculating region at the bottom-left corner. The vertical profiles in Fig. 4.12(c) show that near the upwind facade, at $x/H = 0.75$, the canyon is stratified into three main parts: a central part ($0.2 < z/H < 0.8$) characterised by an almost constant temperature, and two boundary regions, respectively at the roof and street levels, where the temperature decreases compared to the interior one. Moving toward the downwind building, a peak forms at $z/H = 0.7$, corresponding to the location where vertical upward transport is maximum (see Fig. 4.11(a)).

As a result of the motion of the recirculating regions, the pollutant emitted at the surface is only transported toward the downwind facade and very little toward the upwind one (Fig. 4.11(c)). Thus, the pollutant concentration is reduced, compared to the isothermal case, on the left side and at the centre of the canyon, and accumulated at the street level $z/H < 0.25$ near the downwind building, as can be seen in the vertical profile at $z/H = 1.25$ in Fig. 4.12(d), where the concentration is higher than in the neutral case, and then decreases going upward $z/H > 0.25$.

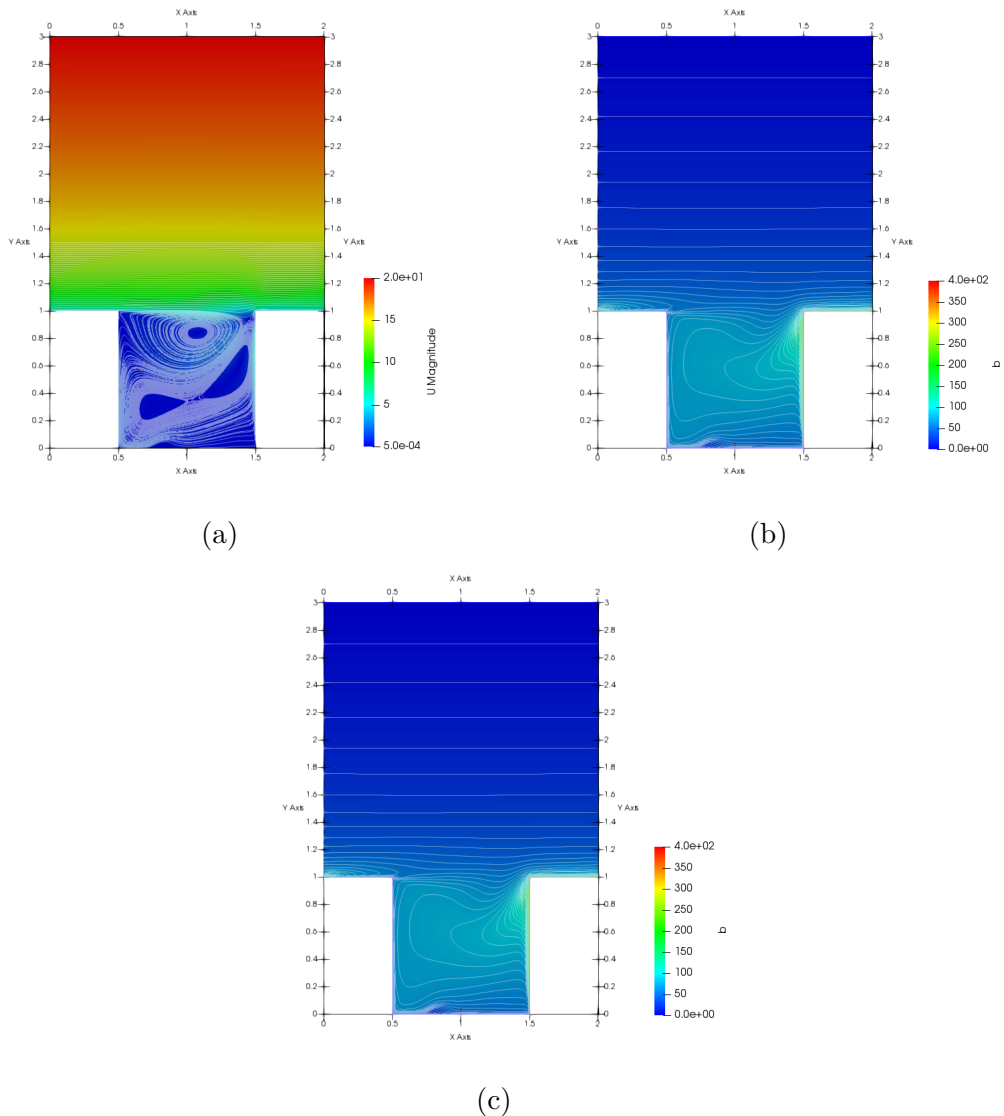


Figure 4.11: (a) Flow field streamlines, (b) contour of the buoyancy, (c) contour of the concentration for the downwind heated case when $Ri = 1.0$.

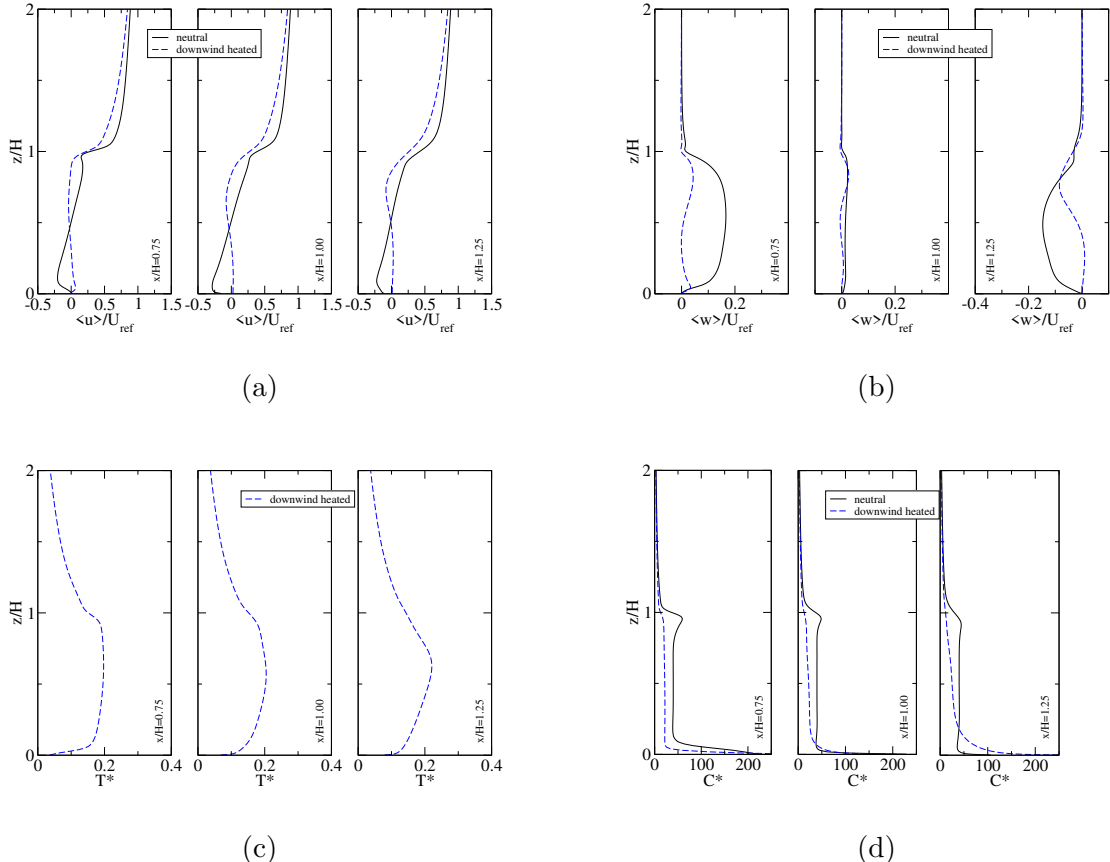


Figure 4.12: Dimensionless vertical profiles of the (a) streamwise velocity and (b) vertical velocity, (c) temperature perturbation, (d) concentration, when the downwind building is heated and $Ri = 1.0$: black solid line represents the neutral case, blue dashed line the upwind heating case.

4.2.3 Ground and both buildings heated

When all the surfaces within the canyon and the roofs of the buildings are heated, the resulting flow field is the one depicted in Fig. 4.13(a). It is immediately noticeable that a higher temperature difference between solid walls and air enhances the circulation pattern seen in the analogous case with a lower temperature difference imposed. The recirculating region at the bottom-right corner of the canyon shrinks the primary vortex dividing the canyon almost diagonally in a half. Looking at the vertical profiles of the non-dimensional velocity components in Fig. 4.14(a) and (b), it can be noticed that the lower part of the canyon is dominated by the enlarged recirculating region while the upper part by the compressed primary vortex, and their intensity is essentially comparable. Being the clockwise vortex confined in the upper region, the streamwise non-dimensional velocity in Fig. 4.14(a) shows that the upward branch at the left side of the canyon is strongly weakened, but the horizontal shear layer is almost the same to the one in neutral case, except at the top-right corner where it is pushed upward by the enlargement of the recirculating vortex. The convective motion at the downwind building is mostly given by the upward motion of the secondary vortex, hence the vertical profile Fig. 4.14(b) shows positive velocity up to $z/H = 0.5$ and then negative with a peak at $z/H = 0.75$. This negative velocity can be attributed to the downward flow of the primary vortex. The opposite happens at the upwind facade, where the upper positive velocity above $z/H > 0.5$ is due to the upward flow of the primary vortex, while the bottom negative velocity below $z/H < 0.5$ is due to the downward motion of the counter-rotating vortex. In the central region, the vertical profiles show the almost perfect splitting of the canyon in the two counter-rotating vortices, with the peak showing that the interfaces between the two is at $z/H = 0.5$.

The canyon in such configuration is practically non-stratified (Fig. 4.13(b)), and the higher temperatures can be found at the street level and near the top-left corner. The warm air at the street level is transported through the recirculating region toward the downwind building and upward by its ascending motion, resulting in the greater temperature near the downwind facade up to $z/H < 0.75$ (Fig. 4.14(c)), where it encounters colder air transported by the primary vortex. Then, the warm air is transported at the interfaces between the two vortices up to the upwind building, where it is redistributed through the canyon by the opposite vertical movements.

The transport role of the secondary vortex is responsible also for the removal of the pollutant from the street level and the consequent accumulation at the downwind facade (Fig. 4.13(c)). As a result of the circulation structure, the concentration of pollutants is higher in all of the three regions (Fig. 4.14(d)) compared to the one in isothermal conditions, with the primary vortex pushing down pollutants from the downwind facade brought by the ascending motion of recirculating region, as can be seen by the decrease of the concentration near the downwind building at $z/H > 0.75$.

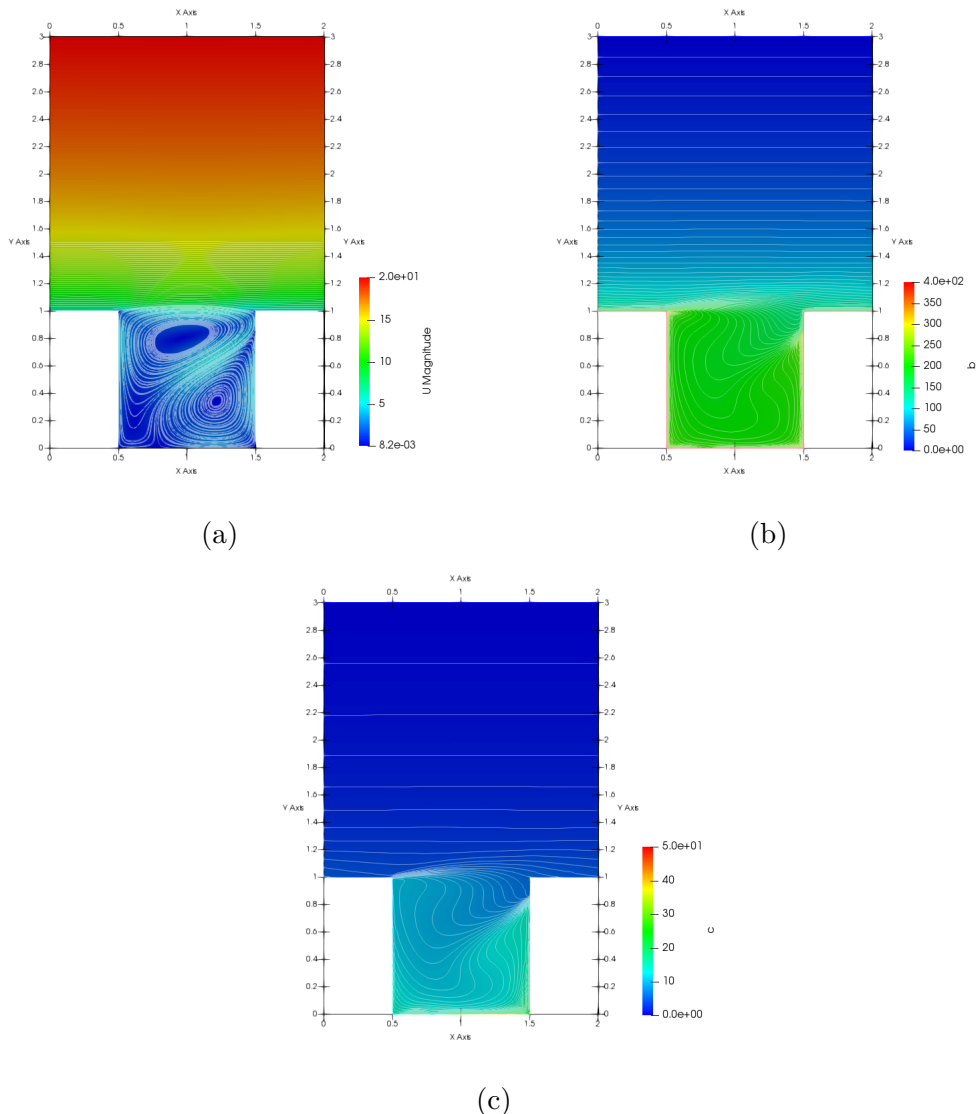


Figure 4.13: (a) Flow field streamlines, (b) contour of the buoyancy, (c) contour of the concentration for the all surfaces heated case when $Ri = 1.0$.

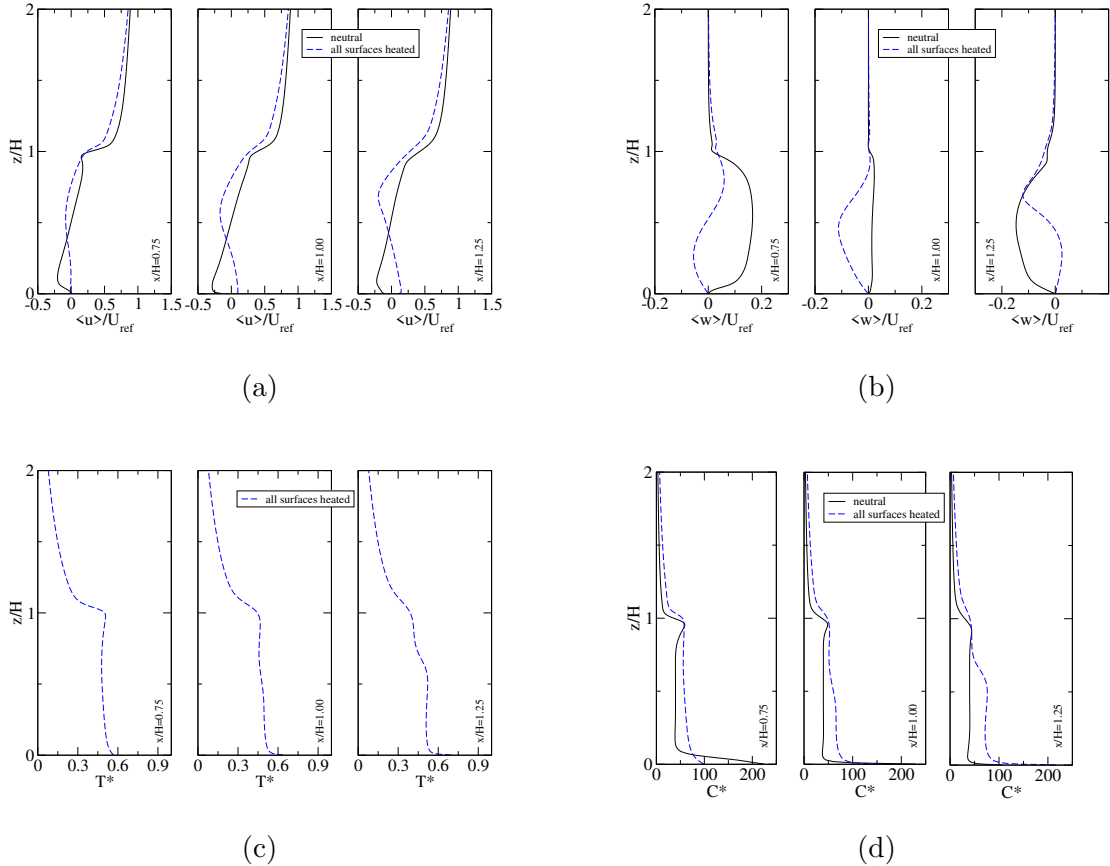


Figure 4.14: Dimensionless vertical profiles of the (a) streamwise velocity and (b) vertical velocity, (c) temperature perturbation, (d) concentration, when all surfaces are heated and $Ri = 1.0$: black solid line represents the neutral case, blue dashed line the upwind heating case.

4.3 Strong convection motions ($Ri = 1.5$)

Lastly, we show and discuss the result of the simulations when a temperature difference between solid walls such that the Richardson number is equal to $Ri = 1.5$ is imposed.

4.3.1 Upwind building heated

As previously seen, heating the upwind facade results in a convective motion composed of a primary vortex that extends throughout the whole canyon, and a minor recirculating vortex in the bottom-left corner. This configuration is shown in Fig. 4.15(a). The flow field also shows an upward displacement of the interface almost symmetrical with respect to the canyon axis. From the vertical profiles of the non-dimensional streamwise velocity in Fig. 4.16(a), the increasing intensity of the bottom peaks at $z/H = 0.2$ shows a strengthening of the horizontal branch at the street level of the main vortex. Regarding the vertical convective flows, vertical profiles of the non-dimensional perpendicular component (Fig. 4.16(b)) show that both the upward flow near the upwind building and the downward flow at the side of the downwind facade increase their strength. Overall, the resulting circulation is reinforced compared to the one resulting in isothermal conditions.

In this way, the main vortex carries warm air from the upwind building to the downwind building through the horizontal flow at the interface, which is then transported to the street by the descending motion near the downwind facade (Fig. 4.15(b)). Since the top-left minor vortex disappears, the higher temperature is found at the interface near the upwind facade. In this configuration, the branch at the interface transports warm air up to the downwind building, as shown by the peaks at $z/H = 1.0$ in all of the three plots of Fig. 4.16(c), which is then transported in the other regions of the canyon, with the exception of the bottom-right corner because of the loss of the recirculating vortex in this point. A region of low temperature difference can be detected close to the street at $z/H < 0.2$ near the upwind building where the recirculating region superimposes on the upward transport of warm air of the main vortex, decreasing the temperature.

The circular motion of the principal vortex brings pollutants from the street to the heated facade and spreads them throughout the canyon (Fig. 4.15(d)), helped by the bottom-left corner counter-clockwise vortex which accumulates pollutants at that point. Thus, the concentration is maximum at the street level and slightly above the roof level of the upwind building, where it is transported by the enhanced upward motion. Moving toward the opposite facade, i.e $x/H = 1.25$, the concentration along the height of the canyon is essentially constant. From the non-dimensional concentration vertical profiles in Fig. 4.16(d), it can be noticed that the resulting convective motion enhances the concentration of the pollutant in the whole canyon, compared to the neutral case.

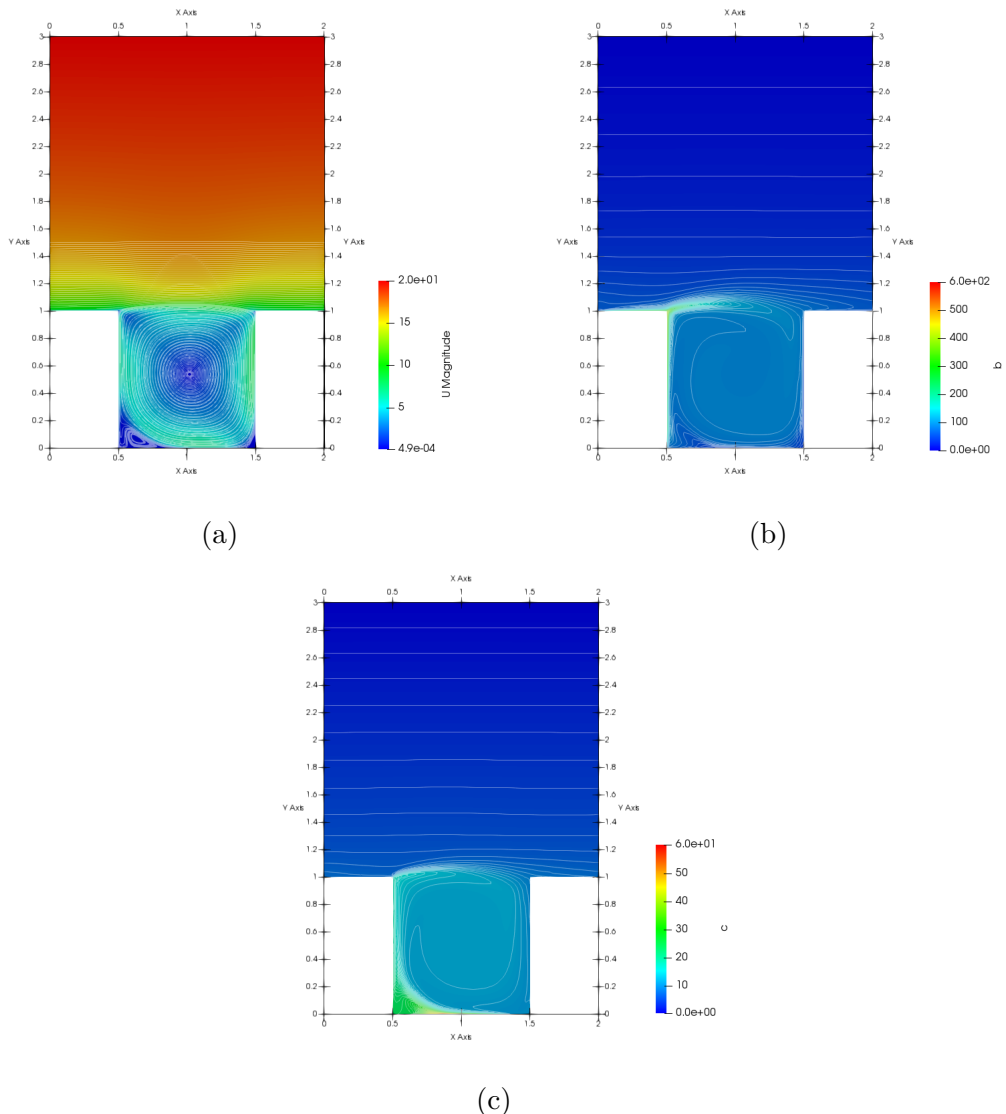


Figure 4.15: (a) Flow field streamlines, (b) contour of the buoyancy, (c) contour of the concentration for the upwind heated case when $Ri = 1.5$.

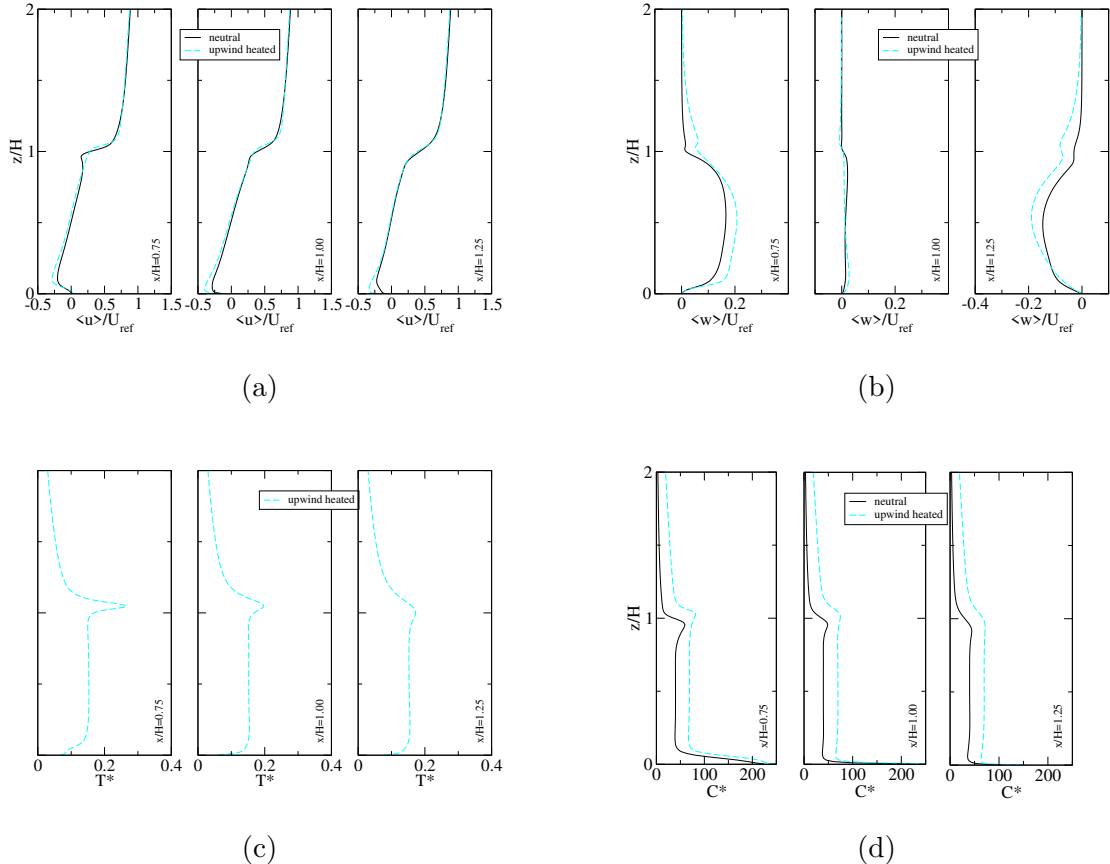


Figure 4.16: Dimensionless vertical profiles of the (a) streamwise velocity and (b) vertical velocity, (c) temperature perturbation, (d) concentration, when the upwind building is heated and $Ri = 1.5$: black solid line represents the neutral case, cyan dashed line the upwind heating case.

4.3.2 Downwind building heated

When the downwind facade is brought to a temperature higher than the ambient, the principal vortex is pushed in the upper part of the canyon and the two recirculating regions in the bottom corners expand (Fig. 4.17(a)). Due to the presence of the main vortex above the two counter-rotating vortices in the lower half of the canyon, the velocity profiles of Fig. 4.18(a) and (b) show opposite behaviour between the upper and the lower part of the canyon, following the direction of the motion of each circulating vortex. Even though the circulating regions are reinforced compared to the cases with a lower temperature difference between the walls, the previously mentioned zero-velocity region is still well visible.

The right-side recirculating vortex pushes warm air upward near the downwind building, which is in turn brought to the centre by both the main vortex and the counter-rotating one near the downwind building. Here, the left-side vortex moves the warm air toward the upwind facade and then downward. The overall motion results in a vertical stratification of the canyon, as shown by Fig. 4.17(b), with higher temperatures at the street level near the downwind building resulting from the convective motion of the vortex in this region, which transports warm air from the centre of the upwind building downward to the street level, and then again toward the downwind building. Vertical profiles of the non-dimensional temperature perturbation (Fig. 4.18(c)) show that moving toward the downwind building a peak of temperature develops at $z/H = 0.75$ due to the right recirculating region bringing warm air upward.

In this way, also the tracer is brought toward the downwind facade, resulting in the accumulation of the pollutant at the street level and in the bottom right corner (Fig. 4.17(c)). The vertical profiles of the concentration, shown in Fig. 4.18(d), are essentially constant along the vertical lines at $x/H = 0.75$ and $x/H = 1.00$, while at $x/H = 1.25$ the transport by the recirculating vortex accumulates the pollutant at the street level and moves it upward, giving an overall concentration lower than in the neutral case above $z/H > 0.1$.

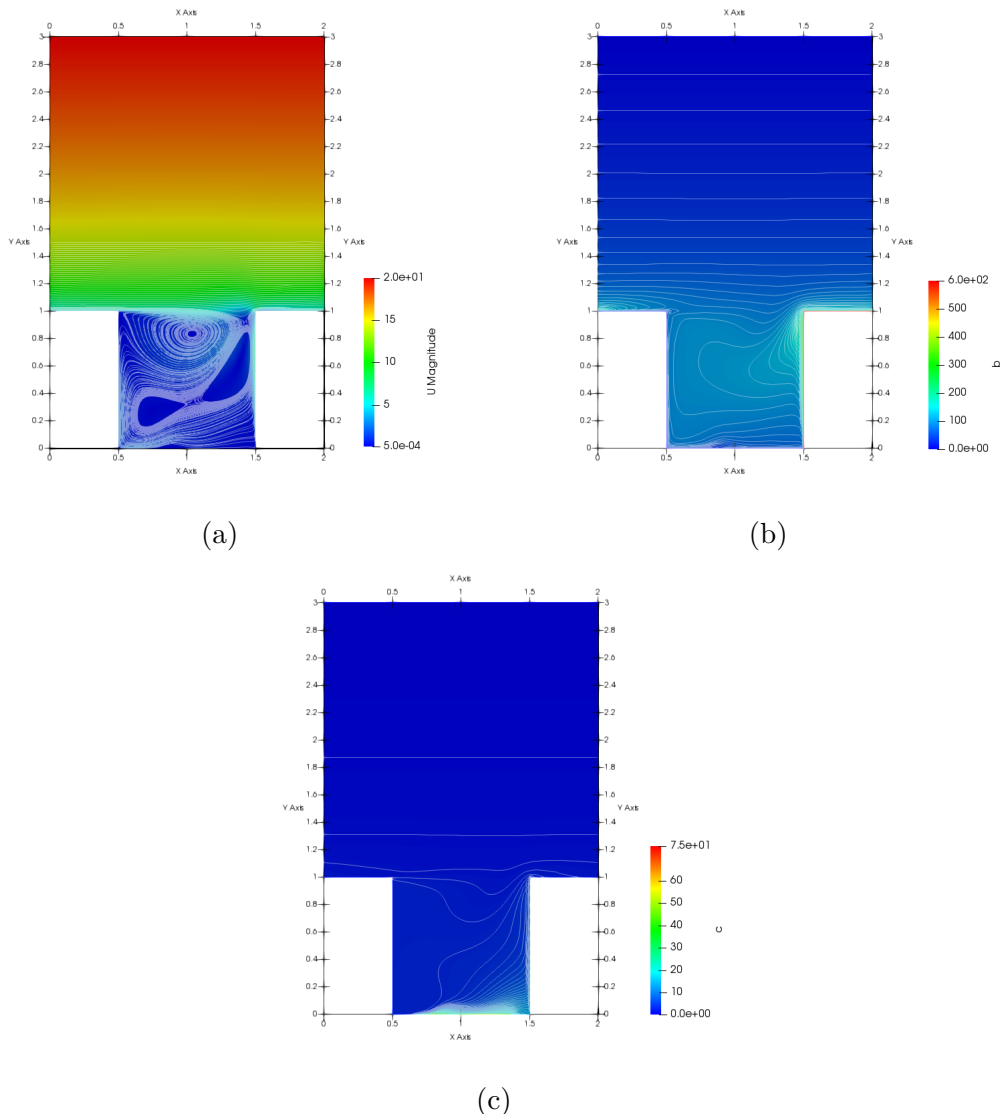


Figure 4.17: (a) Flow field streamlines, (b) contour of the buoyancy, (c) contour of the concentration for the downwind heated case when $Ri = 1.5$.

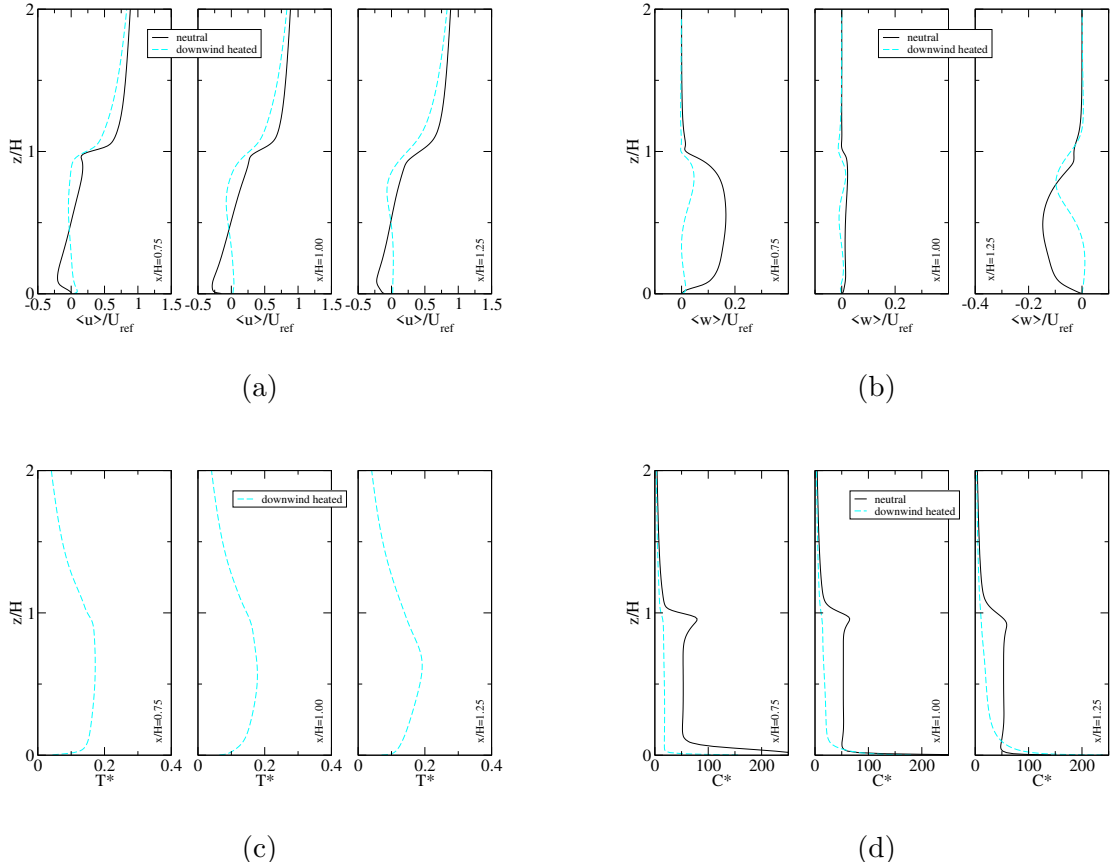


Figure 4.18: Dimensionless vertical profiles of the (a) streamwise velocity and (b) vertical velocity, (c) temperature perturbation, (d) concentration, when the downwind building is heated and $Ri = 1.5$: black solid line represents the neutral case, cyan dashed line the downwind heating case.

4.3.3 Ground and both buildings heated

The flow field generated by imposing a temperature difference between canyon boundaries and the air is shown in Fig. 4.19(a). As it was previously discussed, the main vortex is confined in the upper region of the canyon by the enlargement of the bottom-right recirculating vortex. The interface between the canyon and the outer region bends upward. The centre of the main vortex is displaced slightly toward the upwind building by the growth of the secondary vortex. The vertical profile of the non-dimensional streamwise velocity (Fig. 4.20(a)) shows the upward displacement of the upper branch of the main vortex and that the maximum horizontal (negative) velocity is reached by the secondary vortex at $z/H = 0.75$ near the downwind building. At the bottom of the canyon, such vortex shows similar strength but with a positive value. The vertical profile of the dimensionless vertical velocity (Fig. 4.20(b)) at $x/H = 1.25$ shows that the descendent flow of the main vortex is reinforced generating a peak at $z/H = 0.75$, while the upward flow of the secondary vortex is quite weak. Near the upwind facade, at $x/H = 0.75$, the two vortices show similar and opposite strength, while in the centre of the canyon the profile of the vertical velocity is almost perfectly symmetrical with respect to $z/H = 0.5$.

With the two counter-rotating vortices bringing warm air everywhere in the canyon, stratification is absent (Fig. 4.19(b)), and the vertical profiles of the dimensionless temperature perturbation (Fig. 4.20(c)) are almost constant near the upwind building and in the centre of the canyon, with the only exception near the downwind building where the two opposite branch bringing air at different temperature meets, thus resulting in a lower temperature above $z/H > 0.75$ due to the cool air brought by the descendent flow of the main vortex.

The resulting distribution of the pollutant (Fig. 4.19(c)) is similar to the analogous cases previously discussed, with the tracer being transported toward the heated facade by the reinforced recirculating vortex. Due to the heating of the rooftop which pushes streamlines upward, pollutant concentration is higher than the neutral case outside the canyon but lower near the downwind building just before the roof level because of the transport by the primary vortex (Fig. 4.20(d)). The overall concentration results higher than the one in isothermal conditions, especially at the street level, with the only exception where the main vortex brings air downward, i.e. above $z/H > 0.75$ near the downwind building, resulting in a lower concentration of pollutants in the region $0.75 < z/H < 1$.

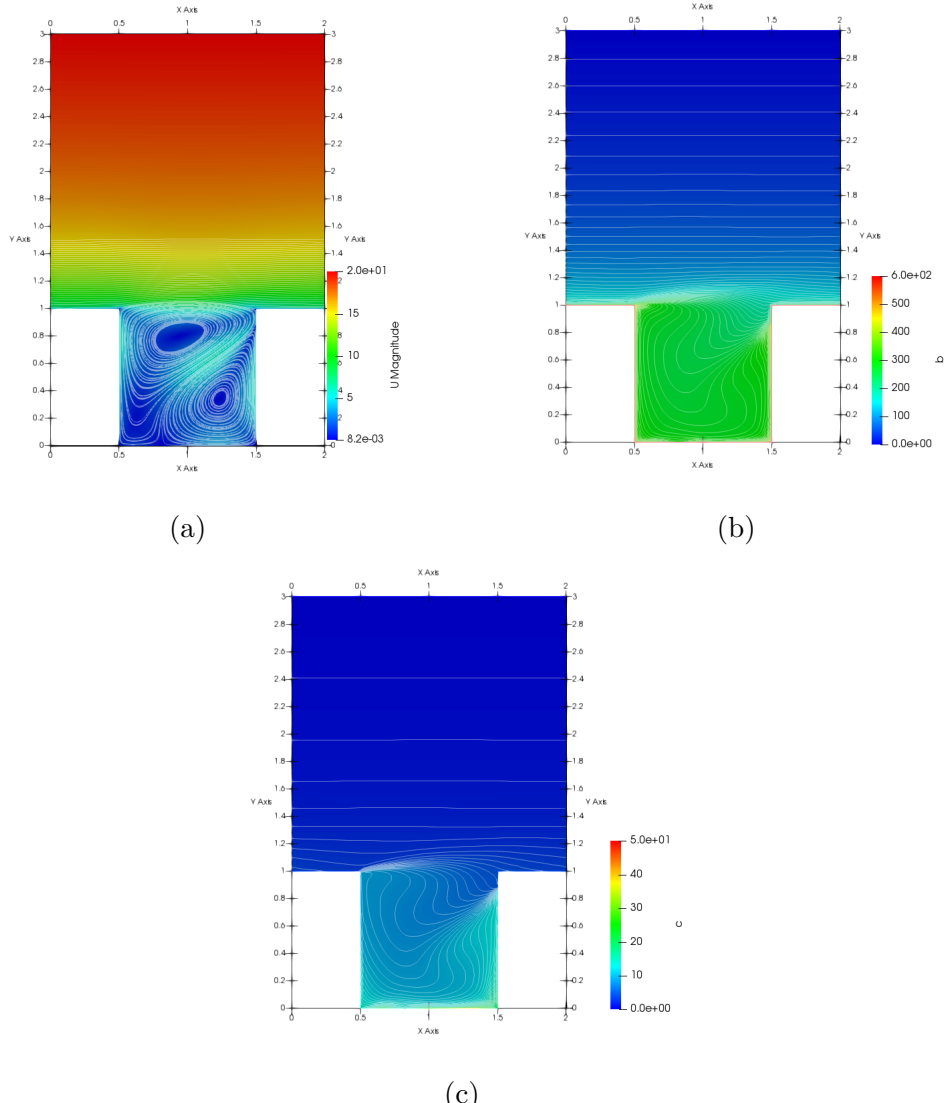


Figure 4.19: (a) Flow field streamlines, (b) contour of the buoyancy, (c) contour of the concentration when all surfaces are heated and $Ri = 1.5$.

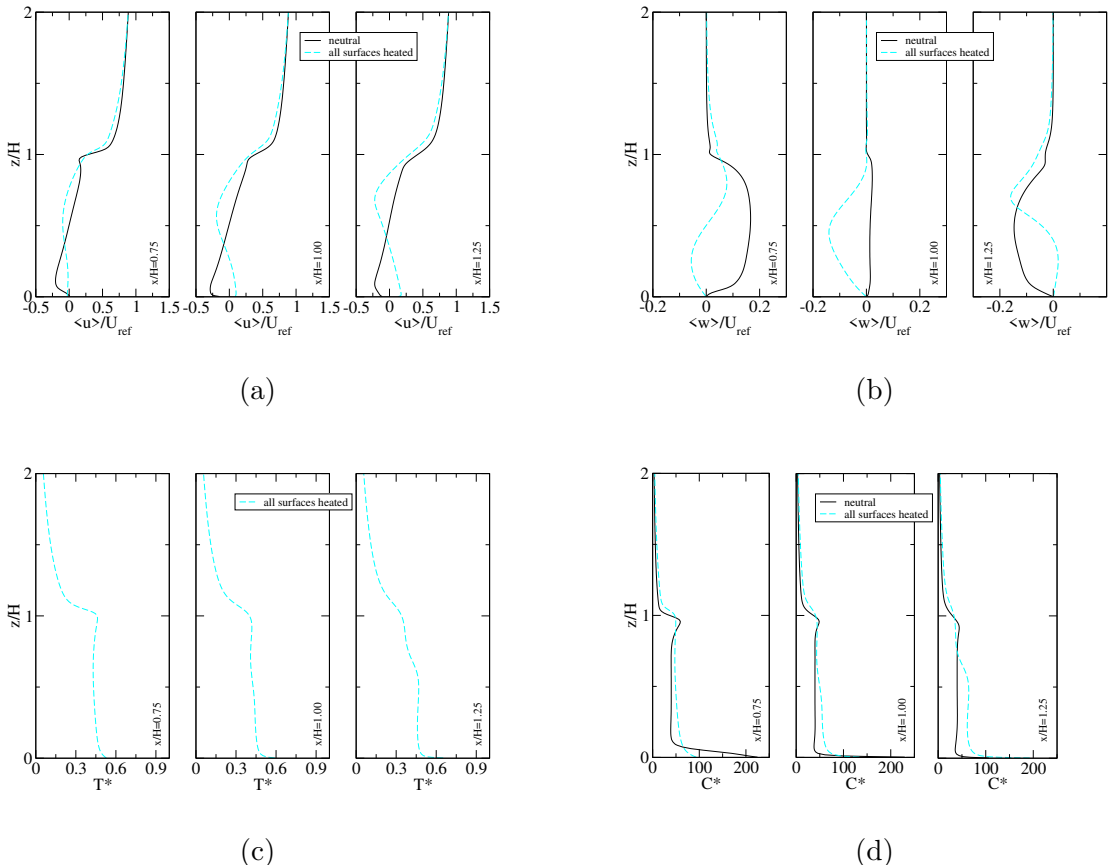


Figure 4.20: Dimensionless vertical profiles of the (a) streamwise velocity and (b) vertical velocity, (c) temperature perturbation, (d) concentration, when all surfaces are heated and $Ri = 1.5$: black solid line represents the neutral case, cyan dashed line the upwind heating case.

4.4 Discussion

In this last section, results obtained for the same configuration with increasing temperature difference imposed are compared. Since each configuration corresponds to a specific Ri , this is useful to characterise the flow and evaluate the effects of convective motions in urban canyons. To make a useful comparison between the same configuration under different temperature difference, in what follows the temperature perturbation will be analysed by means of vertical profiles of the dimensional buoyancy term b , which is directly proportional to the temperature difference being $b = g\beta T$.

4.4.1 Upwind building heated

We start by comparing results for the upwind building heated case. Fig. 4.21 shows the vertical profiles of the analysed quantities, previously made dimensionless through the usual procedure, for the three temperature differences chosen. As concerns the streamwise velocity (Fig. 4.21(a)), all of the three profiles show a decrease of the horizontal velocity at the street level and an increase at $z/H = 1$ near the upwind facade. The former represents the enhancement of the main vortex at the street level, then the shrinking of the recirculating region in the bottom-left corner, while the latter the deletion of the secondary vortex in the top-left corner. These features are more evident with increasing temperature. Moving on to the vertical velocity in Fig. 4.21(b), it can be seen that only the curve of the $Ri = 1.5$ case shows an intensification of the upward flow near the upwind facade which extends above the roof level because of the upward displacement of the horizontal interface. The same argument holds for the vertical velocity near the downwind facade, displayed in the third panel of the same figure. In the central region, at $x/H = 1.00$, the three curves almost collapse on top of each other. Hence, it can be appreciated a stronger vertical flow, both in the upwind and downwind facade, only when a higher temperature difference is imposed, i.e. for the $Ri = 1.5$ case, while the other two cases present a motion with a strength similar to the neutral case.

Regarding the vertical profiles of the buoyancy in Fig. 4.21(c) the highest temperature difference is of course given by the higher heating configuration. It can be seen how all of the three profiles show the same behaviour, i.e. a peak of temperature difference at the roof level which flattens moving toward the downwind building facade, and a decrease at the street level near the upwind building corresponding to the bottom left recirculating region. Furthermore, it can be noticed that the buoyancy profiles for the $Ri = 1.0$ and $Ri = 1.5$ cases are closer to each other than they are with the $Ri = 0.5$ case, which can be probably attributable to the fact that for $Ri > 1$ the convective regime is established.

Lastly, Fig. 4.21(d) shows the vertical profile of the non-dimensional concentration. Here it can be seen that the effect of a stronger convective motion ($Ri = 1.5$ case) is a higher concentration of pollutants along the three regions of the canyon, namely near

the upwind facade, at the centre and near the downwind facade of the canyon.

The resulting flow field described is in agreement with other similar studies, such as Cintolesi et al. [26] and Xie et al. [28] (considering that in the latter the ground is heated together with the facades), but not for the concentration profile since the RANS simulations predict an increased distribution of the pollutants within the canyon whereas those studies show the opposite.

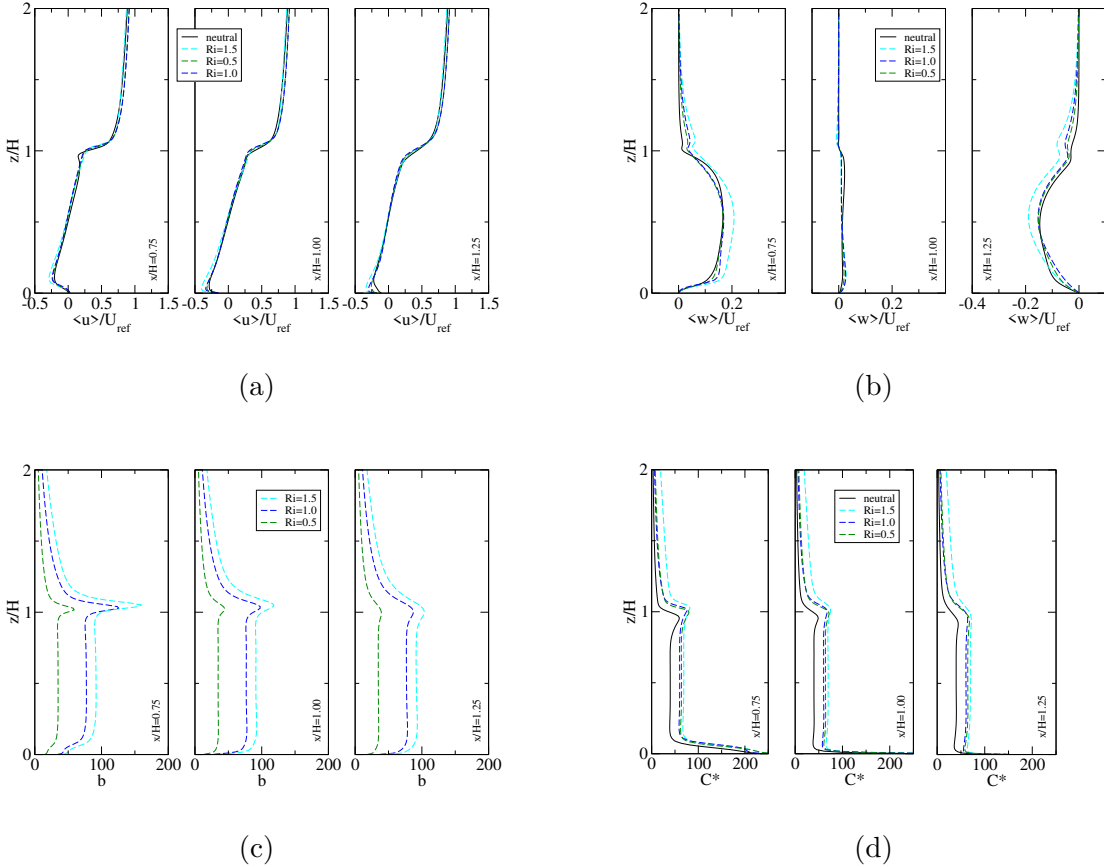


Figure 4.21: Dimensionless vertical profiles of the (a) streamwise velocity and (b) vertical velocity, (c) buoyancy (dimensional), (d) concentration, for increasing heating on the upwind building: black solid line represents the neutral case, green dashed line the $Ri = 0.5$ case, blue dashed line the $Ri = 1.0$ case, and cyan dashed line the $Ri = 1.5$ case.

4.4.2 Downwind building heated

Moving on to the downwind heated building, Fig. 4.22 displays vertical profiles of the non-dimensional velocity components, temperature perturbation and concentration. Both the streamwise and vertical velocities show that in all three cases the two-vortices structure is visible, with the three profiles overlapping, especially in the bottom region of the canyon. The greatest differences can be seen outside the canyon for the streamwise velocity (Fig. 4.22(a)), with the $Ri = 1.5$ case showing the smallest values, while producing the higher downward flow at the upper region of the downwind building (Fig. 4.22(b)). Here, the $Ri = 0.5$ curve shows lower values of the vertical velocity with a lower peak at $z/H = 0.75$, hence a weaker downward motion of the main vortex, while the $Ri = 1.0$ and $Ri = 1.5$ cases show a peak at $Z/H = 0.8$. From these arguments, we can conclude that the only difference that can be appreciated between the three cases is in the intensity of the primary vortex, confined to the upper region of the canyon, with the strongest one arising from the case with the greatest temperature difference between solid wall, i.e. the $Ri = 1.5$ case, even though all of the three configurations show overall similar strength of the vortex.

Vertical profiles of the non-dimensional temperature perturbation are shown in Fig. 4.22(c). It can be noticed that, as seen before, all of the three cases generate a stratification within the canyon, and the strongest one is found for the $Ri = 1.5$ case, with a higher peak of the buoyancy term near the downwind facade at $z/H = 0.7$ where the upward motion of the enlarged recirculating region reaches the maximum height.

Since this configuration results in convective motions with similar strength under increasing temperature differences between the walls and the air, all of the three concentration vertical profiles show very little differences between each other and an overall lower concentration compared to the isothermal case, as shown by Fig. 4.22(d). Nevertheless, the lower concentration of tracers can be found in the $Ri = 1.5$ case.

In this case, the RANS simulation obtained similar results of the flow circulation and the consequent pollutant distribution inside the canyon Xie et al. [28], while the flow field generated by the LES of Cintolesi et al. [26] slightly differs in the distribution of the vortices generated.

4.4.3 Ground and both buildings heated

The comparison between the vertical profiles of the non-dimensional quantities when all the canyon surfaces and the roofs are heated is shown in Fig. 4.23. As was previously discussed, the $Ri = 0.5$ case shows that the temperature difference imposed is too low to appreciate a significant change in the flow field within the canyon, and still reproduces, with some exceptions, especially near the downwind building, the structure that can be found in the isothermal case. With increasing temperature the two-vortices motion is appreciable. In such cases, the major differences between the $Ri = 1.0$ and $Ri = 1.5$

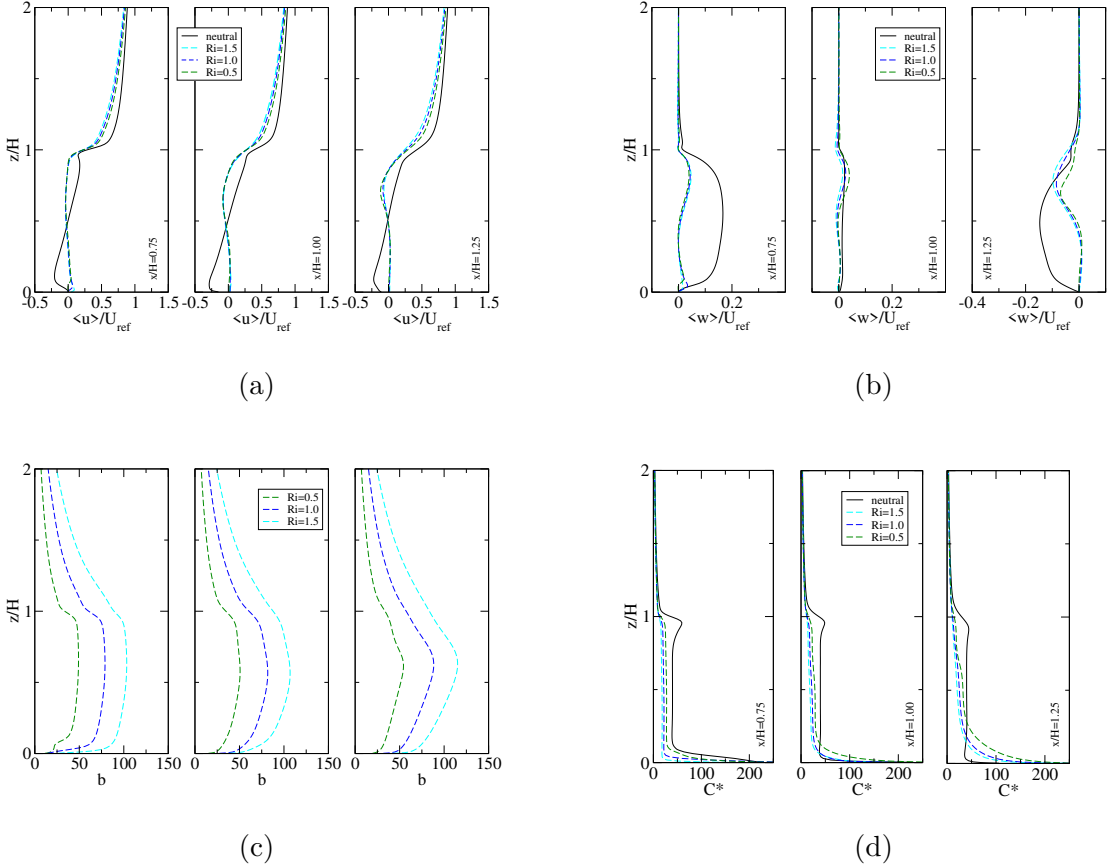


Figure 4.22: Dimensionless vertical profiles of the (a) streamwise velocity and (b) vertical velocity, (c) buoyancy (dimensional), (d) concentration, for increasing heating on the downwind building; black solid line represents the neutral case, green dashed line the $Ri = 0.5$ case, blue dashed line the $Ri = 1.0$ case, and cyan dashed line the $Ri = 1.5$ case.

cases can be seen in the vertical velocity (Fig. 4.23(b)), where the $Ri = 1.5$ case shows a more intense vertical flow, especially in the upper canyon above $z/H > 0.5$ where the main vortex is confined.

Vertical profiles of the buoyancy term are shown in Fig. 4.23(c). Given the different flow fields generated, some discrepancies can be seen between the $Ri = 0.5$ and the other two cases, especially near the downwind building. If near the upwind building the ascendant motion is given in all three cases by the vertical branch of the primary vortex, near the downwind building the buoyancy profile for the $Ri = 0.5$ case shows a constant buoyancy, hence temperature difference, in $0.25 < z < 1.00$, while the other two cases show a constant temperature difference in the lower half of the region which

decreases moving upward and it is again constant in $0.75 < z < 1.00$, as a consequence of two-vortices structure.

Finally, the concentration profiles in Fig. 4.23(d) show, as expected, lower concentration distribution between the three cases for the $Ri = 1.5$ one, and an essentially constant value for the $Ri = 0.5$ case, where the circulating motion is weakened hence the pollutant is emitted from the street and poorly spread around the canyon, bringing to a higher concentration compared to the neutral case.

Comparing the flow field generated in this configuration with the one obtained by Xie et al. [27], the same two-vortices configuration and pollutant distribution can be found.

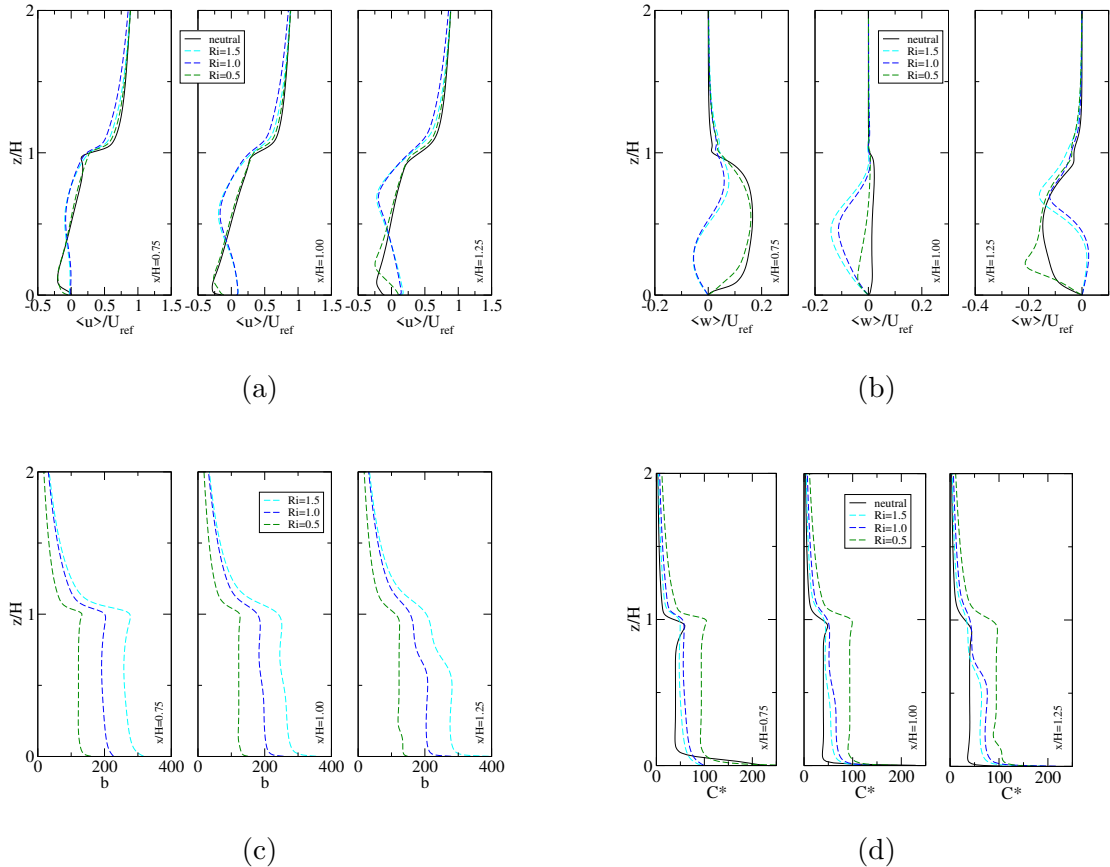


Figure 4.23: Dimensionless vertical profiles of the (a) streamwise velocity and (b) vertical velocity, (c) buoyancy (dimensional), (d) concentration, for increasing heating on all the solid surfaces: black solid line represents the neutral case, green dashed line the $Ri = 0.5$ case, blue dashed line the $Ri = 1.0$ case, and cyan dashed line the $Ri = 1.5$ case.

Conclusions

The present work aimed to investigate the effects of different thermal heating configurations on the dispersion of a pollutant within an urban street canyon with unity aspect ratio. With increasing urbanisation and warmer temperatures due to climate changes, this constitutes a highly fundamental topic for assessing and monitoring air quality in urban areas and the exposure of citizens to pollutants. To do so, several RANS simulations of a square urban canyon are carried out by using the open-source software OpenFOAM v6 adopting the Reynolds-Averaged Navier-Stokes (RANS) approach with the use of the $k - \varepsilon$ closure model and a properly modified SIMPLE algorithm. The case study reproduces a two-dimensional square urban canyon ($H/W = 1$) where an ambient wind flows from the left side to the right side perpendicular to the canyon axis, and a pollutant is emitted at the street level in a region of width $0.7 H$ centred in the street.

Before introducing the thermal effects, the isothermal case has been illustrated to give a better understanding of the case study under neutral conditions. In such a configuration, a main clockwise vortex extending throughout the canyon is generated, together with three recirculating regions at the top-left, bottom-left and bottom-right corners. The main rotating structure carries the pollutant emitted at the street level to the other regions of the canyon. The model implemented has been validated, for the isothermal condition, against several experimental data and two LES simulations, while the one with the introduction of thermal effects against a LES simulation. In the first case the model shows a good agreement between the CFD results and the reference data for all the quantities examined, i.e. the velocity components, the concentration of pollutants, and the turbulent kinetic energy, all of them previously made non-dimensional. On the other hand, the validation made with the addition of the thermal effects, despite being in sufficient agreement with the reference data to carry on with the work, also shows the limitations of the approach in representing convective effects, probably attributable to the model chosen to implement. Then, the introduction of the convective motion has been done by heating the borders of the canyon and the building roofs, thus bringing them to a higher temperature compared to the ambient one. In particular, three configurations mimicking the different positions the sun assumes with respect to the canyon during the day have been explored:

- in the first one, when the sun heats on the right side of the canyon, the upwind building (both roof and facade) has been brought to a temperature higher than the other canyon walls and the air;
- in the second one, when the sun heats on the left side of the canyon, a higher temperature has been imposed on the opposite building;
- lastly, heating all the surfaces, both horizontal and vertical, reproduces the case in which the sun heats directly on the urban canyon.

Three distinctive temperature differences have been imposed, depending on which values of the Richardson number characterising the flow within the canyon are intended to be studied. Such values are $Ri = 0.5, 1.0, 1.5$. The Richardson number can be used to assess the relative importance of the buoyancy on the inertial forces. In this way, a $Ri = 0.5$ represents a case where the convective motion is suppressed and the flow can be described as inertially-driven; on the opposite if $Ri = 1.5$ the canopy is characterised by natural convection since the buoyancy forcing dominates. The results of those simulations can be summarised as follows:

- Heating the upwind building results in the enlargement of the primary vortex as a consequence of the size reduction of the two recirculating zones at the top-left and bottom-right corners of the canyon. As a result, the strongest convective motion is found for the $Ri = 1.5$ case with an overall enhanced primary vortex compared to the one resulting from isothermal conditions, which leads to a higher concentration of pollutants throughout the canyon.
- In the case where the downwind building has been heated, a motion consisting of two counter-rotating vortices arises from the enlarging of the bottom recirculating region, which pushes the main vortex up and weakens it. The result is a stratified canyon in which the convective motion is not sufficient to distribute pollutants all over the canyon, hence they are accumulated in the bottom-right corner producing a region where the pollutant concentration is up to double the one in the isothermal case, while in the other parts of the canyon, it lowers becoming almost half of how it was in neutral conditions. This is a key aspect since such region corresponds to the pedestrian level.
- Lastly, when all surfaces are heated, a two-vortices structure arranged diagonally within the canyon arises from the growth of the bottom-right recirculating region. Such structure is visible only for the $Ri = 1.0$ and $Ri = 1.5$ cases, with the $Ri = 0.5$ one still showing the primary vortex and an enlarged recirculating region at the bottom-right corner. The configuration with $Ri = 0.5$ shows a concentration distribution which is doubled compared to the neutral case, while the other two,

i.e. the ones with $Ri = 1.0$ and $Ri = 1.5$, show a higher accumulation of the pollutant which increases moving toward the downwind building up to 50%.

To conclude, this work showed that the only configuration that foresees a decrease in the concentration of pollutants within the canyon is the one where the downwind building is heated. This is in good agreements with studies of the same topic, such as the one conducted by Xie et al. [28] and Cintolesi et al. [26].

This project can be improved in many different ways. First of all, a three-dimensional geometry, instead of a two-dimensional one, could be generated in order to better represent the flow characteristics and the phenomena appearing in the street canyon, with overall a better representation of the real case. This is especially useful for optimising the street urban design, as pointed out by Mei et al. [34] which investigated the correlation between the street length and the ventilation capacity within street canyons and found that the principal vortex structure arising in isothermal conditions changes with the street length/street width ratio.

Another great improvement of the present work would consist in considering also the stratification of the urban atmosphere, by conducting different simulations under different stratification conditions, i.e. stable, unstable, other than neutral, and studying how those conditions affect the pollutant dispersion mechanism. A study in this direction has been carried out by Li et al. [35], where by means of a LES simulation they found that under stable stratification conditions, the flow and the vertical transport of momentum and heat are reduced, resulting in a higher concentration of pollutant near the ground, increasing the exposure of pedestrian to pollution.

Furthermore, an interesting discussion could arise by studying urban canyons with different aspect ratios. In fact, this would mean investigate not only the skimming flow regime but also the wake interface flow and the isolated roughness flow, leading to different flow fields and pollutant accumulation.

Finally, a last step could be including additional objects within the street canyon which could alter the wind flow field, such as trees and built-up elements, to study how these affect mean profiles.

Bibliography

- [1] Van Thinh Nguyen, Thanh Chuyen Nguyen, and John Nguyen. “Numerical Simulation of Turbulent Flow and Pollutant Dispersion in Urban Street Canyons”. In: *Atmosphere* 10.11 (2019). ISSN: 2073-4433. DOI: 10.3390/atmos10110683. URL: <https://www.mdpi.com/2073-4433/10/11/683>.
- [2] Salim Mohamed Salim, Siew Cheong Cheah, and Andrew Chan. “Numerical simulation of dispersion in urban street canyons with avenue-like tree plantings: Comparison between RANS and LES”. In: *Building and Environment* 46.9 (2011), pp. 1735–1746. ISSN: 0360-1323. DOI: <https://doi.org/10.1016/j.buildenv.2011.01.032>. URL: <https://www.sciencedirect.com/science/article/pii/S0360132311000710>.
- [3] R.B. Stull. *An Introduction to Boundary Layer Meteorology*. Atmospheric and Oceanographic Sciences Library. Springer Netherlands, 1988. ISBN: 9789027727695. URL: <https://books.google.it/books?id=eRRz9RNvN0kC>.
- [4] Wonsik Choi et al. “Estimating the atmospheric boundary layer height over sloped, forested terrain from surface spectral analysis during BEARPEX”. In: *Atmospheric Chemistry and Physics* 11 (July 2011). DOI: 10.5194/acp-11-6837-2011.
- [5] Rex Britter and Steven Hanna. “Flow and Dispersion in Urban Canopies”. In: (Nov. 2001).
- [6] T.R. Oke. “The distinction between canopy and boundary-layer urban heat islands”. In: *Atmosphere* 14.4 (Dec. 1976), pp. 268–277. DOI: 10.1080/00046973.1976.9648422.
- [7] T.R. Oke. “The urban energy balance”. In: *Progress in Physical Geography: Earth and Environment* 12.4 (1988), pp. 471–508. DOI: 10.1177/030913338801200401. eprint: <https://doi.org/10.1177/030913338801200401>. URL: <https://doi.org/10.1177/030913338801200401>.
- [8] L.J. Hunter, I.D. Watson, and G.T. Johnson. “Modelling air flow regimes in urban canyons”. In: *Energy and Buildings* 15.3 (1990), pp. 315–324. ISSN: 0378-7788. DOI: [https://doi.org/10.1016/0378-7788\(90\)90004-3](https://doi.org/10.1016/0378-7788(90)90004-3). URL: <https://www.sciencedirect.com/science/article/pii/0378778890900043>.

- [9] A. John Arnfield. "Two decades of urban climate research: a review of turbulence, exchanges of energy and water, and the urban heat island". In: *International Journal of Climatology* 23.1 (Jan. 2003), pp. 1–26. DOI: 10.1002/joc.859.
- [10] Patrick E. Phelan et al. "Urban Heat Island: Mechanisms, Implications, and Possible Remedies". In: *Annual Review of Environment and Resources* 40.1 (Nov. 2015), pp. 285–307. DOI: 10.1146/annurev-environ-102014-021155.
- [11] Gerald Mills. "Luke Howard and The Climate of London". In: *Weather* 63.6 (2008), pp. 153–157. DOI: 10.1002/wea.195.
- [12] T.R. Oke. "City size and the urban heat island". In: *Atmospheric Environment* (1967) 7.8 (Aug. 1973), pp. 769–779. DOI: 10.1016/0004-6981(73)90140-6.
- [13] Werner Marx, Robin Haunschild, and Lutz Bornmann. "Heat waves: a hot topic in climate change research". In: *Theoretical and Applied Climatology* 146.1-2 (Sept. 2021), pp. 781–800. DOI: 10.1007/s00704-021-03758-y.
- [14] Selma B Guerreiro et al. "Future heat-waves, droughts and floods in 571 European cities". In: *Environmental Research Letters* 13.3 (Feb. 2018), p. 034009. DOI: 10.1088/1748-9326/aaaad3.
- [15] IPCC. *Climate Change 2021: The Physical Science Basis. Contribution of Working Group I to the Sixth Assessment Report of the Intergovernmental Panel on Climate Change*. Vol. In Press. Cambridge, United Kingdom and New York, NY, USA: Cambridge University Press, 2021. DOI: 10.1017/9781009157896.
- [16] Olga V. Taseiko et al. "Air pollution dispersion within urban street canyons". In: *Atmospheric Environment* 43.2 (Jan. 2009), pp. 245–252. DOI: 10.1016/j.atmosenv.2008.09.076.
- [17] Laura Ehrnsperger and Otto Klemm. "Air pollution in an urban street canyon: Novel insights from highly resolved traffic information and meteorology". In: *Atmospheric Environment: X* 13 (Jan. 2022), p. 100151. DOI: 10.1016/j.aeaoa.2022.100151.
- [18] Xian-Xiang Li et al. "Physical Modeling of Flow Field inside Urban Street Canyons". In: *Journal of Applied Meteorology and Climatology* 47.7 (2008), pp. 2058–2067. DOI: 10.1175/2007JAMC1815.1. URL: <https://journals.ametsoc.org/view/journals/apmc/47/7/2007jamc1815.1.xml>.
- [19] Lup Wai Chew, Amir A. Aliabadi, and Leslie K. Norford. "Flows across high aspect ratio street canyons: Reynolds number independence revisited". In: *Environmental Fluid Mechanics* 18.5 (May 2018), pp. 1275–1291. DOI: 10.1007/s10652-018-9601-0.
- [20] Michael Brown et al. "Mean Flow and Turbulence Measurement around a 2-D Array of Buildings in a Wind Tunnel". In: Jan. 2000.

- [21] Takenobu Michioka et al. “Large-Eddy Simulation for the Mechanism of Pollutant Removal from a Two-Dimensional Street Canyon”. In: *Boundary-Layer Meteorology* 138.2 (Nov. 2010), pp. 195–213. DOI: 10.1007/s10546-010-9556-2.
- [22] Michel Pavageau and Michael Schatzmann. “Wind tunnel measurements of concentration fluctuations in an urban street canyon”. In: *Atmospheric Environment* 33.24 (1999), pp. 3961–3971. ISSN: 1352-2310. DOI: [https://doi.org/10.1016/S1352-2310\(99\)00138-7](https://doi.org/10.1016/S1352-2310(99)00138-7). URL: <https://www.sciencedirect.com/science/article/pii/S1352231099001387>.
- [23] Robert N. Meroney et al. “Study of line source characteristics for 2-D physical modelling of pollutant dispersion in street canyons”. In: *Journal of Wind Engineering and Industrial Aerodynamics* 62.1 (1996), pp. 37–56. ISSN: 0167-6105. DOI: [https://doi.org/10.1016/S0167-6105\(96\)00057-8](https://doi.org/10.1016/S0167-6105(96)00057-8). URL: <https://www.sciencedirect.com/science/article/pii/S0167610596000578>.
- [24] Carlo Cintolesi, Beatrice Pulvirenti, and Silvana Di Sabatino. “Large-Eddy Simulations of Pollutant Removal Enhancement from Urban Canyons”. In: *Boundary-Layer Meteorology* 180.1 (Mar. 2021), pp. 79–104. DOI: 10.1007/s10546-021-00610-8.
- [25] Rizwan Ahmed Memon and D. Y. C. Leung. “On the heating environment in street canyon”. In: *Environmental Fluid Mechanics* 11.5 (Dec. 2010), pp. 465–480. DOI: 10.1007/s10652-010-9202-z.
- [26] Carlo Cintolesi, Francesco Barbano, and Silvana Di Sabatino. “Large-Eddy Simulation Analyses of Heated Urban Canyon Facades”. In: *Energies* 14.11 (2021). ISSN: 1996-1073. DOI: 10.3390/en14113078. URL: <https://www.mdpi.com/1996-1073/14/11/3078>.
- [27] Xiaomin Xie, Chun-Ho Liu, and Dennis Y.C. Leung. “Impact of building facades and ground heating on wind flow and pollutant transport in street canyons”. In: *Atmospheric Environment* 41.39 (Dec. 2007), pp. 9030–9049. DOI: 10.1016/j.atmosenv.2007.08.027.
- [28] Xiaomin Xie et al. “Thermal effects on vehicle emission dispersion in an urban street canyon”. In: *Transportation Research Part D: Transport and Environment* 10.3 (May 2005), pp. 197–212. DOI: 10.1016/j.trd.2005.01.002.
- [29] John D. Anderson. *Computational fluid dynamics the basic with applications. the basic with applications*. McGraw-Hill, 1995, p. 547. ISBN: 9780071132107.
- [30] Stephen B. Pope. *Turbulent Flows*. Cambridge University Press, Aug. 2000. DOI: 10.1017/CBO9780511840531.
- [31] Christopher Greenshields. *OpenFOAM v6 User Guide*. London, UK: The OpenFOAM Foundation, 2018. URL: <https://doc.cfd.direct/openfoam/user-guide-v6>.

- [32] Xian-Xiang Li, Rex E. Britter, and Leslie K. Norford. “Transport processes in and above two-dimensional urban street canyons under different stratification conditions: results from numerical simulation”. In: *Environmental Fluid Mechanics* 15.2 (Feb. 2014), pp. 399–417. DOI: [10.1007/s10652-014-9347-2](https://doi.org/10.1007/s10652-014-9347-2).
- [33] Yucong Miao et al. “Numerical study of the effects of Planetary Boundary Layer structure on the pollutant dispersion within built-up areas”. In: *Journal of Environmental Sciences* 32 (2015), pp. 168–179. ISSN: 1001-0742. DOI: <https://doi.org/10.1016/j.jes.2014.10.025>. URL: <https://www.sciencedirect.com/science/article/pii/S1001074215001382>.
- [34] Shuo-Jun Mei et al. “Street canyon ventilation and airborne pollutant dispersion: 2-D versus 3-D CFD simulations”. In: *Sustainable Cities and Society* 50 (2019), p. 101700. ISSN: 2210-6707. DOI: <https://doi.org/10.1016/j.scs.2019.101700>. URL: <https://www.sciencedirect.com/science/article/pii/S2210670719305438>.
- [35] Xian-Xiang Li, Rex Britter, and Leslie K. Norford. “Effect of stable stratification on dispersion within urban street canyons: A large-eddy simulation”. In: *Atmospheric Environment* 144 (2016), pp. 47–59. ISSN: 1352-2310. DOI: <https://doi.org/10.1016/j.atmosenv.2016.08.069>. URL: <https://www.sciencedirect.com/science/article/pii/S1352231016306689>.